Photo-Excitation of Nucleon Resonances from complex nuclei

Inauguraldissertation

zur

Erlangung der Würde eines Doktors der Philosophie
vorgelegt der
Philosophisch-Naturwissenschaftlichen Fakultät
der Universität Basel

von
Thierry Mertens
aus Nice (France)

Basel 2006

Genehmigt von der Philosophisch-Naturwissenschaftlichen Fakultät auf Antrag von Prof. Dr B. Krusche und Dr. Susan Schadmand

Basel, den 13. Juli 2006

<div style="text-align: right">

Prof. Dr. Hans-Jacob Wirz Dekan

</div>

ii

Contents

Chapter 1

Introduction

1.1 General considerations

Quantum chromodynamics (QCD) is accepted as the theory of the strong interaction, a fundamental force which describes the interactions between particles with color charge via the exchange of bosons (namely eight gluons). QCD is a non abelian gauge field theory. As a consequence the gluons themselves carry color charges and interact between each other. Thus, at very short distance or large momentum transfer, the quarks inside the hadrons behave like free particles. This feature is known as the asymptotic freedom. In this kinematic region, perturbative methods as in QED are usable and allow to calculate the interaction between quarks and gluons. This aspect was successfully used to test QCD properties at very high energy. This behavior was first discovered in 1973 by David Politzer, Franck Wilczek and David Gross ([1]). They were awarded the nobel prize in 2004 for this discovery.
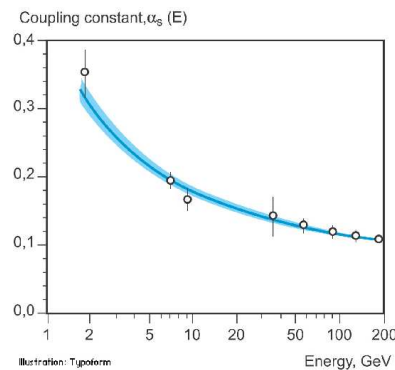
Figure 1.1: *Evolution of the coupling constant as function of the energy scale E. The decrease of the coupling constant at high energies is a prediction of the asymptotic freedom in QCD and is in quite good agreement with measurements. Picture from ([1])*

This thesis work deals with phenomena occuring at the typical energy scale of the

mass of nucleon resonances (a few GeV) and focuses on possible in-medium modifica-
tion of hadrons properties. At this energy scale, perturbative methods are no longer
valid anymore. Quarks and gluons interact strongly with each other, this feature is
called confinement. Up to now only phenomenological models were able to describe
the confinement, therefore measured observables are required in models for further in-
terpretation. The aim of this thesis is to search for possible in-medium modifications
of hadron properties in a dense environment. One very debated topic in modern physic
is to study whether and how the properties of particles in-vacuum are modified when
those particles are embedded under other conditions, for example in a dense and/or
hot environment. Experimentally observable quantities discussed in this context are in
particular masses and widths of hadronic particles.

1.2 QCD and chiral symmetry

The most general form of the QCD Lagrangian can be written as follows :

$$\mathcal{L}_{QCD} = \bar{\psi}_q(i\gamma^\mu D_\mu - M)\psi_q - \frac{1}{4}G^{\mu\nu}G_{\mu\nu} \tag{1.1}$$

where ψ_q is the quark field, M the quark mass matrix, γ_μ ($\mu = 0,1,2,3$) are the Dirac matrices, $G_{\mu\nu}$ the gluon tensor and D_μ the covariant derivative dealing with the coupling between the quarks and the gauge potentials. The chiral symmetry is a fundamental symmetry of QCD, valid in the limit of vanishing quark masses. Chirality is related to the spin orientation relative to the direction of the momentum which may be either positive (right handed) or negative (left handed). Nevertheless, due to the few MeV masses of the up and down quarks (5 to 10 MeV) this symmetry is explicitly broken. Furthermore, at high energy (or high temperature) the system is invariant under any transformation given by the equations governing the system. Considering low energy, due to the fact that the QCD ground state is not symmetric a spontaneous breaking of the symmetry is expected. In these conditions, the system is no longer invariant under any transformations. This feature is illustrated in the next two plots which show two differents rotational invariant potentials (fig 1.2). In fig (a) the minimum of the potential is in the center while in fig (b) the ground state is located far from the center which shows a local maximum. Any arbitrary choice of the ground state is breaking the rotational symmetry spontaneously, i.e any deviation from the ground state would lead to excitations.
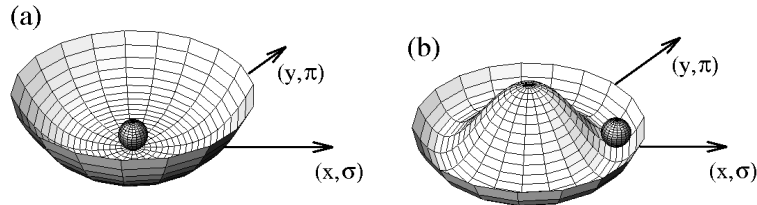
Figure 1.2: *Potentials illustrating the spontaneous breaking of the chiral symmetry plot (a) this kind of potential is not breaking the symmetry, plot(b) does spontaneously break the symmetry. More details are found in text, the plot is from [3].*

According to the Goldstone theorem any spontaneous breaking of a symmetry induces the existence of a Goldstone boson that may be interpreted as new excitation at low energy. This kind of phenomenum is visible for example in solid state physics as "phonons".

In the case of QCD, the number of Goldstone bosons is related to the number of quark flavors according to the relation $n_f^2 - 1$, where n_f is the flavor number. Considering the up and down quarks three Goldstone bosons are identified with the three pions $(\pi^\pm, \pi^0)$. In addition, the "strange" quark will lead to eight bosons that are identified with the three pions, four kaons, and the η.

Chiral symmetry implies existence of parity doublets. That means that for each baryon with a certain mass, a given quantum number, and parity, another baryon should exists with the same properties but an opposite parity. This feature is not observed in nature, as shown with the next examples :

$$
\begin{aligned}
M(\rho) &= 770 MeV (J^\pi = 1^-) < M(a_1) = 1260 MeV (J^\pi = 1^+) \\
M(\pi) &= 135 MeV (J^\pi = 0^-) < M(\sigma) = 600 MeV (J^\pi = 0^+) \\
M(N) &= 939 MeV (J^\pi = 1/2^+) < M(S_{11}) = 1535 MeV (J^\pi = 1/2^-) \quad (1.2)
\end{aligned}
$$

Gell-mann, Oaks and Renner give the formula which links the mass of the pion to the quark condensate ([4])

$$
m_\pi^2 = -\frac{1}{f_\pi^2}\frac{m_u + m_d}{2} + (\langle u\bar{u}\rangle + \langle d\bar{d}\rangle) + O(m_{u,d}^2). \tag{1.3}
$$

The right part of the Gell-Mann, Oaks, Rennes (GOR) expression carries information on both explicit symmetry breaking through the quark mass and on the spontaneous breaking through the expression of the chiral condensate. This quantity is an order parameter of the spontaneously broken symmetry and shows a dependance on both temperature and density. Using the GOR expression Brockmann and Weise get the following expression of the chiral condensate $\langle \bar{q}q\rangle$

$$
\langle \bar{q}q\rangle_{med}(\rho, T) = (1 - \sum_h \frac{\sigma_h \rho_h^s(\rho, T)}{f_\pi^2 m_\pi^2})\langle \bar{q}q\rangle_{vac}. \tag{1.4}
$$

The sum runs over all the hadronic states h, f_π is the pion decay constant, σ_h is the so-called sigma commutator containing all the information about the chiral properties of h and ρ_s is the scalar density of h.
Inserting numerical values in the previous equation leads to

$$
\langle \bar{q}q\rangle_{med}(\rho, 0) = (1 - 0.35 * \frac{\rho}{\rho_0})\langle \bar{q}q\rangle_{vac}. \tag{1.5}
$$

Therefore, a drop of 35 % of the chiral condensate is already expected at normal nuclear density ρ_0. As a consequence, this modification of the chiral quark condensate might influence the in-medium hadron properties.
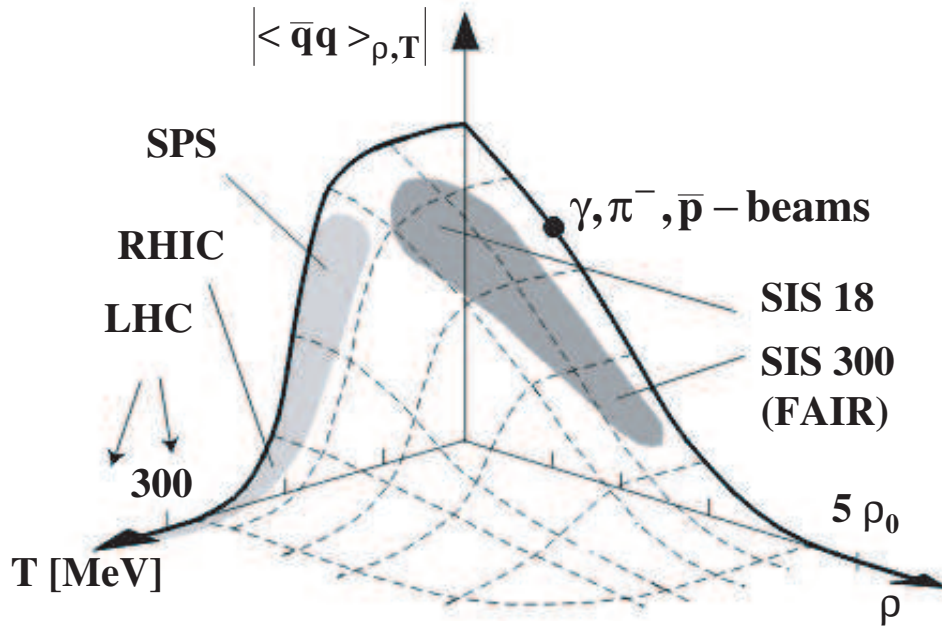
Figure 1.3: *Quark condensate taken from the Nambu, Jona, Lasinio model. The dependence of the chiral condensate on density and temperature shows that a complete restoration of the chiral symmetry is expected at high temperature or very high density. Picture from [5]*

1.3 Standard model and particle properties

The in-vacuum properties of a few hadrons, like the mass and the width are shown in this section. Most of the informations presented in this part can be found in the Particle Data Booklet [2]. The standard model of particle physic is a theory describing strong, weak and electromagnetic fundamental forces and contains both fermionic and bosonic fundamental particles. Fermions are particles with half integer spin and obey the Pauli exclusion principle while bosons are integer spin and do not follow Pauli principle. In a sense, fermions can be seen as particles of matter and bosons are particles which transmit forces. The elementary fermionic particles defined within the standard model are the 6 quarks (u,d,s,c,b,t) the corresponding antiquarks, the leptons and neutrinos. The bosonic particles are the eight gluons made from a color anticolor pair, the gauge and Higgs bosons W^+, W^-,Z^0 and the photon.

1.3.1   Properties of vector and pseudo-scalar mesons

According to the quark model the ground state nonet for both vector and pseudo-scalar mesons are described in terms of quark - antiquark pairs and can be shown in the following representation using the third component of the isospin and the strangeness. (fig1.4)

The quantum numbers needed to describe those states are the total spin and parity, J^P. In the case of pseudo-scalars J is equal to 0 while $J = 1$ for the vectors. The parity is negative in both cases, since for quark-antiquark systems $P = (-1)^{L+1}$ (L is the relative orbital angular momentum) with L = 0 for the ground state.
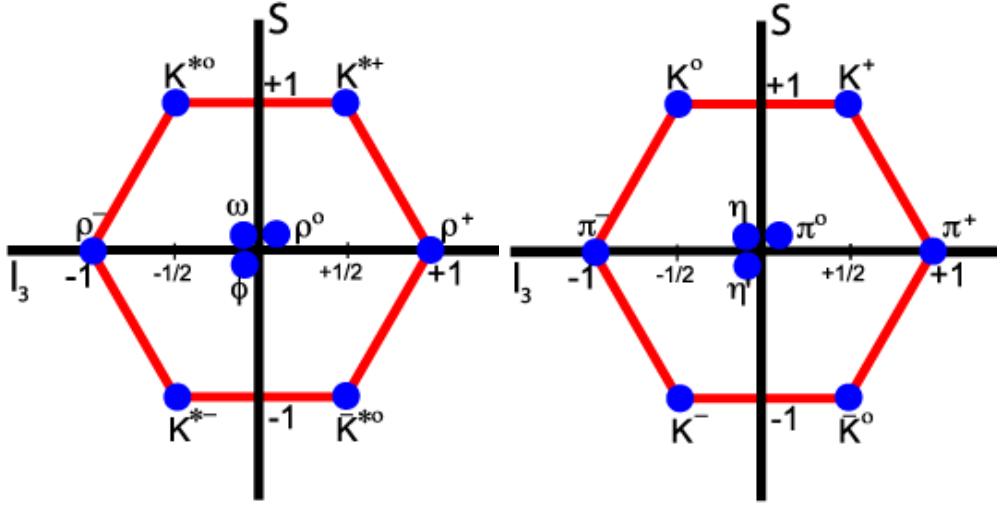
Figure 1.4: *Strangeness S versus z-component of isospin I_z for the ground state nonet of pseudoscalar and vector meson*

The flavor waves functions of both η and π mesons can then be defined as a function of the up, down and strange quarks.

$$|\pi^+\rangle = |u\bar{d}\rangle, \ |\pi^-\rangle = |u\bar{d}\rangle, \ |\pi^o\ = \tfrac{1}{\sqrt{2}}\,|u\bar{u} - d\bar{d}\rangle$$

$$|\eta\rangle_8 \ = \ \frac{1}{\sqrt{6}}\,|u\bar{u} + d\bar{d} - 2s\bar{s}\rangle$$

$$|\eta\rangle_1 \ = \ \frac{1}{\sqrt{3}}\,|u\bar{u} + d\bar{d} + s\bar{s}\rangle \ .$$

Since both octet and singlet states have the same quantum number it becomes possible to mix them and get the physical states of the η and η' meson. The octet and singlet part are mixed involving the mixing angle Θ. Its value is not well known but most estimates are in the range 20 to 25 degrees [20].

$$
\begin{aligned}
|\eta\rangle &= \cos(\Theta)|\eta\rangle_8 - \sin(\Theta)|\eta\rangle_1 \\
|\eta'\rangle &= \sin(\Theta)|\eta\rangle_8 + \cos(\Theta)|\eta\rangle_1
\end{aligned}
$$

In the next table, the main properties of a few vector and pseudo-scalar mesons are summarised. The so-called long lived mesons are the π, η and η' with a few keV width. The width of the short-lived mesons can reach something like 150 MeV in the case of the ρ. The width and life time of quantum objects like hadrons are connected by the Heisenberg relations such than the shorter the width is the longer the life time is.

Table 1.1: *Properties of the most mentioned mesons in this thesis*

.

	Quantum numbers $I^G(J^{PC})$	mass [MeV]	life time (sec)	mean free path ($c\tau$) (cm)	decays (%)	
π^o	$1^-(0^{-+})$	134.98	8.4×10^{-17}	2.5×10^{-6}	$\gamma\gamma$	98.8
					$\gamma e^+ e^-$	1.2
η	$0^+(0^{-+})$	547.45	5.5×10^{-19}	1.65×10^{-8}	$\gamma\gamma$	38.8
					$\pi^o\pi^o\pi^o$	31.9
					$\pi^+\pi^-\pi^o$	23.6
					$\pi^+\pi^-\gamma$	4.9
η'	$0^+(0^{-+})$	957.8	3.1×10^{-21}	9.3×10^{-11}	$\pi^+\pi^-\eta$	43.7
					$\rho^o\gamma$	30.2
					$\pi^o\pi^o\eta$	20.8
ω	$0^-(1^{--})$	782.59	7.8×10^{-23}	2.3×10^{-12}	$\pi^+\pi^-\pi^0$	89
					$\pi^0\gamma$	8.92
ρ	$1^-(1^{--})$	775.8	4.4×10^{-24}	1.3×10^{-13}	$\pi\pi$	100

1.3.2   Resonance classification

Study of baryon spectroscopy has been for many years a challenge since most of the predicted states have not been yet identified experimentally. The well known baryon states n, p, Λ, Σ are predicted for the SU(3) multiplet, where the lightest flavors up, down and strange are involved. Each state is a SU(3) color singlet and completely antisymmetric under any interchange of the three possible colors, blue, red, and green. As a consequence the complete state function may be written

$$|qqq\rangle_A = |color\rangle_A \, * \, |space, spin, flavor\rangle_S$$

The subscripts S and A indicate symmetry or antisymmetry under interchange of two quarks of same mass (up and down in the limit of isospin symmetry). Many models are nowadays available on the market. Old models consider the non-relativistic approach where the constituent quarks are seen as degrees of freedom and interact via the one gluon exchange approximation. In the model from [8], the baryon energies and wave function are deduced from the resolution of the Schroedinger equation for the system of three valence quarks. More recent models are based on relativised quark model and applied on both the meson spectroscopy as in [9] and to the baryons in [10]. As an example, the fig 1.5 shows for both N and Δ states the energy levels and the decay amplitude πN to the ground state.
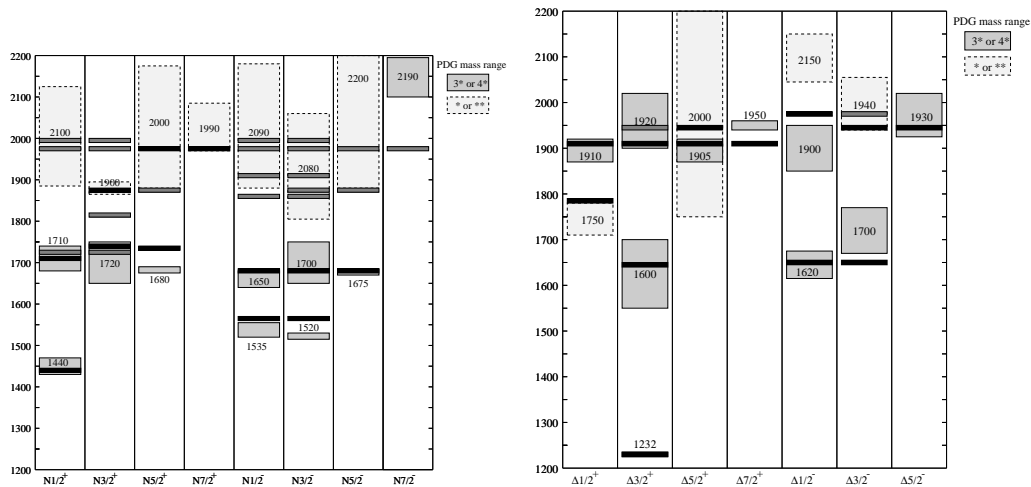
Figure 1.5: *Mass prediction and πN decay amplitudes for both N* and Δ resonances by Capstick et al. PDG data are shown as boxes, slightly shaded for one or two stars and heavily shaded for the three or four stars states. The predicted masses are drawn with a thin black line. The size of the πN amplitude is indicated by the lenght of the black shaded region*

A detailed review of the different theoritical approaches can be found in [12].

A commun notation for the resonances is given by the following expression $L_{2I,2J}(W)$ where L is the relative orbital momentum for the decay of the resonance into a nucleon meson pair. The letters I and J note for the total isospin and spin of the resonance while W is the resonance mass. In the picture (fig 1.6) the resonances are splitted according to their isospin.
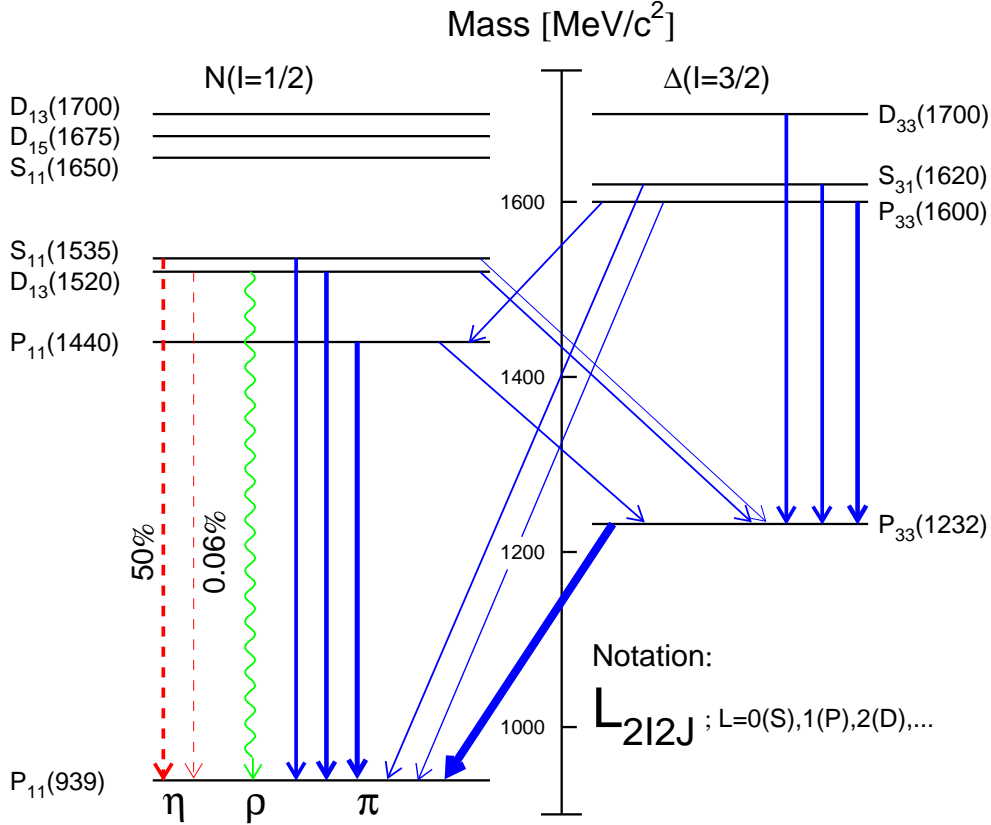
Figure 1.6: *lowest lying nucleon excited states and their decay mode to the nucleon ground state*

The first resonance region consists of the $P_{33}(1232)$ also called Δ resonance. At higher photon energy, around 750 MeV, the second region is composed of the $S_{11}(1535)$, $D_{13}(1520)$ and the $P_{11}(1440)$ resonances. The different excited states overlap within their large widths on the order of 100-200 MeV and decay back to the nucleon ground state via meson emission following the rules of the strong interaction.

Due to isospin conservation, I = 3/2 Δ resonances can only decay to isospin I = 1/2 N^*-resonances via emission of pions,while $N^* \rightarrow N$ and $\Delta^* \rightarrow \Delta$ decays can proceed via emission of pions or η-mesons.Therefore η production at low incident photon energies is dominated by decays of the N^* resonances from the second resonance region, in particular the $S_{11}(1535)$.

1.4   Theoretical predictions on in-medium mass modifications

1.4.1   The Brown-Rho scaling law

The hypothesis of the Brown-Rho scaling assumes that the scale invariance of the QCD Lagrangian is respected by effective low energy theories, in other words in-medium hadron masses display the same scaling as the chiral condensate itself. The next expression is taken from ([6])

$$m^*_{\sigma,\rho,\omega}/m_{\sigma,\rho,\omega} \approx m^*_N/m_N \approx f^*_\pi/f_\pi \approx 0.8 \qquad (1.6)$$

A drop of 20 % of the vector meson masses is expected from those calculations.

1.4.2   The density scaling of meson masses

Shortly after Brown and Rho, Hatsuda and Lee ([7]) predicted a linear decrease of the in-medium modified mass for densities within the range $0 < \rho < 2\rho_0$

$$\frac{M_{\rho,\omega(\rho=\rho_0)}}{M_{\rho,\omega(\rho=0)}} \approx 1 - 0.2 * \frac{\rho}{\rho_0} \qquad (1.7)$$

This result is in rather good agreement with the one of Brown and Rho. Further, it should be mentioned that both calculations assume mesons produced at rest which is a quite difficult condition to reproduce in experiments.

Much more sophisticated models than the simplified Brown-Rho scaling are available on the market. For the masses of ρ, ω, predictions exist that it shifts downward or upward or not at all and most of them predict significant effects on the width.

The next section deals with theoritical predictions connecting in-medium modified vector meson with baryon resonances.

1.4.3 Connecting in-medium modified vector mesons with nucleon resonances

In-medium modifications of the spectral functions of hadrons have been studied by the Giessen theory group [42]. In their model mesons and baryons are treated within a self-consistent coupled channel analysis. Mesons are dressed by the excitation of resonance-hole loops and the in-medium self-energy of the baryon resonances is calculated. The lowest orders of the Feynmann diagramms representing these effects are drawn below (fig 1.7).
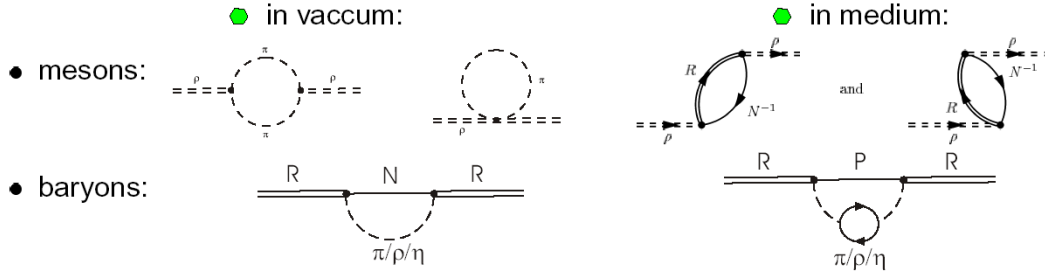
Figure 1.7: *Top left: self energy of the ρ coupling to pions Bottom left: resonance coupling to π, η or ρ Top right: self energy term, the ρ is coupled with resonances (resonances hole excitation) Bottom right: in-medium decay of a baryon resonance into a nucleon and a " dressed meson ", complete resummation of the particle-hole insertions.*

The corresponding set of equations is solved iteratively. The spectral functions of both mesons and baryons are explicitly written as function of the imaginary part of the retarded propagator

$$\mathcal{A}_M^{med}(q) = -\frac{1}{\pi}\mathcal{I}m\frac{1}{q^2-m_M^2-\Pi_{vac}(q)-\Pi_M(q)}$$
$$\rho^{med}(k) = -\frac{1}{\pi}\mathcal{I}m\frac{1}{k^2-m_R^2-\Sigma_{med}(k)}$$

where k and q are the momentum of the corresponding particles while m_M and m_R stand for the masses. The quantity Σ_{med} is the self energy of the in-medium meson and contains the particle-hole states. The self-energy terms for the resonance in-vacuum and in-medium are denoted by Π_{vac} and $\Pi_M(q)$, respectively.

As a result of the calculations the spectral function of the ρ vector meson presents quite significant deviations compared to the in-vacuum lineshape. The spectral function appears much broader and a peak structure is appearing on the left falling tale of the spectral function arises from the coupling of the ρ-meson to the $D_{13}(1520)$ resonance (fig 1.8).
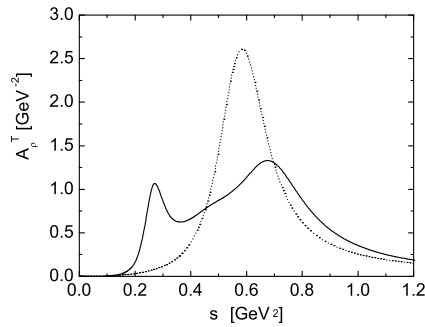
Figure 1.8: *Dotted line : In-vacuum spectral function of the ρ meson. Solid line : In-medium spectral function of the ρ.*

The spectral functions of both the $S_{11}(1535)$ and $D_{13}(1520)$ resonances are also calculated and shown in (fig 1.9)
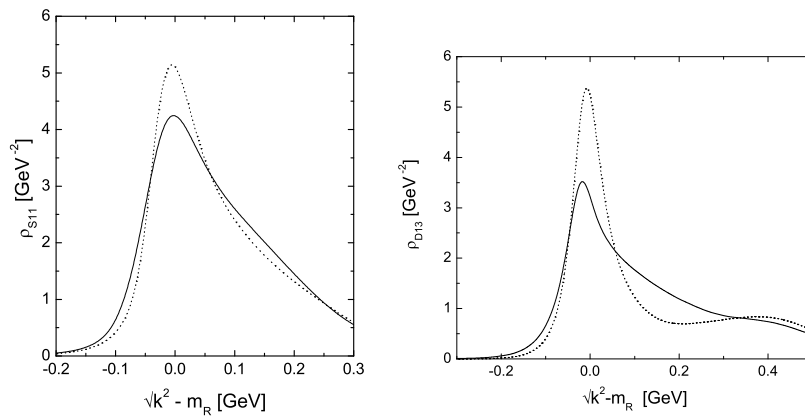
Figure 1.9: *left plot : spectral function of the $S_{11}(1535)$ the right one stands for the $D_{13}(1520)$*

In the case of the $S_{11}(1535)$ very small modifications are expected. A larger effect is predicted for the $D_{13}(1520)$. The left part of the tale remains almost unmodified whereas the right part shows a smoother decrease of the spectral curve. This effect is explained by the fact that a relatively strong interplay is found between the ρ vector meson and the $D_{13}(1520)$. A shift of the spectral strenght of the ρ spectrum is expected towards smaller invariant masses leading to a broadening of the $D_{13}(1520)$.

1.5 Experimental evidence for in-medium hadron modifications

During the last decade, several experiments have measured in-medium modified hadron properties. This section presents a few of them. Recent results from heavy ion collision experiments are shown and a comparison with photo-production experiment is done for the ω vector meson.

1.5.1 Di-lepton invariant masses

Historicaly, one of the first experimental result has been reported by the CErenkov Ring Electron Spectrometer (CERES) collaboration. The experiment has been caried out at the Super Proton Synchrotron SPS at CERN. The invariant mass of dilepton pairs e^+,e^- has been measured for p-p, p-A and A-A collisions. An enhancement of the invariant mass of the dilepton pairs has been reported in the kinematical region above 0.250 GeV in the heavy ion collisions as seen in (fig 1.10). The surplus yield is generally attributed to direct thermal radiation from the fireball, dominated by the two-pion annihilation $\pi^+\pi^- \to \rho \to l^+l^-$ with an intermediate ρ strongly modified by the medium.

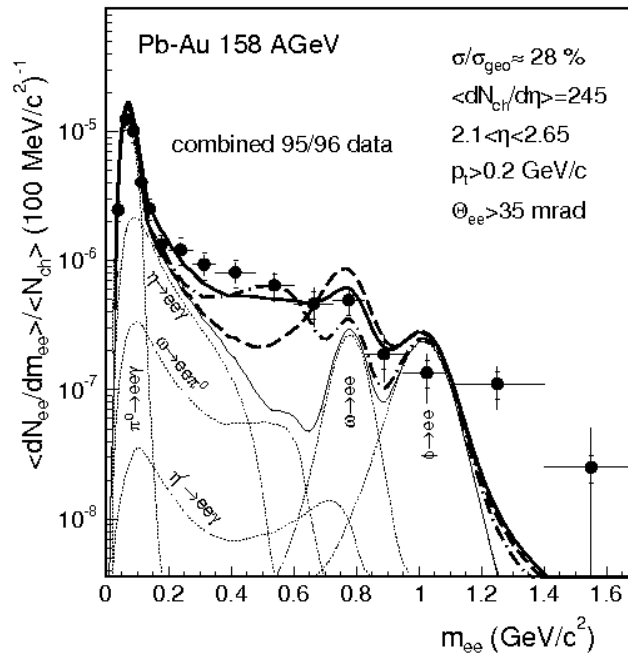Figure 1.10: *comparison of the inclusive CERES dilepton invariant mass to different theoritical predictions. (i) thin solid line : free hadron decay without ρ decay (ii) thick dashed line : calculations with a vacuum ρ spectral function (iii) thick dot-dashed line : dropping in-medium ρ mass (iv) thick solid line : with a in-medium modified ρ spectral function. Picture from [43]*

Full calculations with vacuum ρ fail to describe the characteristic shape of the spectrum of the excess dileptons. The two models incorporating in-medium modification of the ρ more or less reproduce the invariant mass picture but are based on complete different concepts. While the Brown-Rho scaling hypothesis explicity refers to restauration of chiral symmetry, the many-body spectral function approach of Wambach et Rapp does not have chiral symmetry as a key point. The statistical accuracy and mass resolution were not sufficient at that stage to reach any sensitivity on the charactere of the in-medium changes. The structure of the ω meson cannot be resolved and appears to be melted with the broad ρ meson spectral function.

Recent results from the NA60 experiment have been reported with a much better resolution than before. Low-mass muon pairs have been studied in 158 AGeV Indium-Indium at the CERN SPS [14]. A strong excess of pairs is observed above the expectation from neutral meson decays. This excess is isolated by subtraction of the known source. The shape of the resulting mass spectrum is consistent with a dominant contribution from $\pi^+\pi^- \rightarrow \rho \rightarrow \mu^+\mu^-$ annihilation. The dimuon mass spectra is shown in fig 1.11. The net spectrum contains 360000 pairs with a mean signal to background ratio of 1/7. Both vector mesons, ω and ϕ, are clearly visible and a peak structure corresponding to the η meson is seen for the first time in heavy ion collision history.
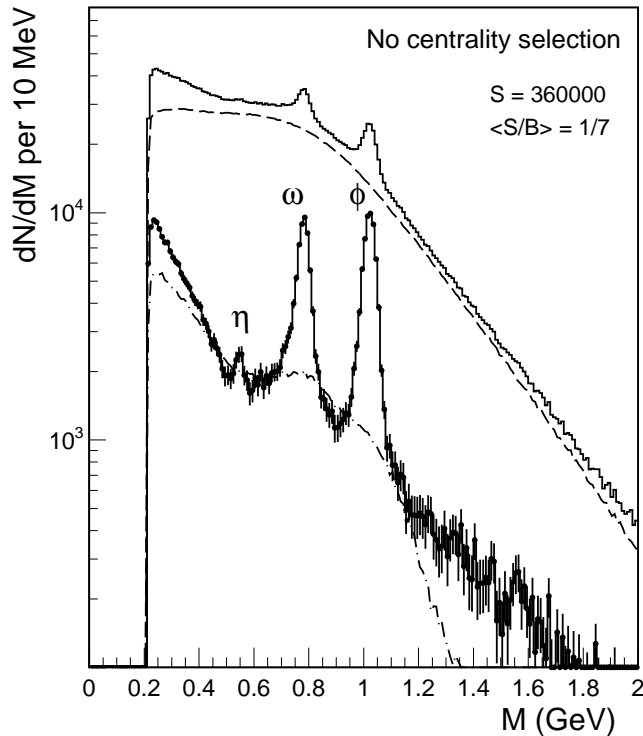

Figure 1.11: *Dimuon mass spectra of the total data (upper histogram), combinatorial background (dashed), fake matches (dot-dashed) , and net spectrum after subtraction of the former two(lower).*

The associated ρ spectral function shows a strong broadening but no shift in mass as seen in fig 1.12.
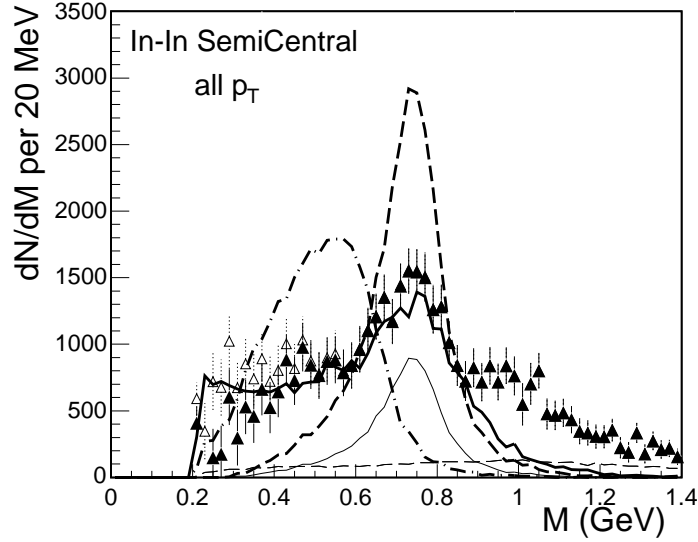
Figure 1.12: *Comparison to model predictions ,made for In-In at $dN_{ch}/d\eta = 140$. Unmodified ρ(thick dashed), in-medium broadening ρ (Rapp/Wambach, thick solid), in-medium moving ρ (related to Brown/Rho scaling, dot-dashed). The open data reflects the change in the difference spectrum resulting from a decrease of the η-yield by 10 %.*

Another approach considers photo-nuclear reaction. The density and temperature of the matter reached with heavy ion collisions are in comparison much higher and therefore should show more significant indication of in-medium effects. Nevertheless more degrees of freedom have to be taken into account and data are much more complicated to interprete. During a photo-nuclear reaction the probability for a photon to interact with a nucleon is the same at any place of the nucleus, therefore all densities of the static density distribution are probed and in principle evidences of in-medium hadron modifications should be visible.

1.5.2   Modification of the ω invariant mass

A shift of the ω invariant mass in its $\pi^0\gamma$ channel towards lower mass at low momentum has been observed with the CBELSA/TAPS experiment and recently been published in [15]. One of the main result is shown next (fig 1.13). The branching ratio of the reaction $\omega \to \pi^0\gamma$ is three orders of magnitudes higher than for the reaction channel $\rho \to \pi^0\gamma$. This effect allows a clear identification of the ω invariant mass signal in comparison to the invariant mass of dilepton pairs in the sense that the interference ρ - ω does not matter. A disadvantage is that the π^0 may rescatter whithin the nuclear volum and obscur the interpretation of the ω signal.
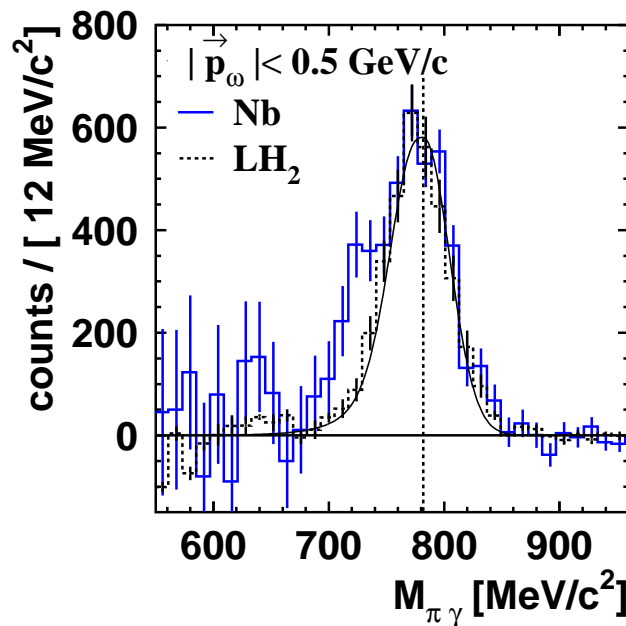
Figure 1.13: $\pi^0\gamma$ invariant mass for Niobium data (Solid histogram) and liquid hydrogen data(dashed histogram) after background substraction. The errors bars are only statistical .

The invariant mass picture for Niobium shows the superposition of decays outside of the nucleus at the nominal vaccum mass and decays produced inside the nucleus and therefore sensitive to in-medium modifications. This last part is responsible for the shoulder visible at the left part of the falling tale. A Voigt fit has been applied to the data and an ω in-medium mass of $M_{medium} = [722^{+2}_{-2}(stat)^{+35}_{-5}(syst)]$ MeV/c^2 has been obtained. This mass drop of 8% is consistent with the scaling law of the ω mass $m = m_0(1 - 0.14 * \rho/\rho_0)$ predicted by [6], assuming an average matter density of $0.6\rho_0$. The observed in-medium shift of the ω should be compared with the results from Na60. Further results from the Na60 are expected to get a more detailed comparison with the result from the CB/TAPS collaboration.

1.5.3   Total photoabsorption cross section

The total photoabsorption cross section on the free proton measured by ([16]), ([17]), ([18]) shows different bump like structures corresponding to the excitation of the different resonance regions (fig 1.14). The first bump structure around photon energies of 300 MeV corresponds to the excitation of the $P_{33}(1232)$ also called the Δ resonance. At higher photon energy additional bump like structures around 750 and 1050 MeV are observed and correspond to the second and third resonance region. The "universal curve" (average over nuclear data from lithium to uranium) shows a broader structure of the Δ resonance but a complete disappearance of the second and third resonance region. Many effects are suggested to explain this depletion. The Fermi motion of nucleons may induce a smearing effect on the resonance lineshape. The resonance width may be reduced due to the Pauli principle which means that the same quantum state can't be occupied by two fermions. A broadening of the width can be induced by collisional broadening of resonance propagation (i.e by the $NN^* \to NN$ channel).
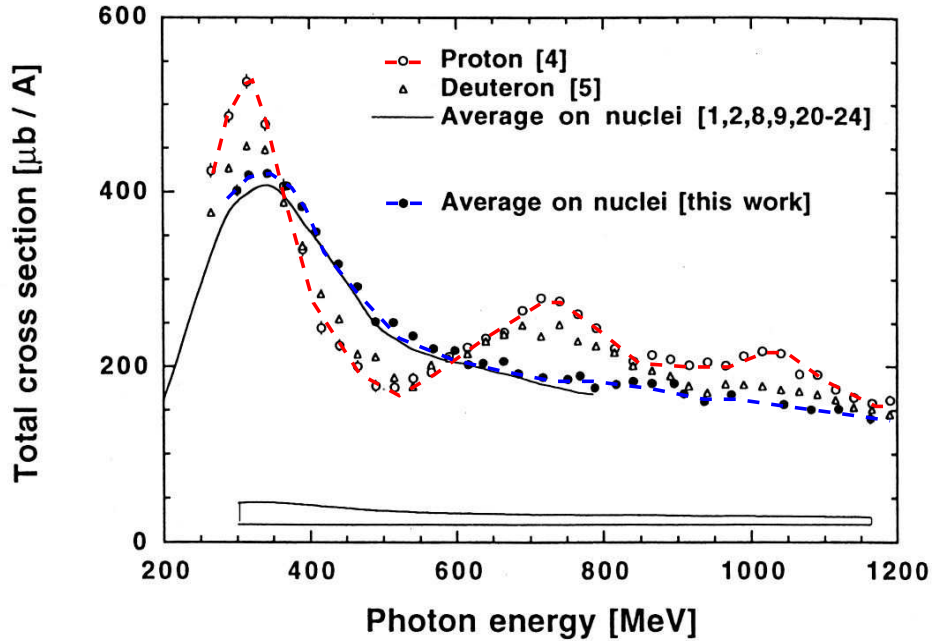
Figure 1.14: *Comparison of the total photoabsorption cross section on the proton and heavier target*

The interpretation of the total photoabsorption spectrum is already uneasy on the proton target since the bump of the second resonance region is composed of the $S_{11}(1535)$, the $D_{13}(1520)$, and the $P_{11}(1440)$ resonances, which overlapp due to their width and peak position. The understanding of the picture from Bianchi et al. may then require to undertand the properties of each resonance individually.

1.6 Resonance investigation via meson photo-production

1.6.1 Interest of photoproduction

Both hadron and photon beams suffer from final state interactions of the produced meson with the nuclear matter. Furthermore hadron beams also undergo initial state interaction since the nucleons can't freely get to the inner part of the nucleus. In consequence those kind of beam will only probe the surface of the nucleus where a much lower density is expected. Photon beams illuminate the full nucleus with the same interaction probability and therefore probe the density of the inner part where larger effects are expected.

1.6.2 The η and $S_{11}(1535)$ resonance

The η photoproduction is dominated at the reaction threshold by the $S_{11}(1535)$ resonance. This feature is explained by the high branching ratio of 50 % of this resonance into the ηN channel. The η meson cross section turns out to be a promising probe to measure the properties of the $S_{11}(1535)$.

The dominant mechanisms leading to the creation of the η meson at threshold can be seen next using the Feynmann diagram pictures. Those diagramms represent two-body final states where an η meson and a nucleon are present.
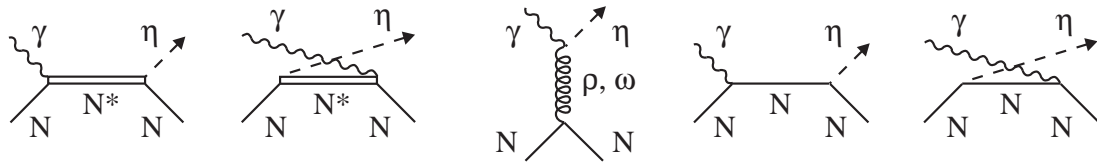
Figure 1.15: *Feynmann diagramms contributing to the η photoproduction*

The first two plots on the left illustrate the creation of an η where a resonance is involved. The s-type diagram represents the usefull process to investigate the properties of the resonance while the u-type contributes to background. The middle plot represents vector meson exchange and the last two plots on the right are Born terms. At high photon beam energy, far from the threshold more particles can be created and therefore other reaction mechanisms to the η background like three body decays should be considered. The next picture (fig 1.16) compares the η cross section measured on both a proton and a carbon target.

Figure 1.16: *Cross section of the η photoproduction On the proton : open circle data from [25], squared [26] On the carbon : open circle from [13], full circle LNS*

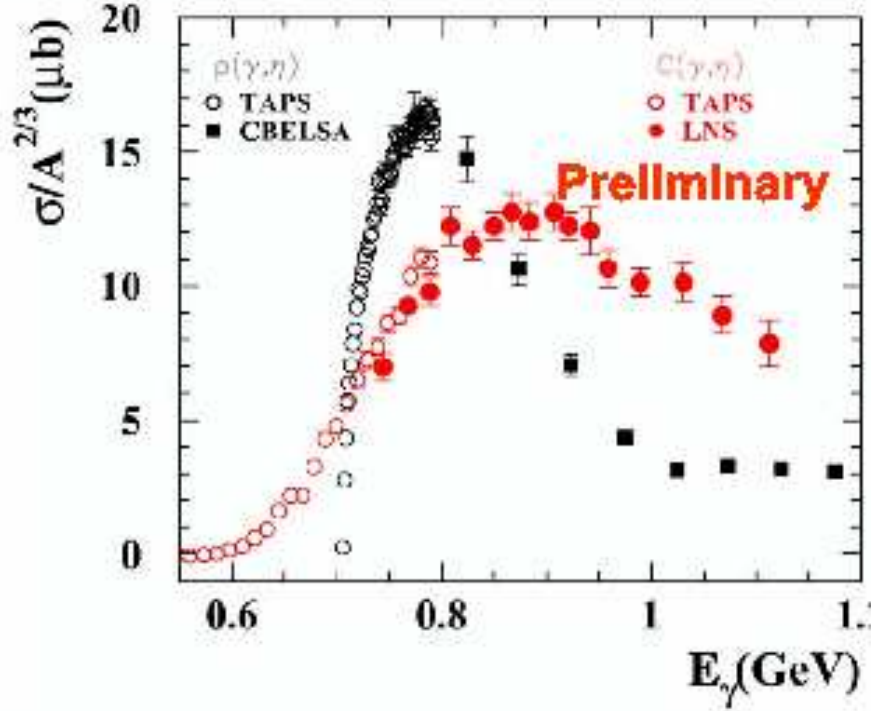In the carbon case the peak seems shifted towards higher photon beam energies and the width of the $S_{11}(1535)$ looks broader. The η cross section for Carbon was measured using the reaction decay $\eta \rightarrow 2\gamma$.

The η cross section off proton was measured using the decay channel $\eta \rightarrow 3\pi^0 \rightarrow 6\gamma$ during the CBELSA experiment at Bonn.

The η cross section off proton measured with the TAPS detector at Mainz has been exctracted using the decay channel $\eta \rightarrow 2\gamma$.

A further point should be mentionned that on the proton target some attempts to isolate the single η production have been applied like missing mass methods and identification of the correlated nucleon. This difference might play a significant role at high photon energies where some background may contribute as seen in a later chapter. Furthermore the available photon energies at that time was not high enough to cover the entire lineshape of the $S_{11}(1535)$ lineshape.

Earlier results for the η photoproduction cross section have been obtained with incident photon beam energies up to 800 MeV in Mainz in order to investigate the in-medium properties of the $S_{11}(1535)$ resonance. Different nuclei have been studied for that purpose.
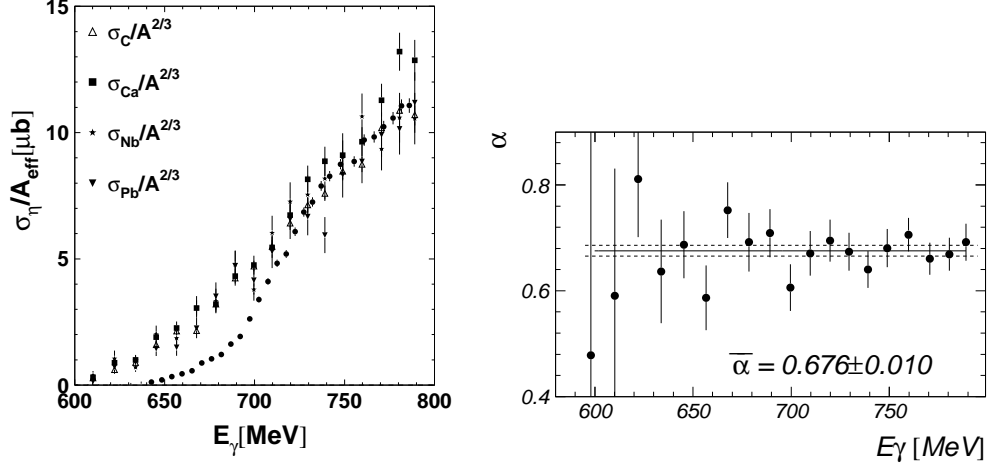

Figure 1.17: *Left : η cross section off nuclei normalized by the scale factor $A^{2/3}$ Right : Determination of the scale factor through the available beam range*

The cross sections of the different nuclei have been fitted using the ansatz $\sigma_A = A^\alpha$. The determination of the scale factor α has been done for different values of the incident photon energy.

An average value of 2/3 has been extracted for the scale factor α. A value of α close to unity would indicate scaling of the cross section with the number of nucleons (nuclear volume) which would be the case for a small absorption probability of the η meson. In the present case the value 2/3 tells that the meson can only be detected if produced at the surface of the nucleus. This reflects a strong absorption effect of the η meson inside the nuclear matter.

The η mean free path has been extracted from the data and evaluated around 2 fm using the framework of the Glauber model [13]. The mesons produced deep inside the nucleus have in fact no chance to be detected. This interesting feature has been predicted in the BUU transport code by the Giessen theory group. More details about the BUU simulations can be found in a later chapter of this thesis and also in [39].

More recent experiments at LNS(Japan) [22], [23], and [24] have been carried out up to 1.2 GeV photon beam energy as shown in (fig 1.18) and compare the η cross sections from two different nuclei.
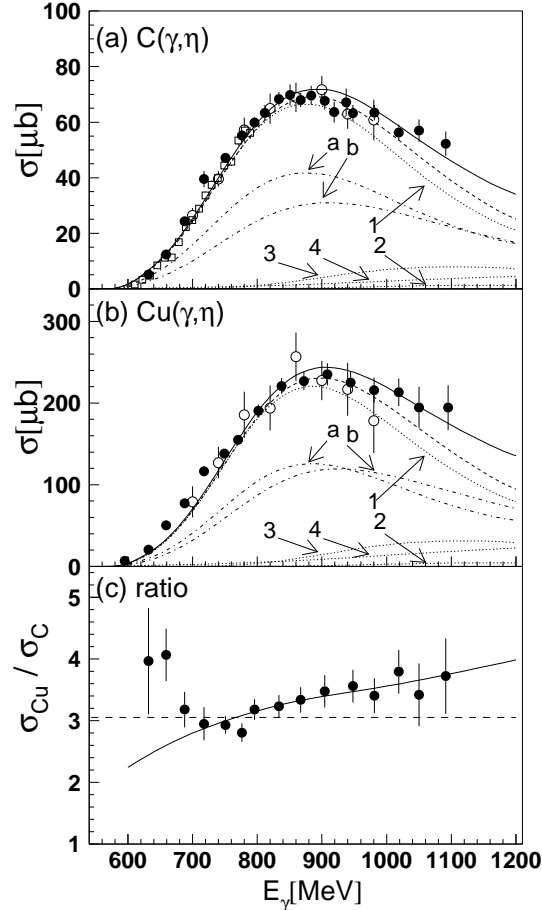
Figure 1.18: *Cross sections of η photoproduction measured on Carbon (a) and Cupper (b). Solid circles are from [24]. Open circles are from [22] and squares points from [13]. (c) shows the ratio of the cross section of the $Cu(\gamma, \eta)$ to that of the $C(\gamma, \eta)$ reaction. The dashed line shows the ratio of $A^{2/3}$ (A: mass number). The solid line is the result of a Quantum Molecular Dynamic calculation.*

A systematic deviation from the scale factor $A^{2/3}$ is found for photon energies higher than 850 MeV. This result is a first attempt to indicate a dependence of the cross section on the target mass. In the present work, the cross sections for nuclei have been measured with photon energies up to 2.2 GeV for four nuclei. These conditions allow to study in more detail possible in-medium dependencies of the resonance properties and the η meson interaction with nuclear matter can be studied for a much larger kinetical range than before.

1.6.3   The $\pi^0\pi^0$ channel and the $D_{13}(1520)$ resonance

The $\pi^0\pi^0$ total cross section has been measured for different targets in the past years by different collaborations. The TAPS, DAPHNE and GRAAL collaboration [40],[31], [32] have measured the cross section on the proton for different photon beam energy ranges. The importance of the $D_{13}(1520)$ resonance to this decay channel has been predicted by ([30]).

The $D_{13}(1520)$ decays into the double π^0 channel with an average branching ratio between 15 to 25 %. The full lineshape of this resonance can then be extracted when measuring the cross section of this reaction. The double π^0 photoproduction cross section was measured on the proton at ELSA (Bonn) and is shown here for a photon energy up to 1.6 GeV(fig 1.19)
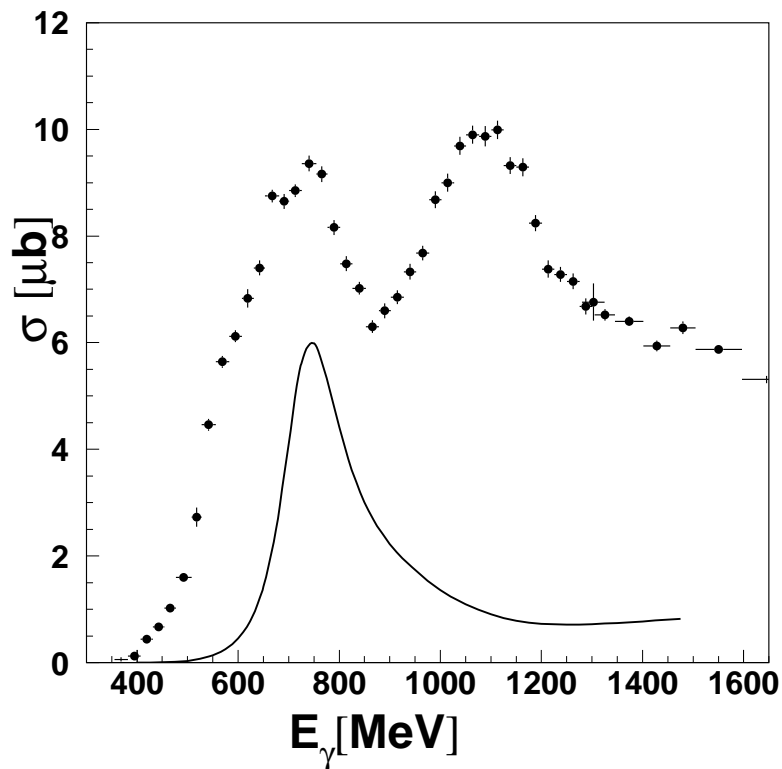

Figure 1.19: $\pi^o\pi^o$ photoproduction from proton [29]. The both second and third resonance are visible as in the total photoabsorption cross section. The contribution of the $D_{13}(1520)$ is also shown as a solid line. Calculation from [33].

The contribution of the $D_{13}(1520)$ is shown at the reaction threshold of the double π^0 channel.

The double π^0 total cross section off nuclei was measured in Mainz by the TAPS collaboration [19] with a maximum photon beam energy of 800 MeV. Several nuclear targets have been used to probe different nuclear average densities (fig 1.20)
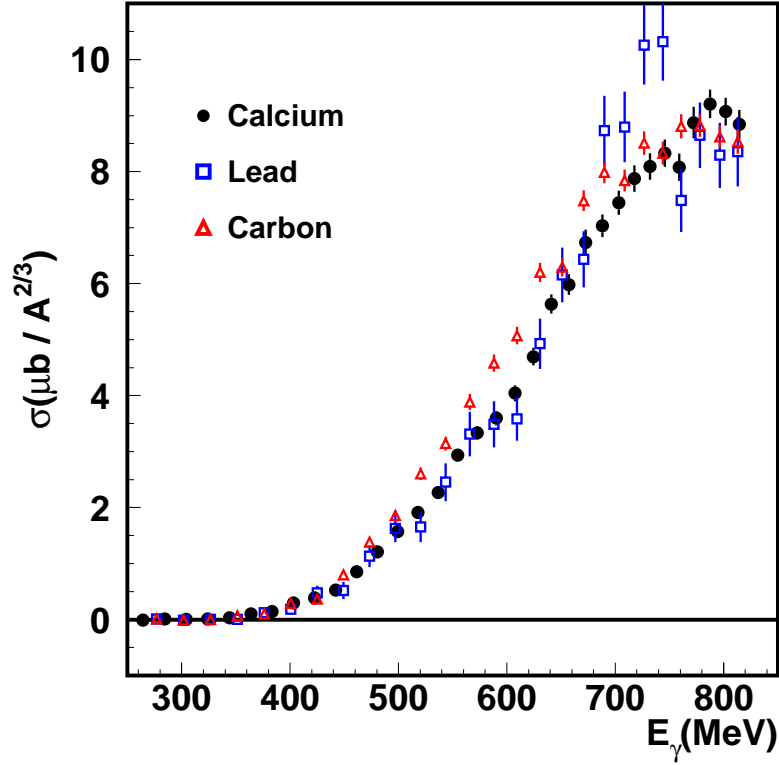
Figure 1.20: *$\pi^o\pi^o$ photoproduction from Carbon, Calcium and Lead. Cross sections are normalized with $(A^{2/3})$ indicating strong final state interactions of the π^0 with the nuclear matter. Picture from PhD thesis of F.Bloch [28]*

The total cross section off nuclei shows slight differences to the proton target that presents a maximum around 750 MeV. In case of the nuclei the rise seem to be constant up to 800 MeV. This thesis work aims at a measurement of double π^0 cross section up to energies of 1.4 GeV. Studing the lineshape of the $D_{13}(1520)$ through the entire energy range of the second region and a search for in-medium effects on the resonance properties should give valuable information to interprete the total photoabsorption cross section. As for the η cross section a scale factor of $A^{2/3}$ is used to normalize the different cross sections. This indicates strong final state interactions of the π with the matter.

1.7   Theoritical models

1.7.1   The Glauber approximation

This model predicts quasifree photoproduction from nuclei. It is based on the knowledge of the elementary production cross section from the nucleon and the absorption cross section of the reaction products. This work was originaly performed by Koelbig and Margolis [46]. A more recent version of this model has been developed by Vercellin et al. [47] The model is only valid for quasifree production and is used during the data analysis to extract the values of the absorption cross section. Mesons are produced off the nucleon like $if \rightarrow fY$ with a certain cross section σ_i. The absorption of the produced meson by nucleons is defined by σ_f. The cross section of the reaction $iA \rightarrow fY$ should scale like the mass number A if the absorption cross section is negligible. The next sketch illustrates the mechanism of the particle production in the Glauber model fig 1.21
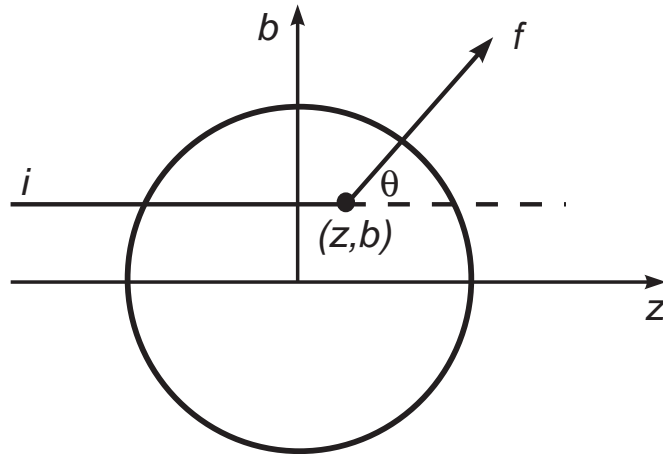

Figure 1.21: *Particle production in the Glauber approximation. An incident particle i interacts with a nucleon at a certain position given by the coordinates (z,b). A particle f is produced and can either escape the nucleus or get absorbed.*

The prediction of the Glauber model for the total cross section is given by

$$\sigma_{tot}^{Glauber}(A, E_\gamma) = \sigma_1(E_\gamma) \times A_{eff}(E_\gamma)\frac{Z + N \times k_{np}}{A} \qquad (1.8)$$

σ_1 is the Fermi smeared elementary cross section measured on a proton target k_{np} is the ratio of neutron and proton cross section.

The extraction of the absorption cross section is done by considering the A-scaling law instead of the absolute cross section. The advantage is that many systematic effects from approximations made in the model and systematic errors in the experimental cross sections cancel in the mass dependence. Therefore, the Glauber cross section is calculated as function of the mass number and the absorption cross section and the mass dependence is fitted with an A^α scaling law. A direct relation can then be

made between the absorption cross section and the scale factor α determined from the experiment.
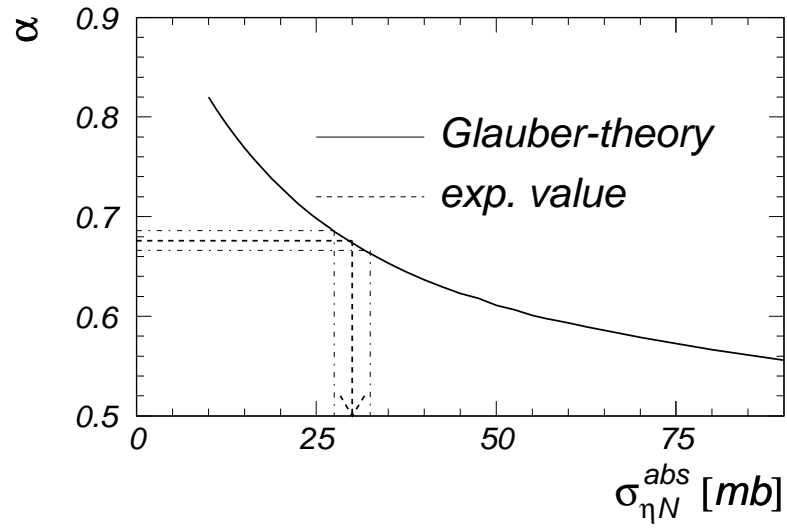

Figure 1.22: *correspondance between the fitted scale factor and the absorption cross section $\sigma_{\eta N}$*

1.7.2   The BUU transport code

The Boltzmann-Uehlig-Uhlenbeck (BUU) transport model was originaly developped to describe heavy ions collisions. The final state interactions are described within a semiclassical coupled channel transport model. The spectral phase space distributions $F_i(r, p, \mu; t)$ give the probability to find a particle of a certain class at a certain time with a mass μ and momentum p at a position r. Its time-development is determined with the following BUU equation

$$(\frac{\delta}{\delta t} + \bigtriangledown_p H_i \cdot \bigtriangledown_r - \bigtriangledown_r H_i \cdot \bigtriangledown_p) F_i = G_i A_i - L_i F_i \qquad (1.9)$$

H_i contains information about energy, mass, selfenergy (mean field) of the particle and a term that drives back an off-shell particle to its mass shell. Its litteral expression can be written as

$$H = \sqrt{(\mu + S)^2 + p^2} \qquad (1.10)$$

The rhs also called drift terms describe both the possibility of particle production and absorption. More explicits details about the application of this model to η and π photoproduction can be found in [39]. the constituants of the nucleus are defined as 'test nucleons' and follow a Woods-Saxon density distribution
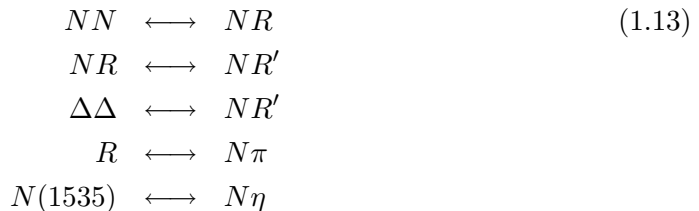
$$\rho(r) = \frac{\rho_o}{1 + e^{(r-R)/a}} \quad , \qquad (1.11)$$

where the nuclear radius is related to the nucleus mass via
$R = 1.124 A^{1/3}$ and $a = (0.0244\, A^{1/3} + 0.2864) fm$.
The momentum distribution is described with the Fermi gas theory.

$$p_F(r) = \left(\frac{3\pi^2}{2}\rho(r)\right)^{1/3}. \qquad (1.12)$$

The elementary η cross sections off protons and neutrons are included in this model. The produced resonances and mesons propagate in the nucleus and can be scattered, absorbed or decay. The different reaction probabilities are either fitted to experimental data or calculated. They are incorporated into the model by the collision term and may interact according to the geometrial condition that the distance between the two particles is smaller than the impact parameter $b_c = \sqrt{\sigma/\pi}$ where σ is the reaction cross section probability. The model includes the following channels:

$$
\begin{aligned}
NN &\longleftrightarrow NR \qquad\qquad (1.13)\\
NR &\longleftrightarrow NR'\\
\Delta\Delta &\longleftrightarrow NR'\\
R &\longleftrightarrow N\pi\\
N(1535) &\longleftrightarrow N\eta
\end{aligned}
$$

The interesting feature of secondary η 's created during the reaction $\gamma N \to \pi N \to N^\star \to N\eta$ is also implemented in the model.

The effects on the η cross section due to the nuclear environment are shown in the picture (fig 1.23).
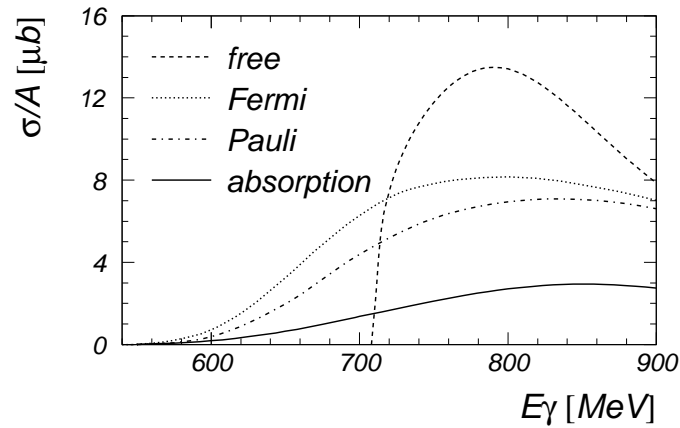

Figure 1.23: *Total cross section per nucleon for quasifree η photoproduction from lead from the BUU calculation of Hombach et al. The elementary cross section on the proton is plotted with dashed lines. The influence of the Fermi smearing, Pauli blocking, and absorption are denoted with dotted, dot-dashed, and solid lines, respectively.*

Early works on the η production mechanism have highlighted the interesting feature that most of the detected η meson have to be produced in a low density area, (so mainly at the surface of the nucleus) as seen in fig 1.24. Another feature that has been predicted for the lead target is that only 10 % of the observed η particles have been absorbed and reemitted. A majority of the η meson are observed "free" of final state interactions.
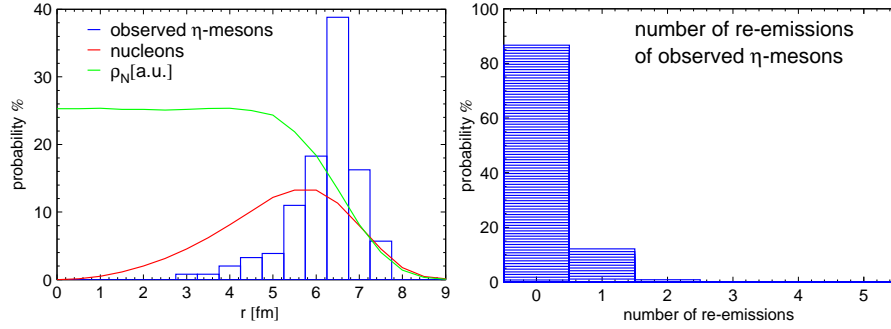
Figure 1.24: *Left plot : Spatial distribution of the observed η meson as function of its creation point. Right plot : Number of possible absorption and reemission of the η.*

The BUU transport code model predicts a different behavior for the π compared to the η.

Figure 1.25: *Probability for a pion to be detected as function of its production point. The detected pion may undergo several rescattering before leaving the nucleus.*

Those π final state interactions should therefore be taken into account to interpret the cross section.

On-going simulations are on the way to interprete total and differential cross sections for the η production off nuclei. The different contributions should first be measured from the proton target and then use to simulation the reaction process from nuclei. (fig 1.26)
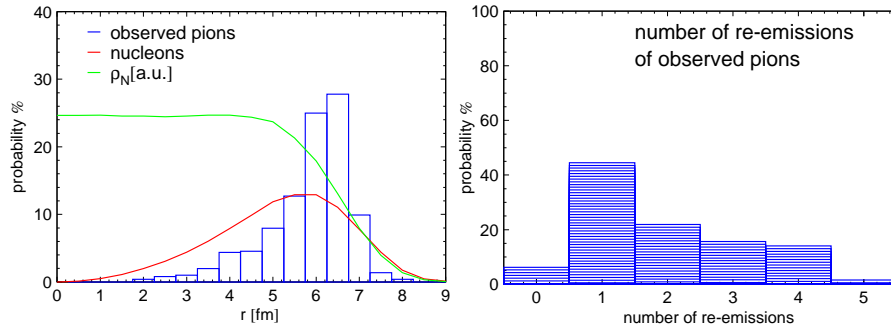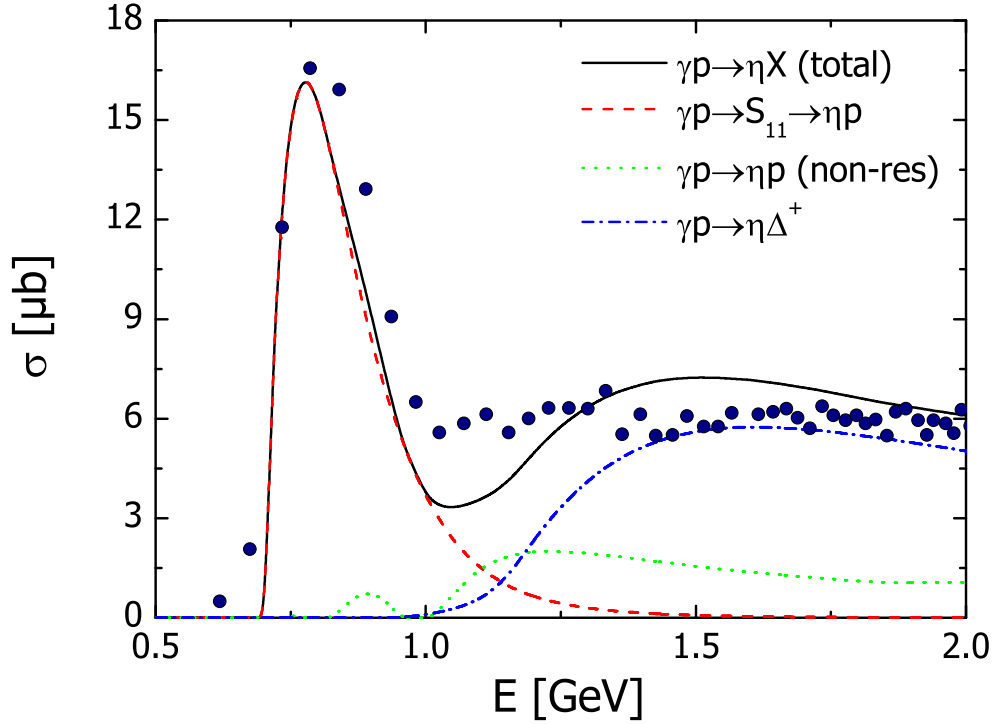

Figure 1.26: *Contribution of the different sources to the η production off proton.*

In this plot, a fit of the exclusive $\gamma + p \to \eta + p$ cross section is shown as a dashed line. The cross section of the reaction $\gamma + p \to \eta + \pi^0 + p$ measured by [34] is used to determine the $\eta\Delta^+$ channel. The sum of all the known contributions to the η production is compared with the measured fully inclusive total η cross section. A discrepency between both quantities is visible for photon energies between 1 and 1.3 GeV. The so-called Kroll-Rudermann term consists of the reaction channel $\gamma + p \to \pi^+ + S_{11}$ where a first charged π is emitted. Finally the $S_{11}(1535)$ resonance decays into an η and neutron. This channel would correspond to the resonance lineshape shifted by the pion mass towards the high photon beam energies. Some calculations are on the way in order to estimate the strenght of this reaction.

Chapter 2

Experimental Setup

2.1   The Electron stretcher and Accelerator (ELSA)

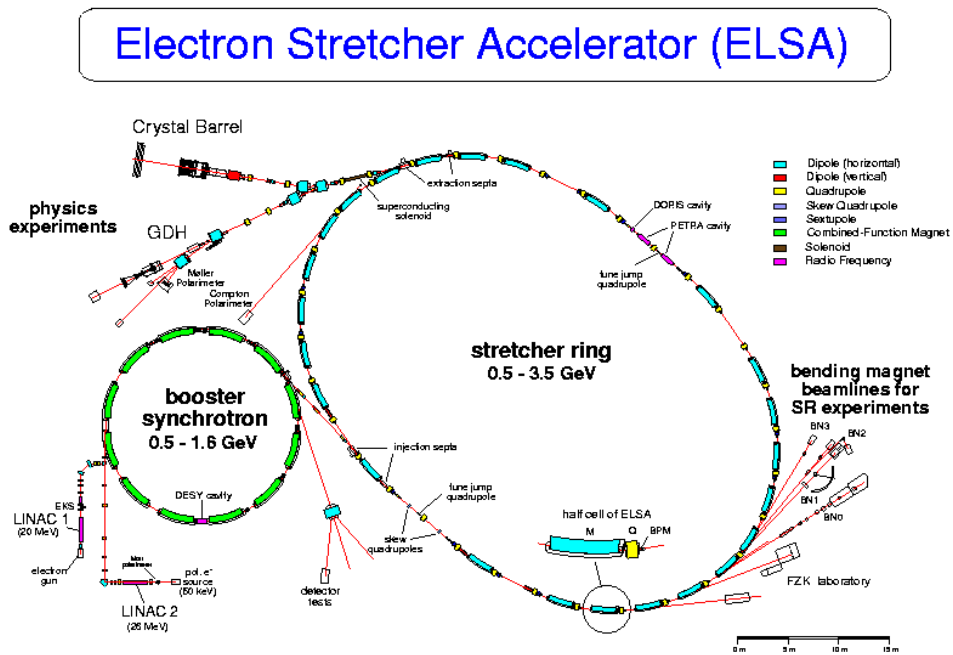The ELectron Stretcher and Accelerator and its main components are shown in top view in (fig 2.1).

Figure 2.1: *Top View of the Electron Strecher Accelerator complex in Bonn (Germany)*

The accelerator has been in operation at the University of Bonn (Germany) since 1987. The electrons are first accelerated with the LINAC system where they can reach energies up to 20 MeV. The electrons are then injected into the booster synchrotron to reach energies up to 1200 MeV depending on the chosen energy. Then the electrons are filled into the stretcher-ring to reach the maximum energy of 3.5 GeV. The electrons are then next delivered to the experimental area. The real photons produced via Bremstrahlung (see the Tagger section for more details) will be used to initiate the nuclear reactions. The decay particles will be collected using the combined setup of the Crystal-Barrel and the TAPS detector. This configuration provides an almost 4π solid angle coverage, suitable for multi particle final states. A sketch of the beamline setup is given in (fig 2.2). The different parts of the setup are presented in the next sections.
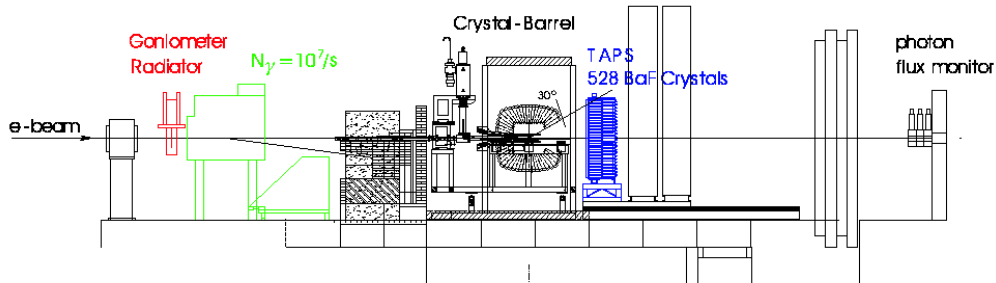

Figure 2.2: *Sideview of the fully mounted beamline setup. From left to the right : The radiator where real photons are produced via Bremstrahlung, The Tagger system, The Crystal-Barrel, The TAPS detector and the Photon flux monitor*

2.2   The Tagger system

A schematic overview of the tagging system is given in fig 2.3. The basis of the TOPAS-II ([35]) tagging system consists of 14 plastic scintillator bars each fitted with a photo-multiplier on both ends. A second layer is made out of 480 scintillating fibres to provide a higher granularity. The accelerated elecrons are passing through a thin copper foil of 0.3 % radiation length. The interaction of the incoming electron with the field of a nucleus results in the creation of a real photon. The momentum transfer to the nucleus is assumed to be negligible such that the simple relation $E_\gamma = E_{beam} - E_{e^-}$ is valid.

The beam energy was fixed at 2.8 GeV for this experiment. The energy of the photon inducing the nuclear reaction can therefore be deduced since the energy E_{e^-} of the deflected electron is known from the tagger reconstruction.
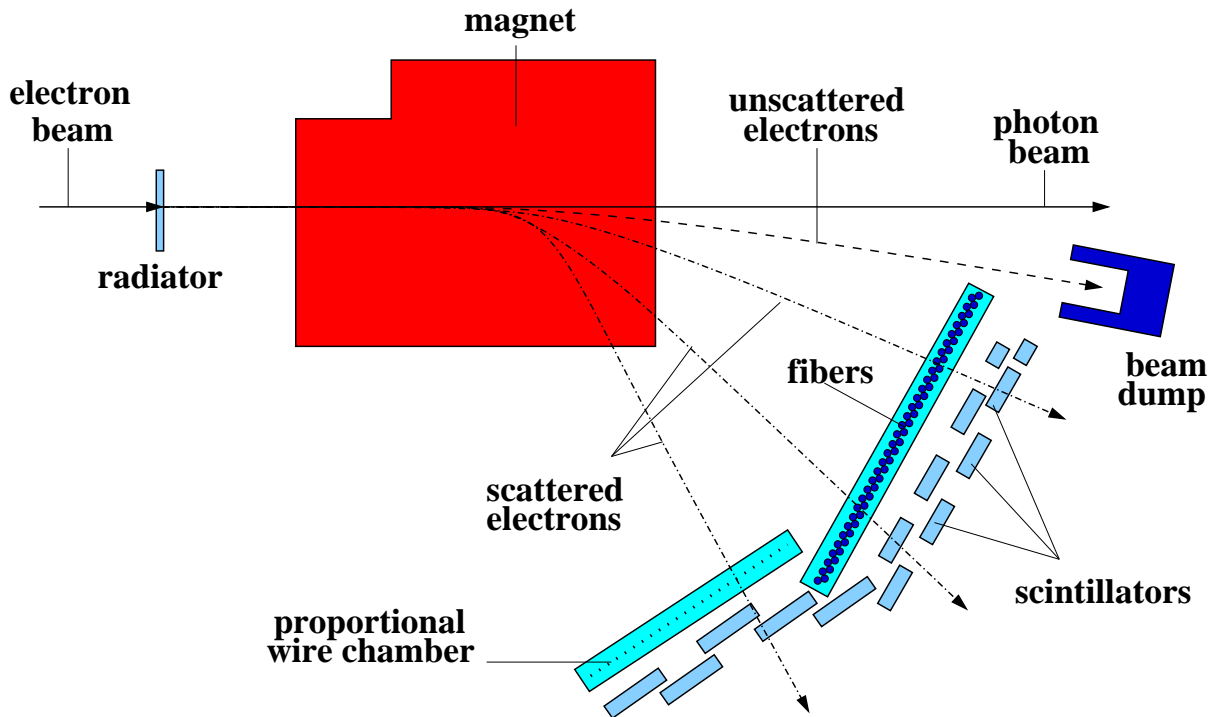
Figure 2.3: *Sketch of the tagging system. A real photon is produced in the radiator and will continue to the target. The scattered electrons are collected in the tagger system and pass first through the fibres and finally stop in the bars. The beam dump will collect all electrons that have not produced photon via bremstrahlung.*

2.3 The TAPS detector

The TAPS detector is an electromagnetic calorimeter well suited to detect photons. Other particles like protons, charged pions, or neutrons may also be detected. The main interaction mechanism between the incoming photon and the BaF_2 is the creation of e^- e^+ pairs. Each e^- and e^+ interacts with the scintillator and create a photon by Bremsstrahlung of decreasing energy. An electromagnetic shower is produced. When the energy of the particles is low enough, their energy is populating the excited states of the scintillator. The deexcitation of those states will lead to scintillation light which is then collected by the photomultipliers (PM) connected optically to the back of the scintillators.

In (fig 2.4) a sketch of a single TAPS-module is shown.
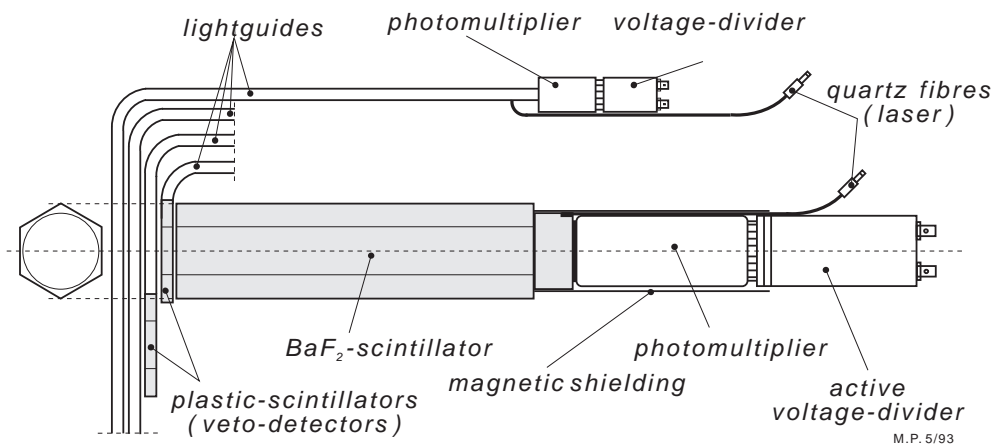
Figure 2.4: *Drawing of a BaF_2 scintillator with its photomultiplier and veto detector.*

The BaF_2 crystal is 25 cm long and has an inner diameter of 5.9 cm (fig 2.5) The density of the crystal is 4.89 g/cm^3, its radiation length is 2.05 cm, and the Moliere radius is 3.4 cm.

Figure 2.5: *Picture of a single BaF_2 crystal and a fully mounted detector element with its photomultiplier where the crystal is covered with black tape.*

528 BaF$_2$ modules are mounted in the forward direction to form a supercluster having an hexagonal shape, as can be seen in (fig 2.6)
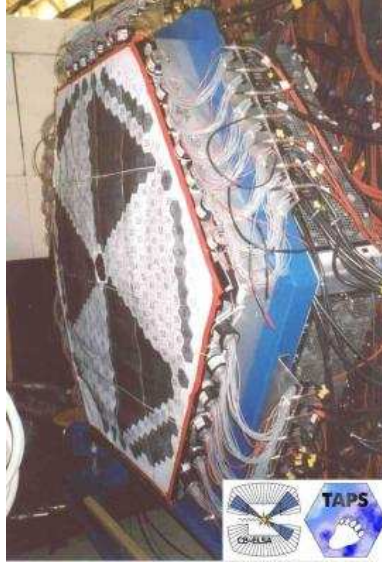
Figure 2.6: *of the fully mounted 528 BaF$_2$ detectors. The TAPS detector has been mounted in the forward direction.*

Each BaF$_2$ has a very good time ($\Delta T < 300$ ps) and energy resolution (2.6 % for a photon energy of 400 MeV). Furthermore this crystal offers the interesting feature to present two differents scintillation lights. A fast component ($\tau \approx 0.7$ns) and a slow component ($\tau \approx 620$ns). Since electromagnetic and hadronic particles interact differently with the crystal, their pulse shape response present quite a different lineshape as shown in fig 2.7. The pulse shape for hadrons presents a bigger component with a larger decay time compared to the photon. This feature can be used in principle to separate the two types of particles. In practice the signal is integrated twice once within a short gate (50 ns) and once with a longer gate (2 μs). The application of this feature for a pulse shape analysis will be discussed in a next chapter. Further informations and details about the TAPS detector can be found in ([37]).
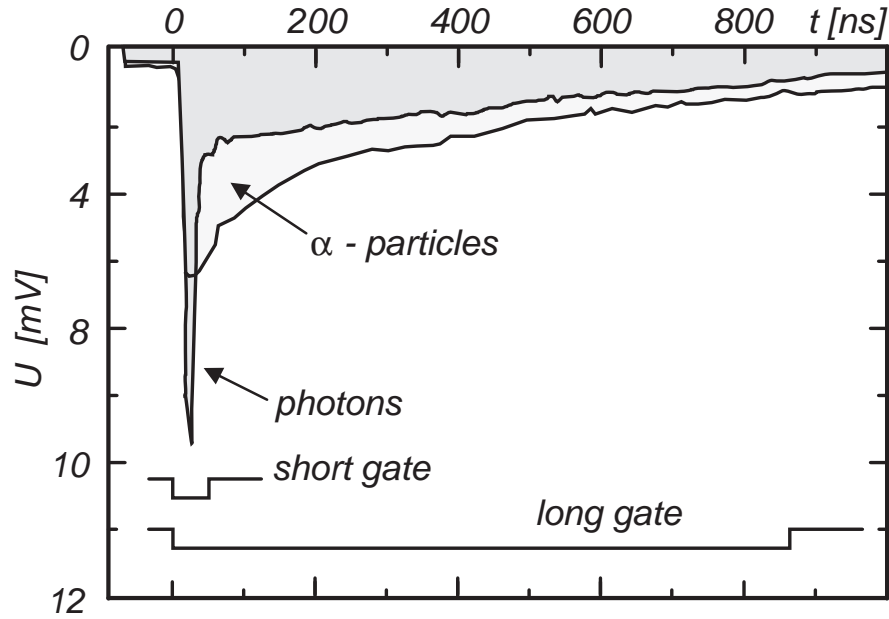
Figure 2.7: *Pulse signal of a BaF$_2$ detector for α and γ particles. The signal is measured with a digital oscilloscop TEKTRONIX 2440. The γ particles are produced with a ^{137}Cs source. The pulse signal of the α particles is drawn in slight grey while the signal for γ is in dark grey. The integration of the pulse signal on both the short and the long gate is used to identifie the particles.*

2.4 The Crystal Barrel

The Crystal barrel detector consists of 1290 CsI crystals mounted in a barrel shape surrounding the target system. Each crystal is 30 cm long corresponding to 16 radiation lenghts with a photodiode mounted on top of it. After amplification, the resulting signal has a rise time around 2 μs, therefore timing information was not available. The crystals have been arranged in 23 rings each containing 60 detectors. The three most backward rings contain only 30 detectors (fig 2.8). The energy resolution is about 2.8 % (at 1 GeV), more details can be found in ([36]).
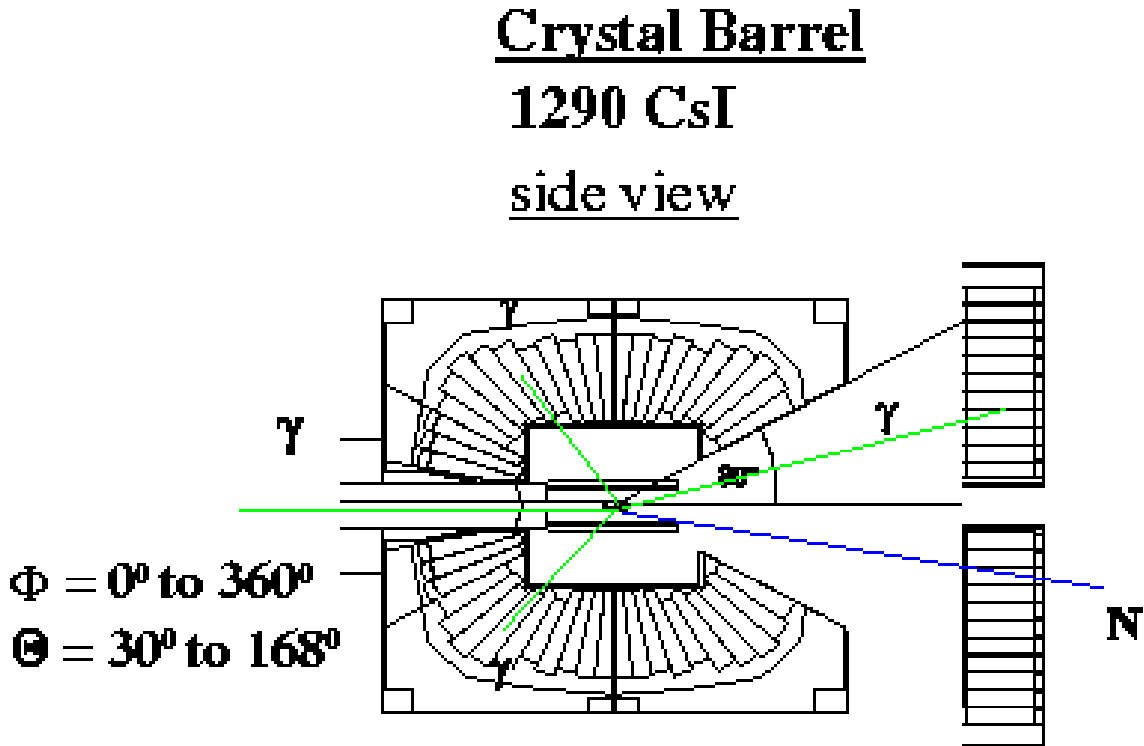
Figure 2.8: *Side view of the Crystal Barrel. Once a nuclear reaction occurs the final state products are detected by the surrounding Crystal Barrel and TAPS detectors.*

2.5 The Inner detector

In the core of the Crytal Barrel a fibre scintillating system was installed to identifie the charged particles. It is a shaped tube covering angles between 28 and 168 degrees. It is made of 3 layers, the outside layer contains 191 fibres orientated parallel to the incoming beam. The middle layer was oriented with +25 degrees compared to the first layer. The inner one was oriented by -25 degrees. The energy deposition was not available in the present experiment, only the time and position of a charged hit was measurable. A sketch of the scintillating fibres is shown next (fig 2.9)

2.6 The solid targets

The different nuclei used for this work are Carbon, Calcium, Niobium and Lead. The target thickness has been chosen such that they present a similar radiation lenght. The main idea is to cover a wide range for the different target masses allowing a significant variation to study any effects depending on the mass. Their main physical properties are summarised in the table 2.1.

400 mm

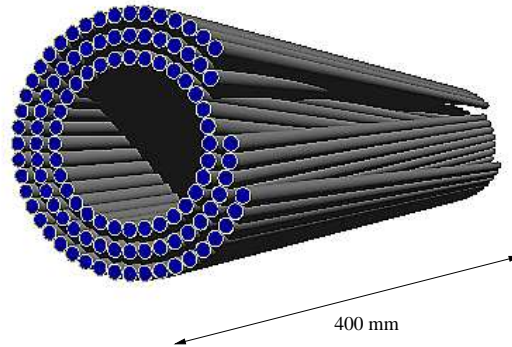Figure 2.9: *Scintillating fibre inner detector used to discriminate the charged particles. The three layers were used to reconstruct the position of the outgoing particle.*

Table 2.1: *Parameters of the nuclear targets.*

Target	Target lenght [cm]	density [g/cm^3]	radiation length % of X_o
^{12}C	2.0	1.67	19.8
^{40}Ca	1.0	1.53	9.08
^{93}Nb	0.1	8.51	17.6
^{nat}Pb	0.06	11.4	8.49

2.7   Data acquisation and data reading

2.7.1   TAPS

The electronic of a single BaF$_2$ detector is shown in (fig 2.10)

The signal coming from the TAPS scintillator is sent through an active splitter giving four outputs. The first one is used to carry the energy signal to the QDC's to be integrated. This signal is delayed to allow trigger formation. It's integrated over through two different gates, one short (50ns) and on long (2μs). This allows to perform pulse shape identification. The second and third outputs are connected to two different LED (Leading Edge Discrimination), the LED High and LED Low which are used for TAPS pre-triggers. The fourth signal from the split is used for timing, gate generation for the QDC's and zero suppression.This signal is passed through a Constant Fraction Discriminator (CFD), which provides a better signal for timing purpose. The output of the CFD is taken out of the experimental area and sent to a daisy chain. The first link is used as the input for the gate generator (RDV), which provides the QDC's with the two gates named before. The second link provides the stop-input for the TDC's which are operated in a common-start mode and were started by the trigger signal. The third and last link is a bit register. This register is monitored by the acquisition and detectors which have a bit set are read out. In other words, only detectors with
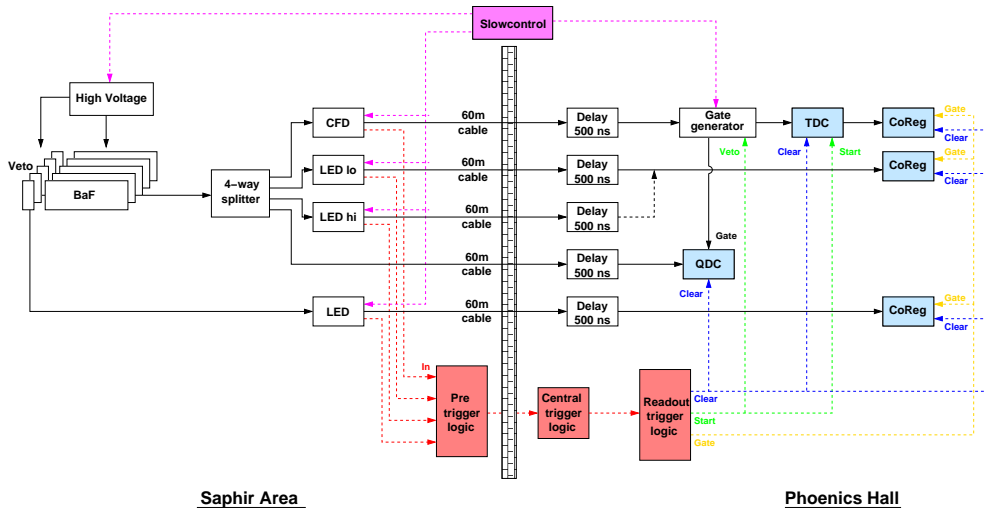
Figure 2.10: *Scheme of the TAPS electronic readout for a single BaF$_2$ detector .*

energy deposition greater than the CFD threshold are read out. The average CFD thresholds of the detectors were set around 10-15 MeV.

2.7.2 Crystal Barrel

The signals coming from the photodiodes are sent to the Charge to Digital Converter (QDC). The total charge is integrated in two energy ranges. The QDC's contain two different capacitors and the incoming signal is plit in a ratio of 1 to 8 between them. The charge to digitize is decided by the internal logic. This system allows the QDC to cover two different ranges, up to 200 MeV and up to 2 GeV. The QDC's are readout by a VMIC computer on a VME compatible board running Linux. Two modules are used, one is responsible for the upstream and the other for the downstream Crystal Barrel half. The two VMIC computers each build their sub events and send this via TCP/IP to a central event builder. More information can be found in [38].

2.7.3 Inner

The signals from the Inner Detector are read out using photo-multipliers.Those are connected to trigger electronics which is able to determine the how many of the three layers detected a hit. This layer multiplicity may be used as a trigger but was not used for this experiment.

2.7.4 Tagger

All the 480 scintillating fibres of the tagger system are connected to CFD's close to the detectors. The resulting logic signals are taken out outside the experimental hall through delay lines and passed through a passive splitter. The signals from the splitter are connected to a multi-hit TDC (64ps/ch) and a scaler. The TDC's (Time to Digital Converter) are used in a common-stop mode. Both TDC's and scalers are mounted

on top of CATCH boards. The CATCH are readout by a VME interface by a similar VMIC eventbuilder as is used for the two Crystal Barrel halves. The signals from the tagger bars (two for each bar, left and right) are fed through delay lines to normal TDC's, QDC's and scalers.

2.7.5   Trigger conditions

Due to a large amount of non interesting events coming from photon-pair conversion and since the electronics is not fast enough to register all produced events some criteria conditions have to be applied concerning the event selection. For that purpose some "trigger conditions " have to be fullfilled. The main trigger used in this experiment consists of two levels. The first level trigger decides whether the event is of interest or not and therefore should be as fast as possible. Why the first-level trigger has to be fast is that a logic decision has to be done before the analog signals reach the readout electronic through appropriate delay lines. The analog signals of the TAPS detector pass through a delay line of 300 ns. Since the Crystal Barrel is equipped with photodiodes the signal rise is too slow (2 μs), therefore the first level trigger has to be made by TAPS which is equiped with fast photomultipliers. Two LED's are connected with two outputs of the splitter and can be used with different thresholds settings. Also designed in term of LED low and LED high those logic signals can be then combined for a more sophisticated event selection. The first pre-trigger is achieved with LED low multiplicity two, that means that at least two hits have to be seen by the TAPS structure in two different logic segments as seen in fig 2.11.
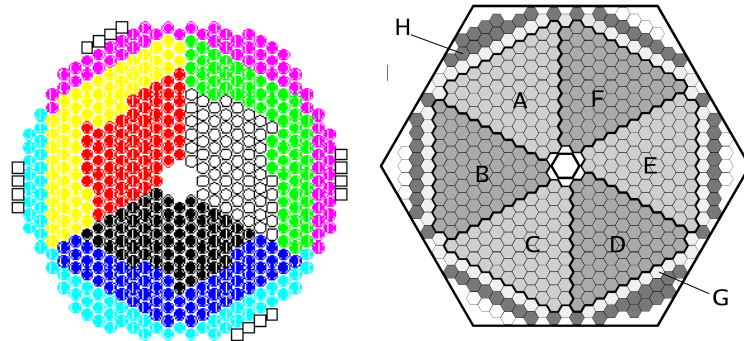
Figure 2.11: *logical segmentation of the led low and high pretrigger. Left: Segmentation of the TAPS detector for the LED low multiplictiy 2 pre-trigger. Right: Segmentation of the TAPS detector for the LED high multiplicity 1 pre-trigger.*

The second pre-trigger is made with the LED low OR (one hit in one segment). This pre-trigger has been downscaled. Finally a third pretrigger is built with LED high multiplicity 1. The TAPS detector is again subdivided in segments but this time following a different layout as seen in fig 2.11. A sketch of the Led Low and High pre-trigger can be seen in fig 2.12 and fig 2.13, respectively.

Figure 2.12: *Sketch of the electronic for the LED low pre-trigger. Each LED module is connected to 16 detectors. In a first step each block of 64 detectors is OR'ed. The eight block outputs are connected to the input of a Memory Lookup Unit (MLU) which is programmed to select multiplicities of two and higher. The resulting sign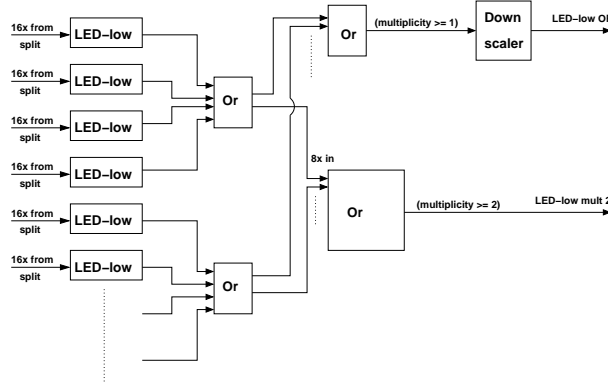al is used as the LED-low mult two pre-trigger. For the minimum bias trigger the eight block outputs are OR'ed together to form an OR of the entire signal. This signal is scaled down and is used as the LED-low OR pre-trigger.*
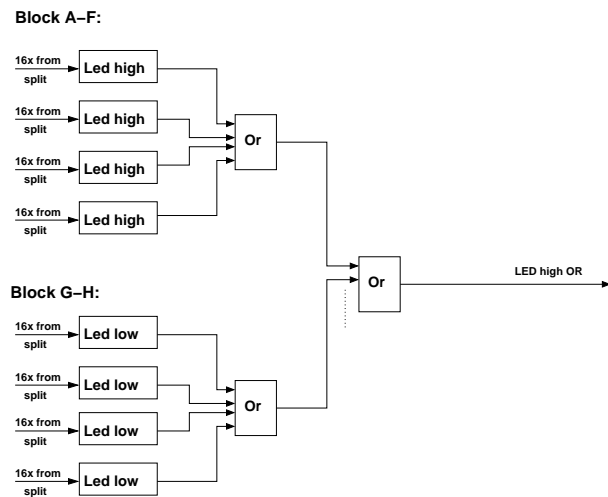
Figure 2.13: *Sketch of the electronic for the LED High (right) pre-triggers. The logic is arranged similar to the logic for the LED-low pre-triggers in 2.12. for this trigger the MLU si programmed to select multiplicities of one and higher.*

The second level trigger determines if the "digitized" signal is good enough to be read out for further processing. Since the digitization process takes about one ms, there is much more time available and the signals coming from the Crystal Barrel can now be associated to the trigger condition. The second-level decision is based on the number of clusters seen by the Crystal Barrel modules. This cluster number is checked out by the so-called FACE (Fast Cluster Ancoding). The clusterisation is done within 10 μs, which is rather slow as compared with the required timescale of the first level trigger.

If the second-level approves the event all measured signals will be digitized, read out and sent to data storage.

Chapter 3

Data Analysis

3.1 Calibration

Informations registered during data taking are not yet directly usable as physical quantities. To analyse reactions as $\gamma + N \rightarrow \eta + X$, the energy, momentum and time of flight of finals states particles as photons, protons have to be extracted from the raw data. The Crystal Barrel and TAPS detectors have been mounted in a combined setup to identify the final state particles. The tagger system is dealing with the timing and energy of the incoming photon that induces the reaction.

3.1.1 Energy calibration

The TAPS and Crystal Barrel detectors have been calibrated separatly.

TAPS

Each individual BaF_2 crytal has to be calibrated separatly. The energy of the incoming particle is converted to an integer value and registered in the QDC modules. Both long and short gates are calibrated and allow for discrimination between electromagnetic and hadronic particles. Before and after each beam time period special runs were dedicated to cosmic radiation measurement. As shown in picture (fig 3.1) two points are of interest, the first non zero value is also called the pedestal value and corresponds to E = 0 MeV. The second one points out the cosmic peak value that according to the detector geometry corresponds to E = 38 MeV. Those two points allow for a first step calibration of the TAPS system, a second calibration procedure is based on the masses of the mesons.

3.1.2 Time Calibration

TAPS time calibration: This part determines the gain of each TAPS TDC. A signal is split into two parts. One is sent to the start of the TDC whereas the second reaches the stop with a certain time delay measured with an oscilloscope.
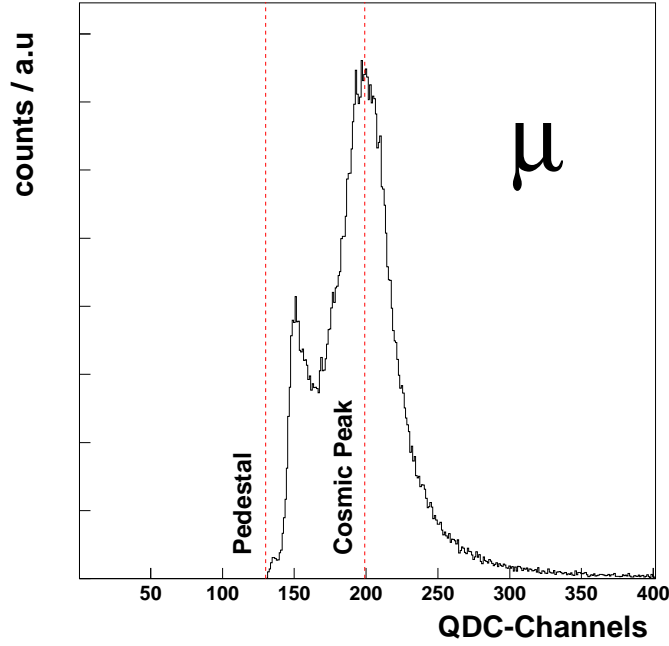
Figure 3.1: *typical energy distribution of cosmic rays in a single BaF2 detector. Both pedestal and cosmic peak are shown*

Tagger time Calibration: The same method is than used.

TAPS-Tagger time calibration: The Trigger start time is given by the TAPS Detector. The time information given by the TAPS or Tagger system contains a time difference between the stop of each crystal and the common start time. Those difference can be expressed as:

t_{TAPS}= individual TAPS - pre-trigger

t_{Tagger} = pretrigger + individual Tagger

Adding those quantities will get rid of the unphysical common trigger time

$$t_{TAPS1-TAPS2} = t_{TAPS1} - t_{TAPS2}$$

$$t_{TAPS-Tagger} = t_{TAPS} - t_{Tagger}$$

In a first step the time of flight difference is computed for each TAPS detector versus all the other TAPS detector and the detectors are calibrated such that in average the time of flight difference is set to 0 ns.

In a second step the time of flight difference between each individual tagger channel is plotted versus all the TAPS detectors. A full width half maximum (FWHM) of 780 ps is achieved when looking at the time difference of two photons in TAPS and a resolution of 2.5 ns on the relative time difference between an electron in the Tagger and a photon in TAPS. The corresponding time of flight differences are plotted next in(fig 3.2).
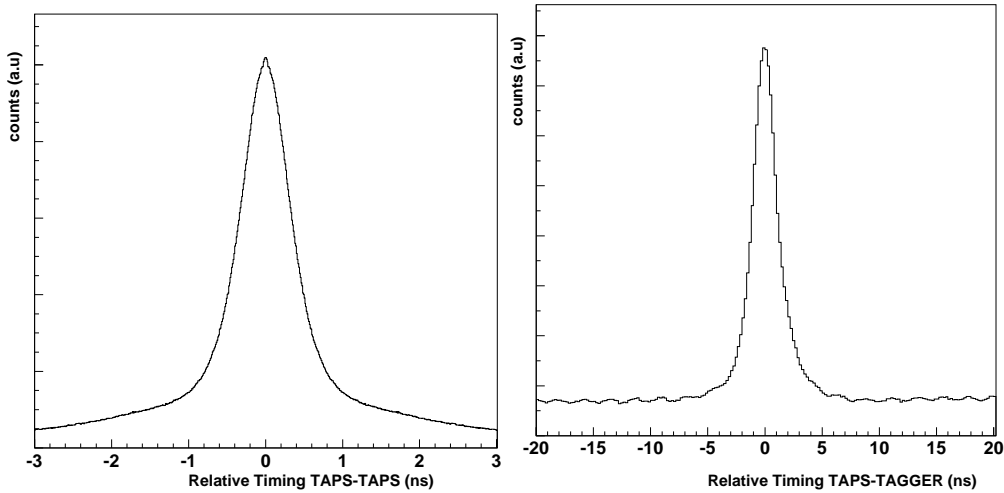
Figure 3.2: *left Relative timing of 2γ in TAPS identified with the VETO detector and the Pulse Shape Analysis, right relative timing TAPS- scifi fibres*

3.2 Identification of the particles

3.2.1 The Veto system

As explained earlier the Veto is used to discriminate between charged and neutral particules. In this thesis work the veto information is used only to reject charged particles when seeking for neutral particles (photons). Since photons may also fire the veto detector and be lost for further analysis, the efficiency of this effect is determined by simulations with Geant 3.21 (see later for description).

3.2.2 The Inner detector

As for the veto detector, the Inner allows to discriminate between charged and neutrals particles and was used to reject charged particles. As for the veto system the loose of photons is taken into account in the simulations.

3.2.3 The pulse shape analysis

The cosmic calibration is applied both for short and long integration gates and will result in a calibration for the wide and narrow energy. The next procedure will lead to so called pulse shape analysis and will use the particularity of the two scintillations lights of the BaF_2 to discriminate between electromagnetic and hadronic particles.

This interesting feature is highlighted in the next pictures of the (fig 3.3). The signal is integrated over the short and long gate and the distribution of the short gate energy is plotted as function of the wide gate energy. The corresponding picture is seen on the left part of fig 3.3. For photons the short and long energies are calibrated in a such way that they are equal. Beside the photon band, another band corresponding

to hadrons (protons,neutrons) is visible. The same events can also be visualised using polar coordinates as seen in the right plot of the fig 3.3.
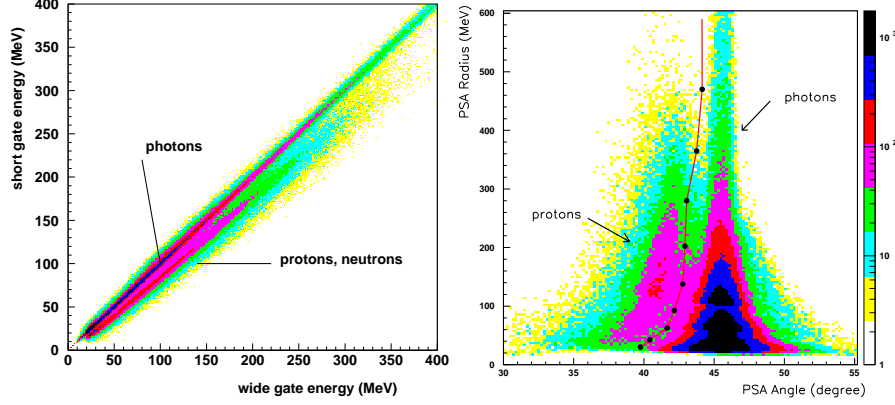

Figure 3.3: *Left Plot: Short gate energy vs. long gate energy. Right Plot: Typical pulseshape plot for a BaF_2 in polar coordinates. Photons are defined being to the right of the cut line*

The link between the polar coordinates and the measured energies is defined as follows:

$$R = \sqrt{E_s^2 + E_w^2} \qquad (3.1)$$

$$tan(\phi) = (E_s/E_w) \qquad (3.2)$$

where E_s defines the short gate energy and E_w the wide gate energy. The cuts used for discrimination are determined by analysing different projections on the x-axis for different ranges over the y-axis. The photon peak is assumed now to be right at a position of 45 degrees as shown in plot (fig 3.4). A gaussian fits the photon peak and a 3σ cut to the left of the photon peak will define the limit between photons and hadrons. More details concerning this method can be found in the PhD thesis of Martin Kotulla [41].

The detectors are calibrated now according to the average deposited energy of the cosmics rays. The determination of the 2-photon invariant masses is used for the next step of the energy calibration and is achieved offline for the different data samples. The energy of the differents photons coming from the meson decays is collected by the different detectors. A combination of the reconstructed angle/energy of the particles is done in terms of an invariant mass analysis.

3.2.4   Invariant Mass Analysis

The invariant mass of two photons is calculated as follows:

$$M_{inv} = \sqrt{P^2} = \sqrt{(P_1 + P_2)^2} = \sqrt{P_1^2 + P_2^2 + 2P_1P_2} \qquad (3.3)$$

P_1 and P_2 are the four-vectors of photons, $P_1^2 = P_2^2 = M_\gamma^2 = 0$.
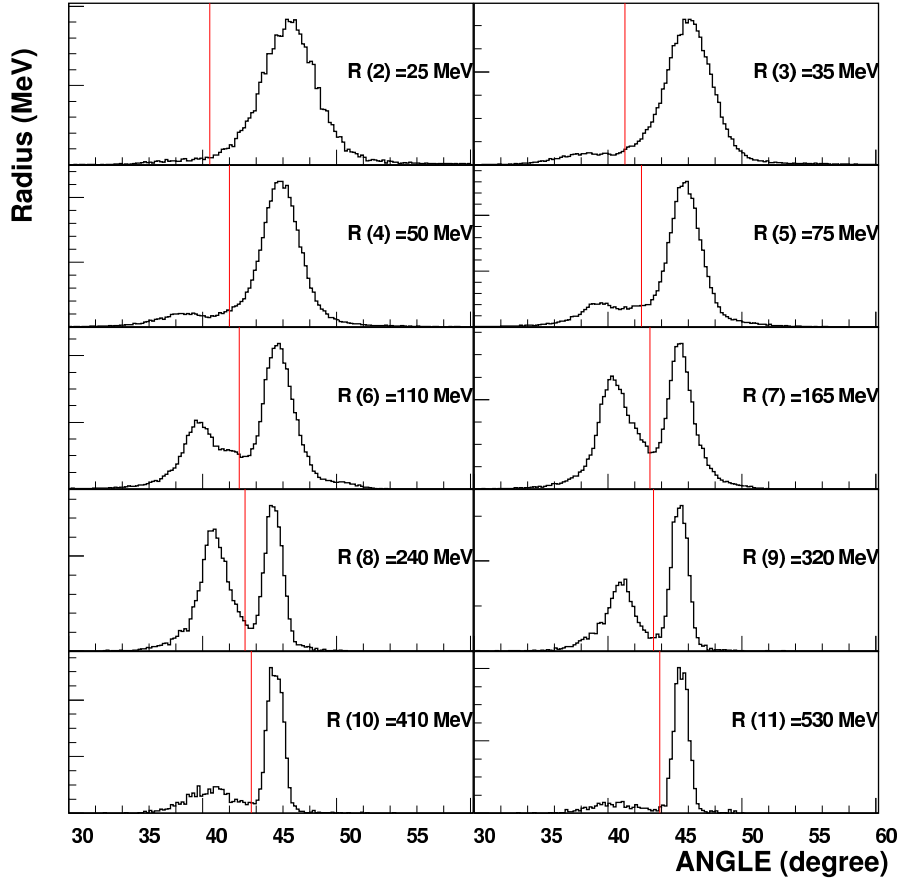The invariant mass picture of two photons exhibits two peaks corresponding to the

Figure 3.4: *projections over the x-axis for different range values of the y-axis.*

production of two different mesons, the π^0 at 135 MeV and the η at 547 MeV. With the cosmic calibration the two peaks are not at the exact position, therefore some corrections have to be applied. In any rigour all combinations between the 528 BaF$_2$ detectors should be done but this would lead to a number of combination of 278784. The chosen method is then to combine each of the 528 detectors with all others and determine an average value of the correction to apply to this particular detector such that the peak position fits with the π^0 mass.

3.2.5 Energy correction

Once fitting the π^0 invariant mass the η peak position seems to be slightly shifted towards higher invariant masses. In order to compensate this effect an energy dependent correction should be applied on the photon energy introducing two additionnal parameters such that the corrected photon energy becomes

$$E_\gamma = a * E_\gamma + b * E_\gamma^2$$

The values of the fitted parameters are a = 1.01204 b = 0.0000353
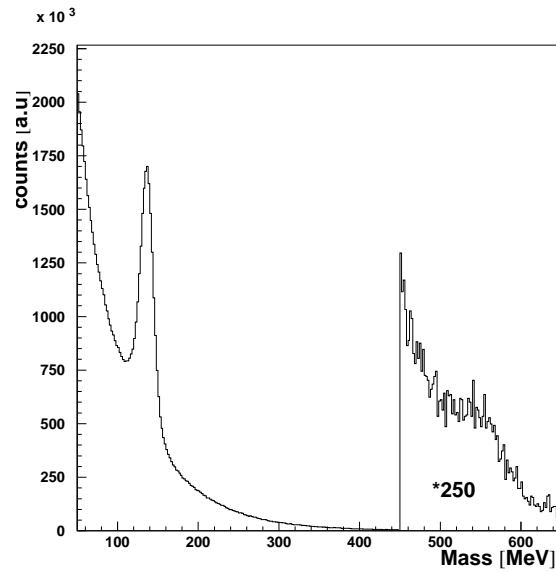
TAPS

Figure 3.5: *Invariant mass of photons pairs. The peak at 135 MeV corresponds to π^0 events and the second one at 547.3 to the η meson*
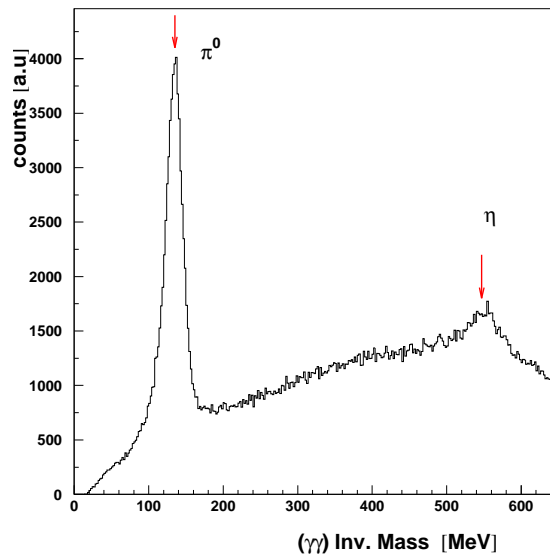
Crystal Barrel

Figure 3.6: *Invariant mass of photons pairs for the Barrel Detector. Both π^0 and η peak are shown for the condition that the sum of both photon energies is at least greater than 800 MeV.*

3.2.6 LED Thresholds Calibration

As mentioned in an earlier chapter the information contained in the LED pattern is used to decide if an event is going to be recorded or not. Simulations on certain event types have been performed in order to determine raisonable LED thresholds. Compromises about those values have to be done. Too low thresholds would lead to an increase of the dead time and background but if those are too high, good events would be lost due to kinematical limits. Furthermore the knowledge of the values of the thresholds is mandatory to get physical cross section. The save values have to be implemented in the simulation software. The determination of these parameters is done by comparing the energy distribution in the detectors with and without the condition that a LED bit pattern has been recorded.
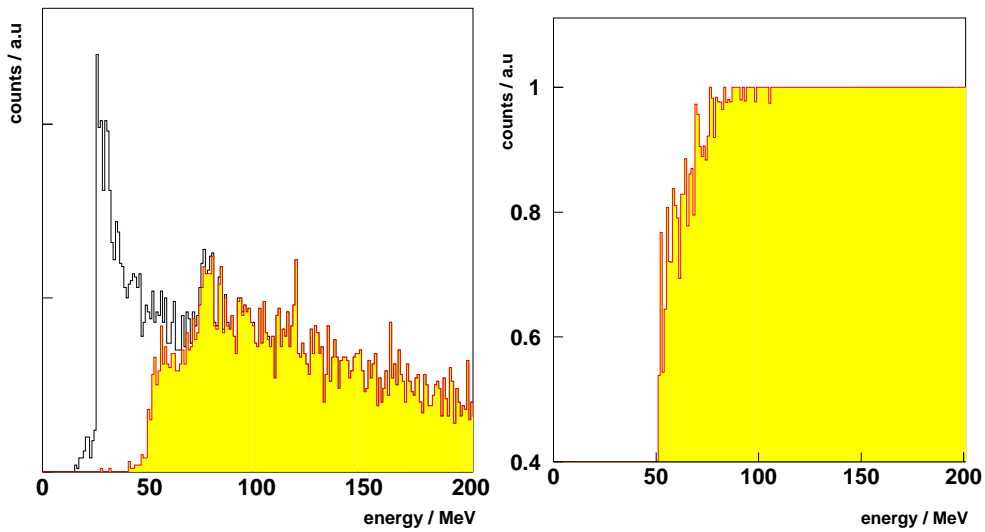
Figure 3.7: *left picture: Energy distribution for one single detector when the LED bit pattern is required (grey shaded area) or not (solid line) right : Ratio of both distribution*

Two comments should be made at this point, the first concerns the shape of the rising edge of the ratio shown in the right part of the fig 3.7. As the ratio of both energy distributions is not showing a sharp rise from 0 to 1 the software trigger installed in the simulation should not undershot the values of the hardware trigger. To cure this effect more restrictive conditions on the threshold values are applied. Furthermore the software analysis used for both data and simulation only considers photons for the trigger whereas the hardware system is not able to disentangle the kind of particles that triggered. The main reason is that protons and neutrons do interact differently with the nuclear matter such that the comparison between the different nuclear target may be unfair. This is the case for the comparison between the carbon or calcium nucleus with lead which contains a relatively higher number of neutrons. Therefore these thresholds correspond only to photons since protons and neutrons have different responses. To eliminate all systematical effects only trigger from photons are accepted.

3.3   Identification of the $\pi^0\pi^0$ channel

The identification of this channel requires that at least four particles identified as photons have been detected by the combined TAPS and Crystal Barrel setup. Each combination of four photons is studied and the masses of the photon pairs are calculated. As a first condition the two pion invariant masses are required to lie between 110 and 160 MeV. If several combinations of the four photons fullfill the previous condition then the best combination is chosen according to minimisation of the quantity

$$\chi^2 = \sqrt{(M_{\gamma_1\gamma_2} - 135)^2 + (M_{\gamma_3\gamma_4} - 135)^2} \qquad (3.4)$$

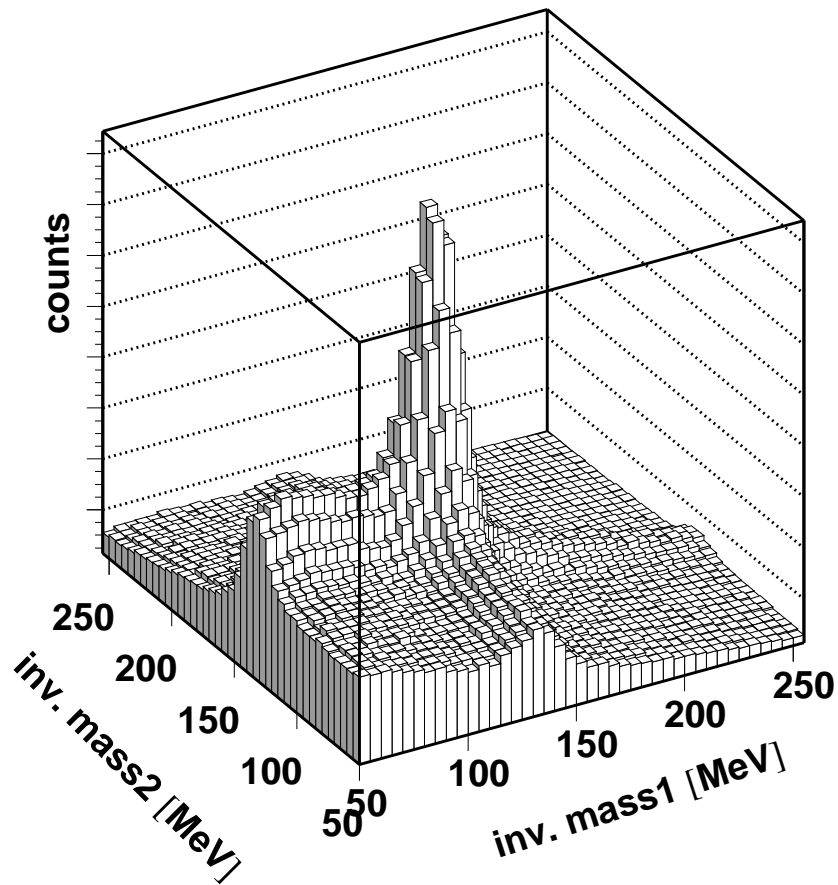The best combination is plotted in the following plot in (fig 3.8).

Figure 3.8: *invariant mass of photons pair 1 versus invariant mass of photons pair 2 when four gammas are detected*

Missing mass principle

The energy and momentum of both pions are detected and reconstructed from the detector system. The incident photon beam energy is also known from the tagger. The reaction is assumed to take place on a single nucleon (either proton or neutron) in a quasifree mode so that the constraints on energy and momentum conservation can be written as :

$$M_X = \sqrt{(E_\gamma + M_N + E_\eta)^2 - (\vec{P}_{beam} - \vec{P}_\eta)^2} \tag{3.5}$$

$$\Delta M = M_X - M_N \tag{3.6}$$

The simulation is done with Geant3 (see later chapter for more explanations). Two π^0 are generated inside the nucleus. The π^0 can get absorbed by a nucleon and be re-emitted according to energy-momentum conservation. They finally decay into 4γ and get detected. Different backgrounds like decays of the η meson into $3\ \pi^0$ may enter in the missing mass of the double π^0 if the $2\ \gamma$ coming from the decay of the third π^0 are not detected by the detector system. The next distribution shows a comparison between the simulation and the data for two different photon energy ranges.
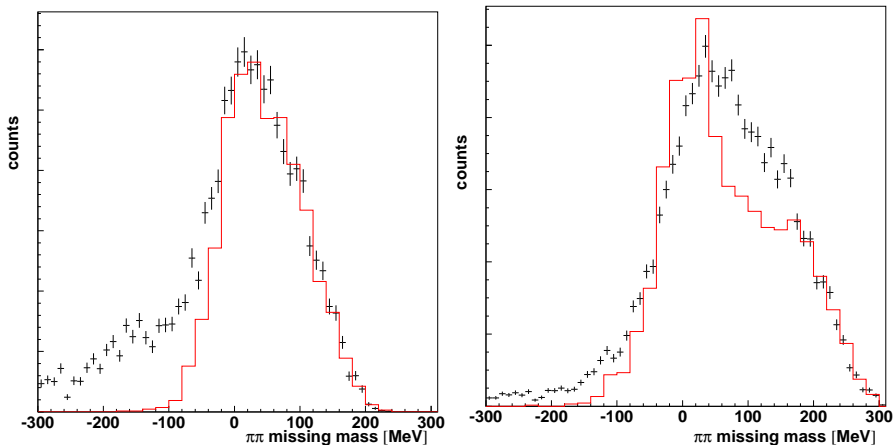
Figure 3.9: *Comparison missing mass data with simulation, left picture for $E_\gamma = 500,650$ MeV. Right plot $E_\gamma = 650,800$ MeV*

The left plot at low energy shows a fair agreement between data and simulation, the missing mass at higher energies turns out to be more difficult to reproduce. The simulation lineshape in the energy range (650,800) MeV shows two parts. One part with a peak structure around a missing mass of 0 MeV and a broader structure centered around 150 MeV corresponding to events with rescattered pions. The discrepancy between the two missing mass lineshapes could be explained by background sources to the double π^0 reaction as mentioned earlier. A tight cut has been done in the missing mass selection between -50 and 30 MeV such that the background contribution is minimised. The η meson into its three π^0 decay channel may contribute but probably other reaction channels do also contribute. Since the η cross section off Calcium has been measured in this energy range the number of events where two of the three π^0

coming from the η decay are detected can be calculated. This number turns out to be rather small in the selected missing mass range, less than one % for a photon energy of 800 MeV.

The fig 3.10 shows the missing mass distribution when two π^0 are detected for simulated η's into the three π^0 decay channel. The range of the photon beam energy lies between 800 and 1300 MeV.
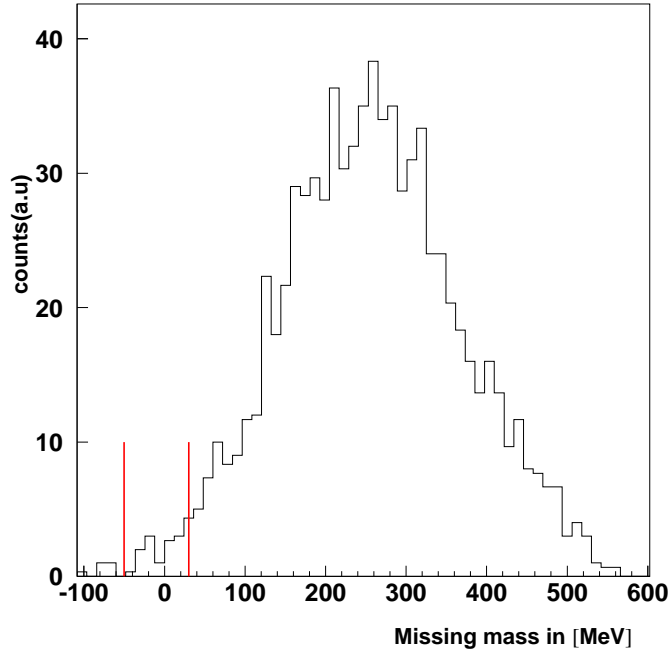
Figure 3.10: *Missing mass distribution of two detected π^0 when an η decaying into three π^0 is simulated by GEANT. The photon beam energy range lyes between 800 and 1300 MeV.*

The two lines at -50 and 30 MeV indicate the cuts applied in the analysis to identify the two π^0 events. Only few events are entering into this rangem, this feature indicates that the background coming from the η channel into its three π^0 decay channel plays a minor role in this energy range.

3.3.1 Identification of the correlated charged nucleon

For the reaction channel $\gamma + N \to \pi^0\pi^0 + N$, the correlated nucleon is not explicitely required in the reconstruction analysis. Either a proton or a neutron can be produced. The probability to detect the two π^0 with a further proton is rather high due to the large solid coverage provided by the combined TAPS/Crystal Barrel setup. Thus events with a charged particle may also be taken into account if the particle is detected by the TAPS detector in certain kinematical conditions.

The relative time of flight of the correlated particle detected by TAPS is plotted as function of its deposited energy in (fig3.11) if the following conditions are fullfilled.

The first condition requires events with four photons and two identified pions.

For the second condition, a hit in the veto corresponding to the detector where the maximum energy is deposited or in the veto of a neighbour detector is demanded.

The visible and so-called "banana" region corresponds to protons. In this kinematical region protons deposit their full kinetic energy in the detector. A maximum deposited energy of 400 MeV is observed for a time of flight around two ns, faster protons will punch through. Another band corresponding to the photons can be seen around 0 ns independant of the deposited energy. The trace of the charged pions π^+, π^- get mixed with the very fast protons. (accumulation trace for a time of flight around 0 ns and a deposited energy of 180 MeV).
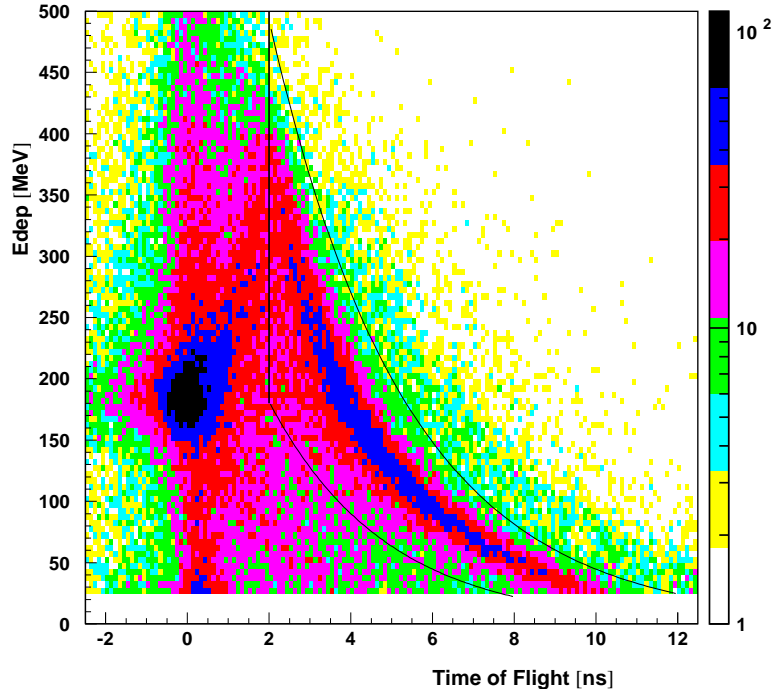

Figure 3.11: *relative time of flight of a proton as function of its deposited energy measured in the TAPS detector*

Some kinematical limits have been drawn in this plot surrounding the "banana" trace. A proton detected in this kinematical region is allowed and the event is counted otherwise it is rejected. This cut removes background coming from charged π but may remove good events with badly identified protons.

Events with a charged hit in the Crystal Barrel are not used.

With the Crystal Barrel the available tool to identify the charged particles is based on the angle difference between a hit in the Barrel detector and a hit in the scintillating fibres.. On a proton target the phi difference between the coincident two π^0 and the proton should be equal to π. For a nuclear target this method is not selective enough to clearly identify coincident protons and too much background events would enter in the selection. Indeed, in-medium effects like Fermi smearing or rescattering processes induces a much broader phi difference distribution. Furthermore, events with a coincident neutron are also not used for a study on nuclear targets. The aim is also to limitate events coming from background reaction.

The previous conditions tell that a certain amount of double π^0 events will not be taken into account. Therefore some comments should be done in order to get an estimate of the lost events.

At the reaction threshold of the two π^0 most of the protons are emitted forward and detected by the TAPS detector.

For higher photon beam energies the proton can punch through and will not be measured due to the kinematical constraints applied in the analysis. The polar angle of the emitted proton arises with the photon beam energy such that a fraction of the protons are emitted towards the crytal Barrel. Therefore the number of lost events will increase with the incident photon energy.

Events may also be lost due to the fact that events with neutron are not considered. At low photon energy most of the neutrons are emitted in the forward region towards the TAPS detector.

The neutron efficiency for TAPS has been estimated in the average range of 10 to 15 % using the GEANT3 package for kinetic energies less than 300 MeV in the PhD thesis of [45]. The loose effect is also energy dependent such that for incident photon energies less than 1 GeV an upper value of 20 % event lost is assumed.

3.4 Identification of the η meson channel

The η meson has been identified via its three π^0 decay channel with six photons as final state particles. During the experiment events have been registered without any conditions on the type of particle which induces the trigger such that proton or neutron can contribute. A software trigger condition has been applied during the offline analysis such that only events where the trigger is done by photons are taken into account. One reason is that the coincident proton or neutron may strongly interact with the nuclear matter so that quite elaborated models would be needed for the simulations. Furthermore the trigger probability for neutrons is completely different from protons. Thus, the trigger system is entirely based on the detection of the photons. One of the photon has to be at least detected by TAPS with the LED high pre-trigger condition. The probability for a photon to be seen in TAPS drops very fast as the η meson is emitted in the backward region of the beam direction. The detection efficiency covers a wider kinematical range in the case of an η decaying into three π^0 compared with the situation where an η decays into two γ. As seen in the following plot fig 3.12, a cut on the π^0 invariant mass between 110 and 160 MeV was made and the combination of the three π^0 which minimize the following expression is taken into account.

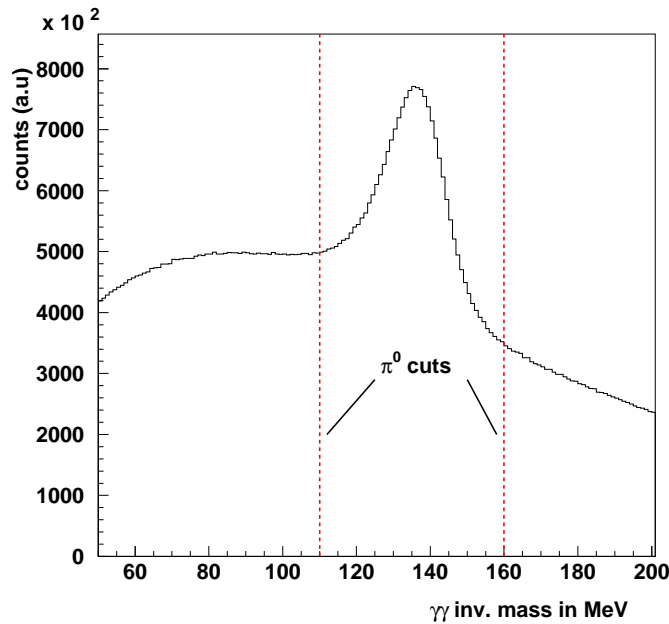$$\chi^2 = \sum_i \frac{(135 - m_{\pi^0})^2}{(\Delta m)^2}$$

Figure 3.12: *Invariant mass of two photons when six photons are detected with the combined TAPS and Crystal Barrel setup. The two lines at 110 and 160 MeV represent the cuts applied to select the π^0.*

The η signal appears as a resonance of the combination of three π^0. The extraction of the signal from the background is made using a fit based on the simulated lineshape. The invariant mass distributions are shown for two differents photon beam ranges in fig3.13.
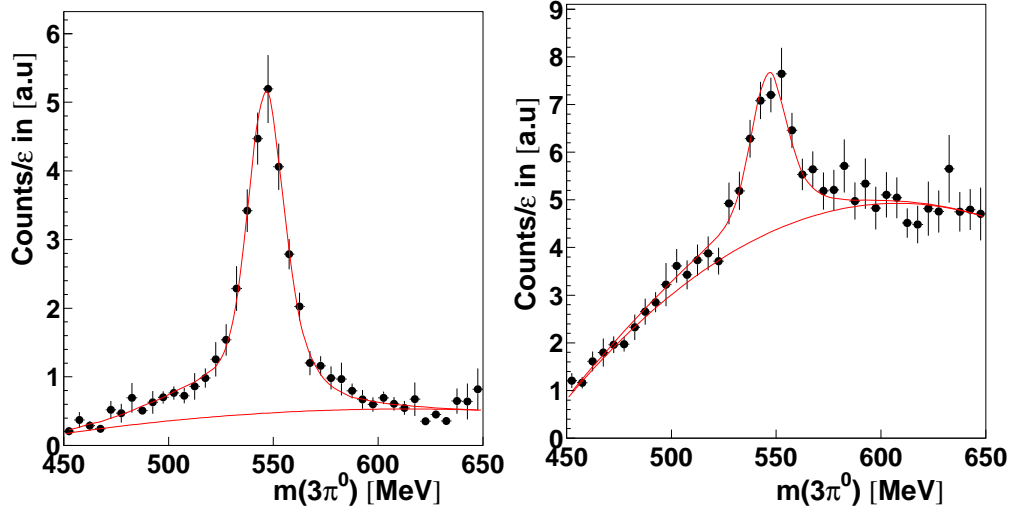
Figure 3.13: *Comparison of the three π^0 invariant mass for two incident photon beam energy ranges. Left: Range in MeV (800,850). Right: Range in MeV (1850,2150)*

The background was fitted by a second order polynomial and the resulting signal is shown in (fig 3.14).

Figure 3.14: *Comparison of the background substracted signal to the simulated lineshape for the $3\pi^0$ invariant mass. Range in MeV Left: (800,850) Right: (1850,2150). A ligne is plotted at the position of the η mass.*

3.4.1 Missing Mass Analysis

In order to analyse quasifree η photoproduction a missing mass analysis on the nucleon can be done to identify the single η production. At the reaction threshold, the η can only be produced direct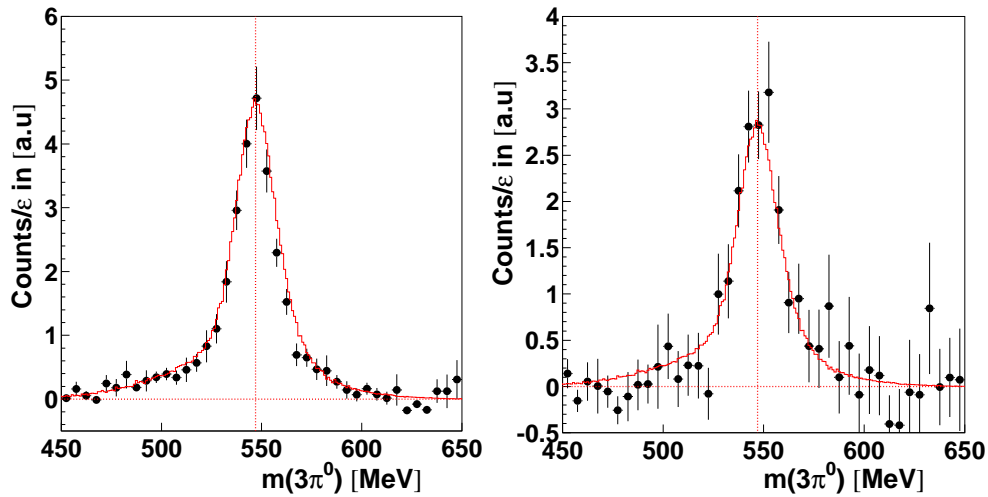ly with a correlated nucleon, therefore a distribution centered at the nucleon mass position is expected. On the next plot fig 3.15 the missing mass distributions are compared for two photon beam energy ranges.
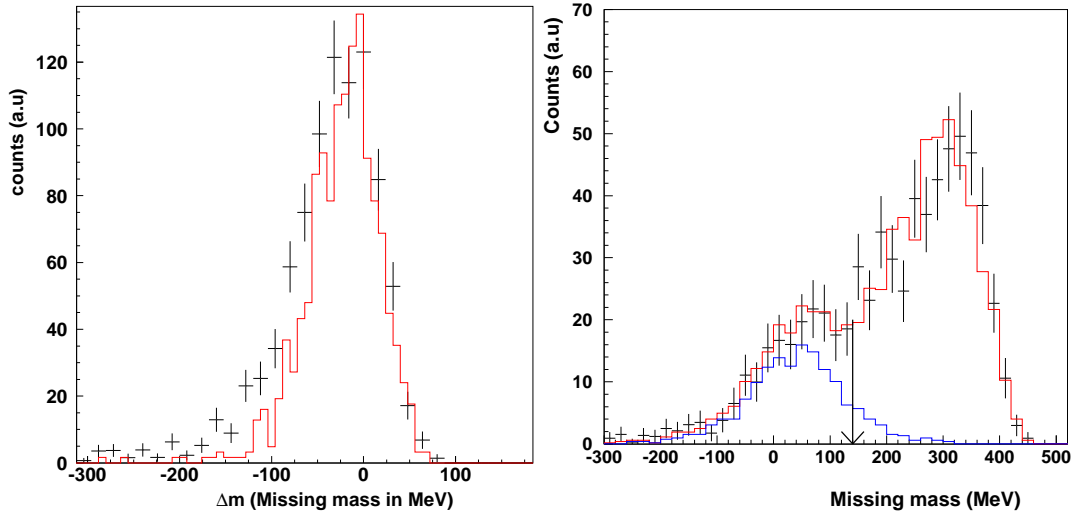

Figure 3.15: *Left plot : Missing mass on nucleon for photon range E_γ between 650 and 800 MeV. Data are the cross points, the full line is the simulated lineshape. Right plot: Missing mass on nucleon for photon range E_γ between 1300 and 1500 MeV. The data are also represented as cross points while the full line represent the simulation. A line at 140 MeV is drawn to show the limit of the missing mass cut for the cross section measurement.*

The comparison between data and simulation gives quite good agreement and indicates that the physic process are quite well understood at the η threshold. The simulation is based on BUU calculations from [56] and takes into account the relative proportion of the different production modes of the η meson. Thus this model includes η coming from the decay of the $S_{11}(1535)$, Born terms, and background to the single η production as the production of coincident $\eta\pi$ or secondary η's where a primary π scatter on a nucleon to produce a further η. See later chapter for more details on the BUU simulations. At higher energies, η mesons may be created via different reaction mechanisms and the interpretation of the missing mass spectra is getting more difficult.

The plot at the right hand side of the fig 3.15 corresponds to photon energies between 1.3 and 1.5 GeV. The distinction between the quasifree process and the background reaction is possible at this energy range since enough energy is available to move the background distribution far enough from the quasifree peak.

Data points and simulation agree quite well at this energy scale, the bump like structure corresponding to the quasifree events around 0 MeV and the background lineshape match pretty good. The contribution of the quasifree events at this energy scale has been predicted by BUU calculations and the lineshape representing the quasifree events is drawn centered around 0 MeV of the missing mass axes. Nevertheless, the experimental determination of the quasifree events should be independant from model. In that sense a cut in the missing mass range at 140 MeV has been applied for of the determination of the quasifree signal. The effect of this cut will be shown in the next chapter concerning the extraction of the cross sections.

Chapter 4

Determination of the cross section

4.1   cross section formula

The total cross section is experimentaly determined by

$$\sigma_{tot}(E_\gamma) = \frac{N_{event}(E_\gamma)}{\varepsilon_{detectors}(E_\gamma) \cdot \Gamma_{br} \cdot N_{target} \cdot N_\gamma(E_\gamma)} \tag{4.1}$$

whith :

- $N_{event}(E_\gamma)$ Number of reconstructed events for the channel of interest

- $\varepsilon_{detectors}(E_\gamma)$ Detection efficiency from simulations for the corresponding channel

- Γ_{br} is the branching ratio of the measured channel.

- $N_\gamma(E_\gamma)$ is the number of photons that reach the target

- N_{target} is the number of nuclei targets per cm^2 (or barn).

$$N_{target} = \frac{\mathcal{N}_A \cdot \rho_{nucleus} \cdot L_{target}}{M_{nucleus}} \tag{4.2}$$

with $\mathcal{N}_A$ the Avogadro number, $\rho_{nucleus}$ the target density, L_{target} the target thickness and $M_{nucleus}$ the molar mass of the nucleus.

4.2 Simulation of the detector system

The detector system has been simulated to estimate the probability to reconstruct an event produced in the target. The so-called detection efficiency can be limited by different reasons. Although an almost 4π solid angle coverage is provided by the combined TAPS/Crystal Barrel setup, one or several photon may not be detected. A minimum size of the signals is required by the CFD or LED modules. Some trigger conditions had to be applied in order to reduce the number of useless events and keep a reasonnable dead time of the detector system. A non negligeable amount of good data was then rejected and efficiency corrections have to be done to compensate this effect. The GEANT3 package has been used to model the detection efficiency ([52]) The configuration of the detector system has been implemented and a sketch of the setup is shown in fig 4.1.
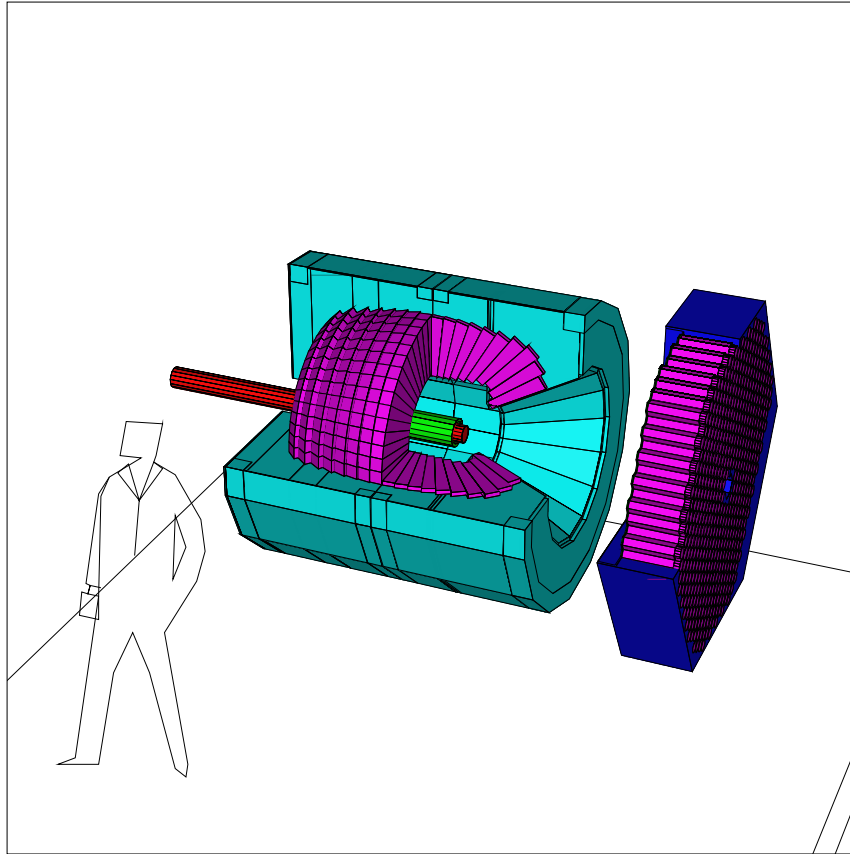

Figure 4.1: *Sketch of the implemented setup geometry into the GEANT simulation. In this picture the crystal Barrel and the TAPS detectors have been made visible. In the center of the Crystal Barrel the Inner detector is shown around the beam pipe.*

4.2.1 Determination of the η efficiency

The mechanism leading to the η meson production during the reaction $\gamma + N \to \eta + N$ in the nuclear target is unknown. The η meson undergo strong final state interactions and at high photon energies may be produced during secondary reactions. Therefore simulations taking only into account Fermi smearing would be unrealistic. An alternative is used with the so-called grid efficiency method where the η efficiency is determined in the laboratory frame as function of its measured polar angle θ_η and its measured kinetic energy T_η. Both quantities are used as degrees of freedom. The efficiency to detect η mesons has been determined for the decay channel $\eta \to 3\pi^0 \to 6\gamma$. The η particles are randomly generated in the target system and decay into the six photon final state particles. The absorption of the photons within the target is therefore taken into account. The six photons are reconstructed and the best three π^0 combination is determined to get the energy and momentum of the formed η. In the simulation both the kinetic energy and the polar angle are isotropicaly chosen and define the so-calleds start distribution $N_{gene\eta}(T_\eta, \theta_\eta)$. This distribution countains the number of emitted η per intervall $T_\eta - \theta_\eta$. Another distribution $N_{built\eta}(T_\eta, \theta_\eta)$ contains the number of reconstructed η assuming the differents conditions (invariant mass cuts, trigger conditions, etc...) per intervall $T_\eta - \theta_\eta$.

The resulting efficiency ϵ is determined dividing both quantities :

$$\epsilon(T_\eta, \theta_\eta) = \frac{N_{built\eta}(T_\eta, \theta_\eta)}{N_{gene\eta}(T_\eta, \theta_\eta)} \tag{4.3}$$
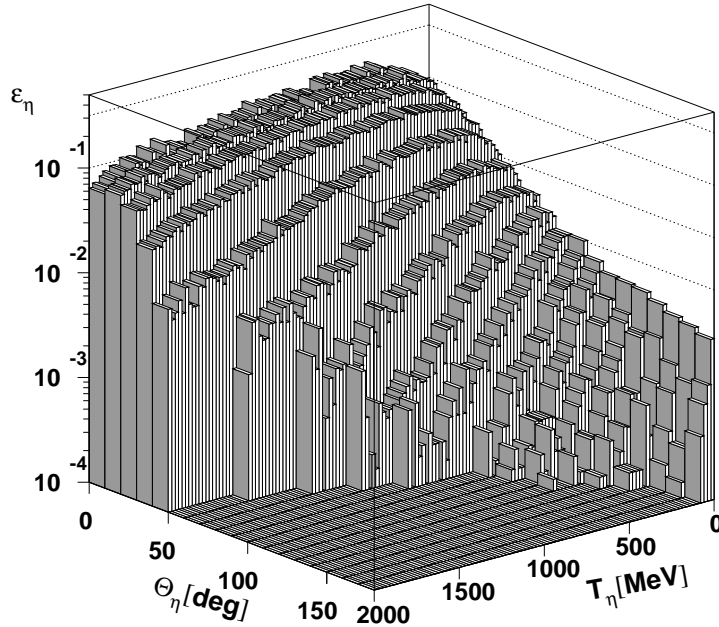

Figure 4.2: *η detection efficiency as function of its kinetic energy and theta angle in the lab frame*

4.2.2   Efficiency for the $\pi^0\pi^0$ channel

The efficiency for the reaction $\gamma + N \rightarrow \pi^0\pi^0 + N$ has been determined as function of the incident photon beam energy. The mean free path of the π^0 is known for relatively small values of the kinetic energy. Simple arguments have been considered to take into account the multiple rescattering of the produced meson within the nucleus. A π^0 may propagate inside the nucleus and if an interaction with a nucleon occurs the energy of both particles is calculated in the center of mass system. A further π^0 is created with a new four-momentum determined by the monte-carlo routine. Uncertainties have to be taken into account. A more sophisticated simulation would include (for example) charged exchange currents, propagation of resonances, and Pauli-Blocking. Nethertheless, the idea is to stay as far as possible off modele dependence, therefore a compromise is required.

The picture in fig 4.3 shows the $\pi^0\pi^0$ efficiency determined from Geant3 as function of incident photon energy. The different cuts applied in the analysis, like cuts on the π^0 invariant mass or missing mass cuts are reproduced in the same way in the simulations.
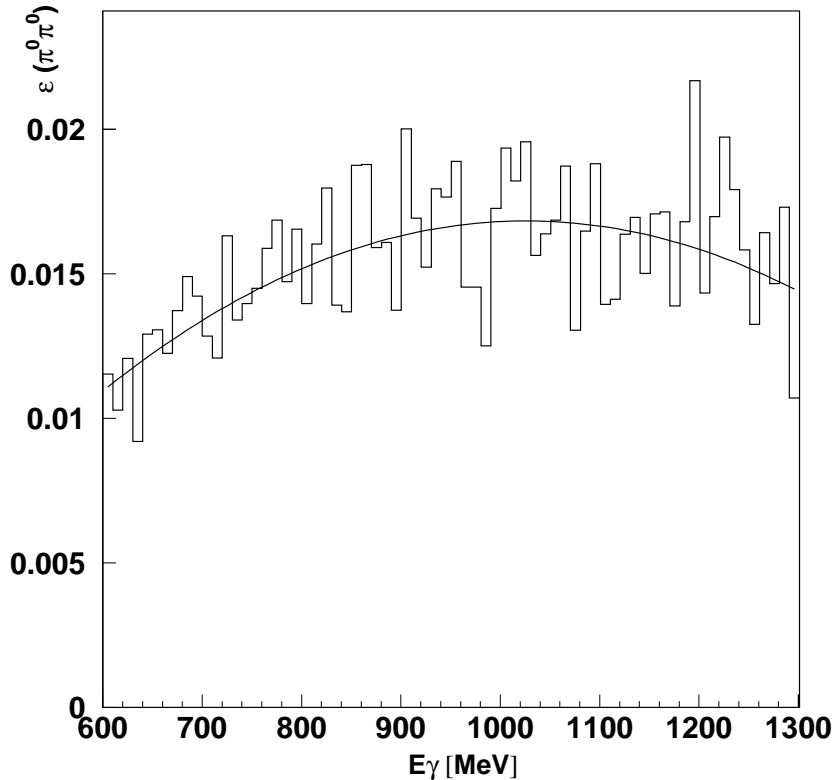

Figure 4.3: *Double π^0 efficiency as function of the incident photon beam energy. The full line is polynomial function of degree two which fits the simulation points. This function is used further to measure the cross sections.*

4.3 Random correction

The number of electrons detected by the tagging system is in average greater than 15 and can be seen on the picture (fig 4.4). This high multiplicity is explained by the high beam intensity and the rescattering of the primary electrons in the beam dump that fly back to the tagger system.
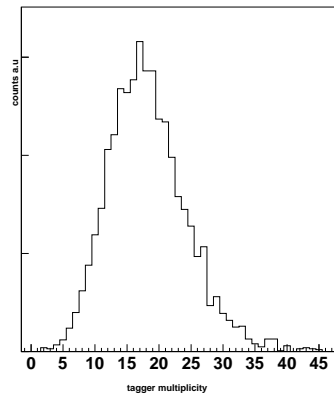

Figure 4.4: *Tagger multiplicity or number of electrons detected by the tagger fibres in a time range of 400ns.*

The relative timing TAPS-tagger as drawn in (fig 4.5) highlighs different zones of the timing range.
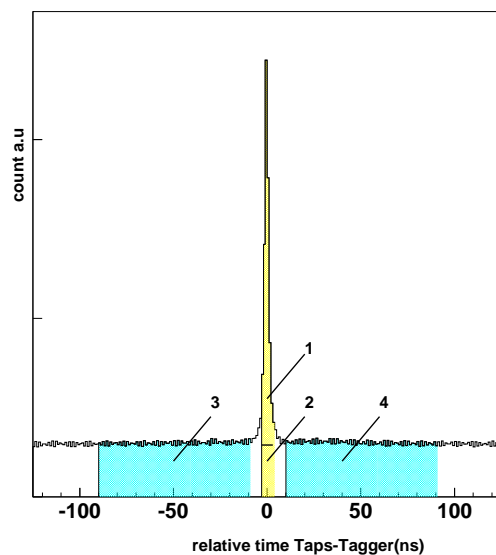

Figure 4.5: *Time difference between an electron hit in the tagger and a photon detected in TAPS*

The time distribution shows a peak structure around 0 ns and a smooth and flat background. Events in the region of the prompt peak correspond to the true coincident events when electrons and photons are detected in coincidence (area 1) and to accidental coincidences (area 2). The ranges besides the prompt peak (3 and 4) contain only random background. A time coincidence cut around the prompt peak allows to reject most of background events that belong to the "plateau"'. Nevertheless, the accidental coincidence can not be completely removed in this way, therefore a background substraction must be applied to get correct distributions. This solution is possible due to the nature of the background which presents the same amount of events at any time position of the plateau. The number of background events to be substracted is determined from an event selection made in the region 3 and 4. Events with a time difference between -90 and -10 ns OR 10ns and 90 ns are selected and this quantity will be substracted from the coincident events of the time region between -3 and 3 ns. A weight factor of 0.033 has to applied to the background events to normalize the areas: This number is determined in the following way : $\frac{(3-(-3))}{(-10-(-90)+(90-10))} = 0.033$ The effect of the random correction is visible in the missing mass spectra in fig 4.6.
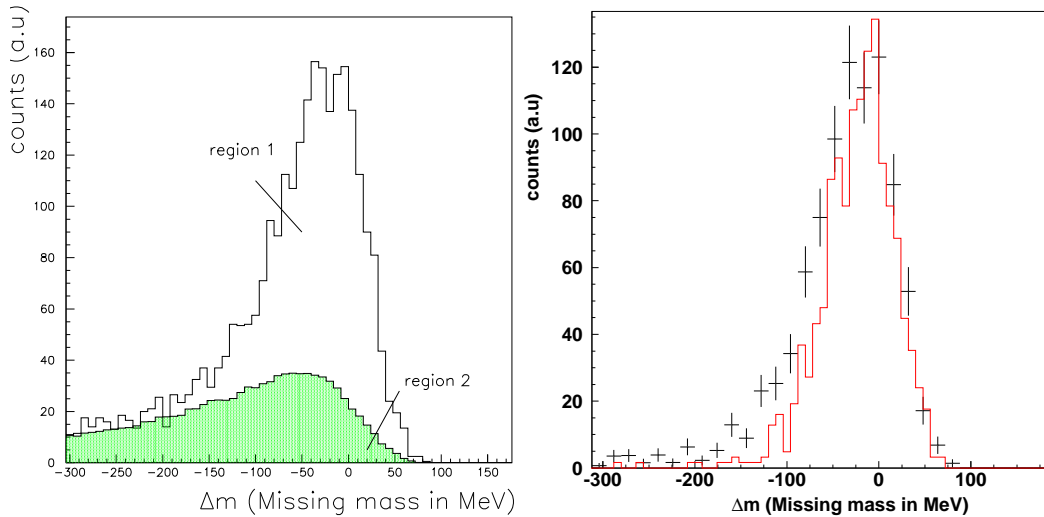
Figure 4.6: *Left plot : Missing mass on nucleon for photon range E_γ between 650 and 800 MeV. The region one represents the events, the full shaded area, region two describes background events coming from accidental coincidence. Those events have to be substracted. Right plot: Comparison of the substracted coincidental background missing mass(dotted points) with a simulation lineshape from Pascal Muehlich (full line, see later chapter for more description about the BUU simulations)*

The efficiency of this method is checked when the background free missing mass spectrum is compared with the simulation where this kind of background does not exist.

4.4 Photon Flux normalization

The number of events deduced from the invariant mass picture is a statistical quantity and gives the rate of the reaction of interest. To get a normalized value independant of the number of photons that have reached the target and induce a reaction the event rate has to be normalized by the number of photons that have reached the target. The number of photons is determined by

$$N_\gamma(E_\gamma) = N_{scalers}(E_\gamma) \times \epsilon_{tagg}$$

where $N_{scalers}$ is the number of electrons counted by the scalers and ϵ_{tagg} is the probability for a photon to reach the target.

4.4.1 Electron scalers

some electronic modules (scalers) have been installed to count the number of detected electrons in the tagger. The plot in fig 4.7 shows a typical Bremstrahlung distribution of the produced photons. This distribution follows in a first approximation a $(1/E_\gamma)$ distribution as mentioned in [48].
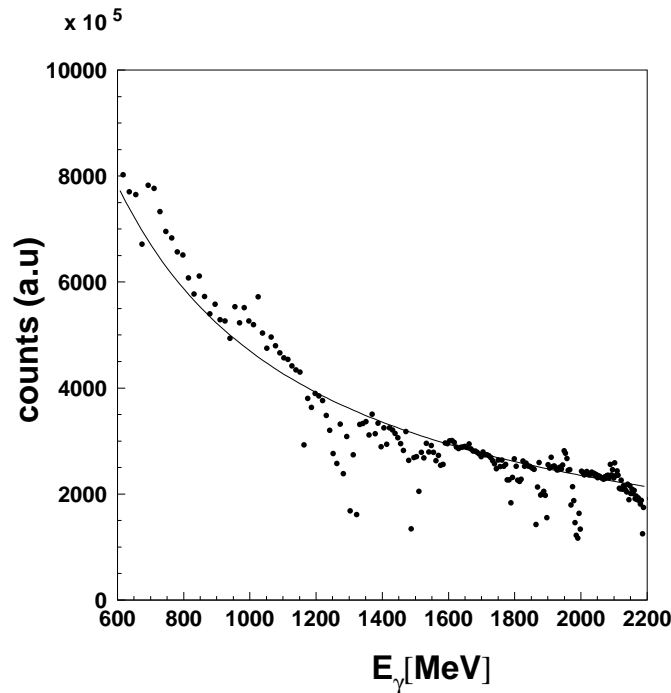

Figure 4.7: *Energy distribution of incident photons. Each point represent a binning of five tagger channels. A typical (1/E) distribution has been drawn (Data from this analysis).*

4.4.2   Tagging efficiency measurements

Nevertheless several effects induce a loose of the number of photons that reach the target. A first aspect is given by the characteristic opening angle of the Bremstrahlung. The half-angle between the emitted photon and the incoming electron beam for relativistic energies is given by ([49] , [50]) and is written as

$$< \theta^2 >^{\frac{1}{2}} = \frac{m_e c^2}{E}.$$

For a photon of 1.5 GeV the previous formula gives an half-angle of 0.3 mrad. Furthermore it should be pointed out that the beam has been collimated and therefore photons being at the limit part of the cone may be lost. As a consequence, the number of photons is systematicaly smaller than the number of the electrons, therefore the probability for a photon to reach the target or the so-called ϵ_{tag} " tagging efficiency " has to be estimated.

The principle of a tagging efficiency measurement is discussed next For this purpose dedicated runs called Tagger OR runs have been taken. In this configuration, the trigger is not made by the TAPS detector but by an OR between the 14 Scintillating Bars. During a tagger OR run, the number of photons is measured by the Gamma Veto detector. The TDC distributions are written as follows for the three detectors.

$TDC_{BAR} = T_{BAR} - T_{Trigger}$

$TDC_{Scifi} = T_{Trigger} - T_{Scifi}$

$TDC_{GammaVeto} = T_{GammaVeto} - T_{Trigger}$

where the the START is provided by the trigger signal. The STOP is made by the detector. The Number of photons is determined from coincident prompt events seen both by the Gamma Veto and the Tagger system. The determination of the tagging efficiency is therefore calculated according to:

$eff_{tag} = \frac{N_\gamma}{N_{e^-}}$

where N_γ is the number of photons measured by the Gamma veto and N_{e^-} is the number of electrons seen by the tagger in the mean time.

Chapter 5

Results

5.1 The η cross section

5.1.1 Total inclusive cross section

The total η inclusive cross section has been measured for different nuclei targets as function of the incident photon beam energy.
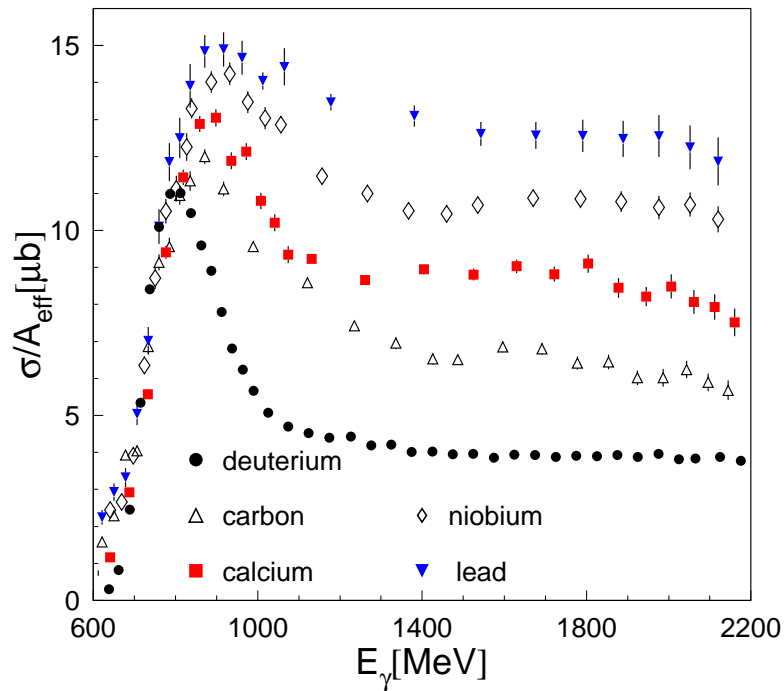

Figure 5.1: *Total full inclusive η cross sections normalized by the factor $(A^{2/3})$ where A is the number of nucleon and (2/3) is a scale factor. The cross sections off nuclei are compared with the deuterium cross section.*

The cross sections at the production threshold of the η mesons agree pretty well. The scale factor (2/3) shows a strong absorption effect of the η meson in the nuclear matter. This effect indicates that the detected η meson are produced close to the surface of the nucleus. The different cross sections behave differently at higher photon energy and seem to scale like the target mass. The scale factor α is re-fitted assuming a dependence on the incident photon energy using the following ansatz.
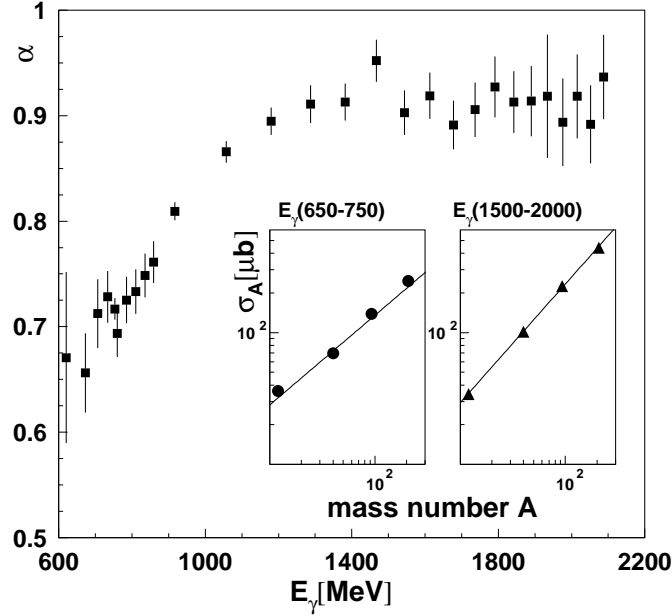
$$\sigma(A, E_\gamma) \propto A^{\alpha(E_\gamma)}$$

Figure 5.2: *Determination of the scale factor α as function of the incident photon beam energy*

A systematic deviation of the scale factor is observed for photon energies higher than 850 MeV. The evolution of the scale factor is in agreement with the observations from the LNS experiment (Japan) [24]. The scale factor constantly rises from 0.66 to 0.9 and seems to saturate around this value for photon energies higher than 1500 MeV. The total η cross sections are plotted in a log-log scale for two different beam energy ranges as function of the nuclear mass number A. For the two ranges of energy a clear linear dependence on the mass number is seen for the cross sections.

How this observation can be interpreted in terms of possible modifications of the $S_{11}(1535)$ resonance properties ?

On-going studies of the η cross section on light targets as proton and deuterium show a clear background contribution to the single η production. This feature becomes important at high photon energy where more energy in the center of mass is available and additional particles can be created, indeed a further π can be produced via the reaction : $\gamma + N \rightarrow \eta + \pi + N$.

This type of background is also expected for the nuclear targets. In the next plots, eight photons are detected. The invariant mass of the best $3\pi^0$ combination is plotted as function of the invariant mass of the two remaining γ. Assuming a selection on the two-photon invariant mass between 110 and 160 MeV the data are projected to the y axis and the resulting three π^0 invariant mass is shown in the top right plot of the fig 5.3. Data are also projected to the x coordinate with a cut surrounding the η mass, bottom left of fig5.3.

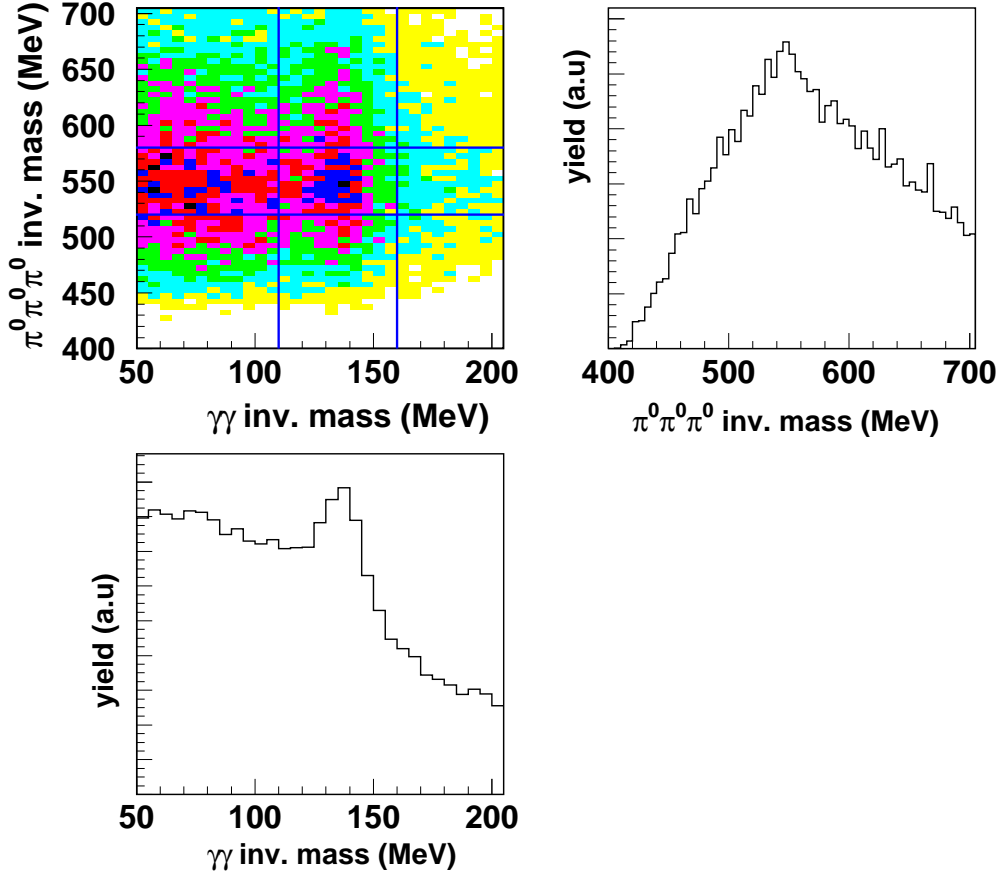Figure 5.3: *Top left: correlated η invariant mass in its 3 π⁰ decay vs. 2 γ inv. mass Top right: projection of the events to the y axes assuming a cut on the two gamma invariant mass between 110 and 160 MeV Bottom left: projection of the events to the x axes. The four lines indicate the cut applied before the projection.*

Furthermore, the total cross sections measured from nuclei nuclei indicate a clear enhancement of the cross sections at high energy which seems to be connected to the target mass. This effect suggests another kind of background, where a primary π is created and scatter on another nucleon. The resonance $S_{11}(1535)$ is excited and a so-called secondary η is produced. This scenario was first suggested in [44] and can be summarised like : vertex one : $\gamma + N \to \pi + X$
vertex two : $\pi + N \to \eta + N$

The determination of the resonance properties requires to analyse single η production. Thus, events with a further particle should be removed. Different possible scenarios concerning the creation of the η particle are drawn in the next sketch fig 5.4.
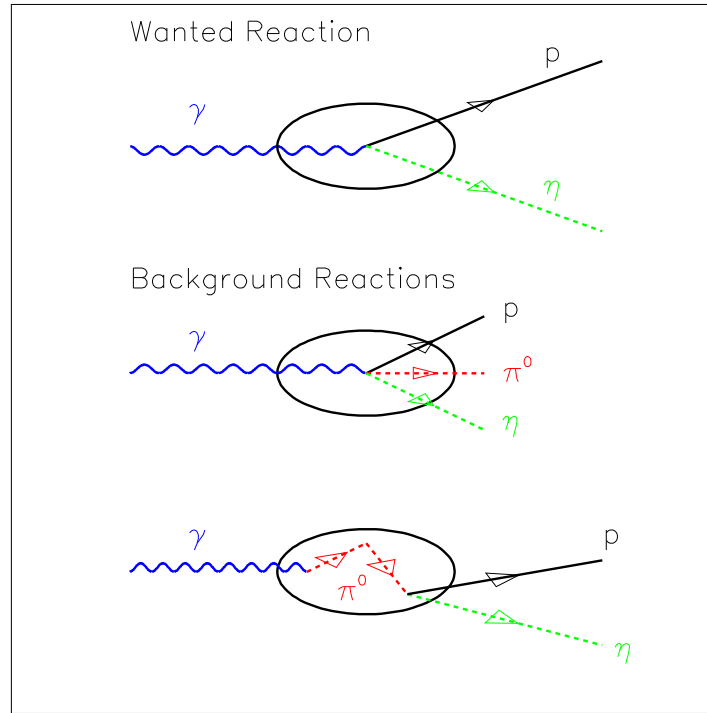

Figure 5.4: *Top plot: The plot shows a quasifree production of the η meson, a meson and a correlated nucleon are produced. Lower plot: Possible background contributions to the η cross section. The η meson can either be produced in a primary reaction with an additional π or during a secondary process where a π can interact with a nucleon and further create an η.*

Furthermore, the final state interactions between the η meson and the nuclear matter is only known for relatively small momenta of the meson in the energy range where the single η production is dominant as it was first demonstrated in [13]. Therefore the absorption effect of the meson in the matter at high kinetic energy remains an opened question. An additional hypothesis to explain the total cross section picture would be that at high kinetic energy the nuclear matter becomes transparent for the η meson. In that case, all nucleons would contribute to the production and therefore the entire volume of the nucleus could be probed.

5.1.2 Differential cross sections

To get more informations about the production mechanism of the η meson from nuclei differential cross sections in energy and angle may be considered. The differential cross sections have been measured for four beam energy ranges covering the threshold region up to photon energies of 2200 MeV.
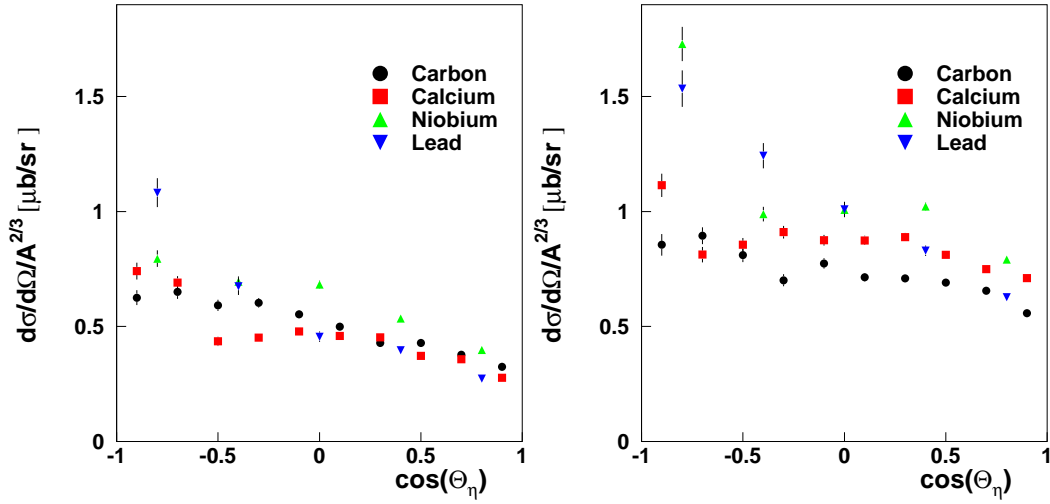
Differential angular cross sections

Figure 5.5: *Differential angular cross section in MeV unit: Left plot $E_\gamma = 650, 835$, Right Plot $E_\gamma = 835, 1050$*
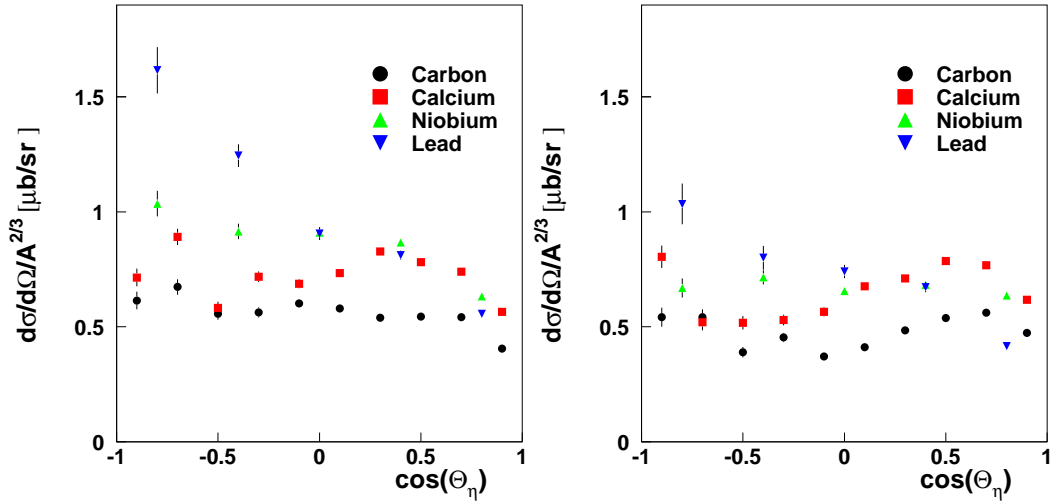

Figure 5.6: *Differential angular cross section in MeV unit: Left plot $E_\gamma = 1050, 1550$, Right Plot $E_\gamma = 1550, 2200$*

The cross sections are expressed in $(\mu b/sr)$ and plotted as function of $cos(\theta_\eta)$ where the θ_η angle is the polar angle of the emitted η relatively to the beam direction. This quantity is calculated in the center of mass (CM) of the $(\gamma - nucleon)$ system. The differential cross sections are normalized by the scale $A^{2/3}$ and agree pretty well near the reaction threshold. The observed asymmetry in the backward to forward region is predictable since the $(\gamma - nucleon)$ system used to plot the angular distribution is moving faster than the true CM system. This effect explains why the angular distribution is shifted towards backward angles. At higher energies the calculated $\gamma - Nucleon$ system can move slower than the true one, nevertheless both cases occur which means that on average the distribution should not be influenced by this effect. For photon energies around $E_\gamma \propto 850 MeV$ the cross section off heavier targets show a systematic difference from lighter one in the backward region and this effect is more pronounced with increasing photon energy. The reason for this effect might be due to a relatively more important contribution of low energetic η mesons in the case of heavy targets. This situation most likely happens when enough energy to create additional particles is available such that η's are produced during secondary reactions. A primary π can be created in the nuclear matter, propagates and induce the creation of a secondary η. An additional interesting feature is observed for the highest energy beam range. The measured cross sections for Calcium and Carbon seem to peak at the forward direction. This effect is not seen for the heaviest targets Lead and Niobium. This observed peaking distribution has been measured for the proton target when looking at excusive measurement $\gamma + p \rightarrow \eta + p$ at high incicent photon energy [26]. The next plots show the cross distribution measured from the proton for two incident beam energy ranges.

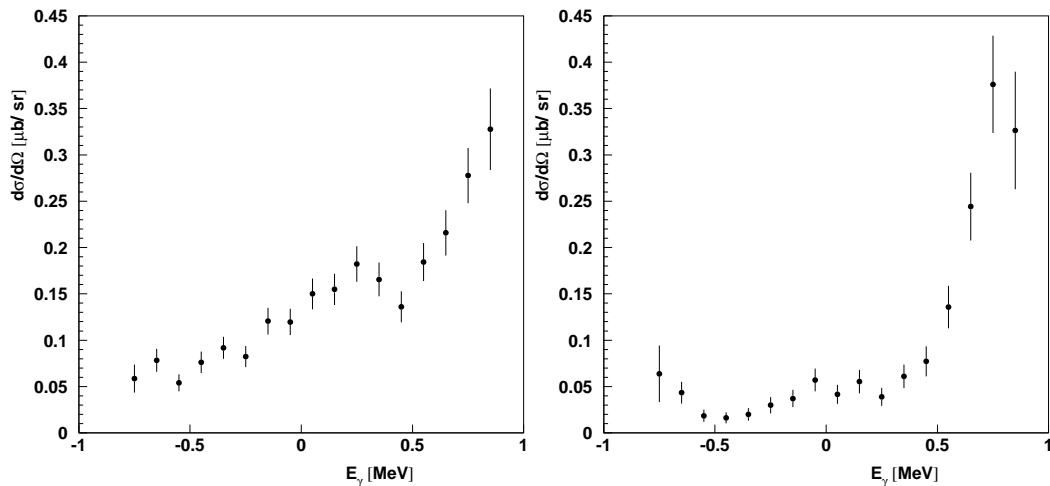Figure 5.7: *Energy differential cross section in MeV unit for the proton target: Left plot $E_\gamma = 1550, 1600$, Right Plot $E_\gamma = 2150, 2200$*

The forward peaking get more pronounced at high energy. Since the cross sections off nuclei are measured over a much broader range of photon energies a fair comparison with the proton could be done by making an average of the proton cross sections in these energy ranges.

Differential energy cross section

Further informations are obtained by looking at the evolution of the differential cross as function of the kinetic energy of the η.
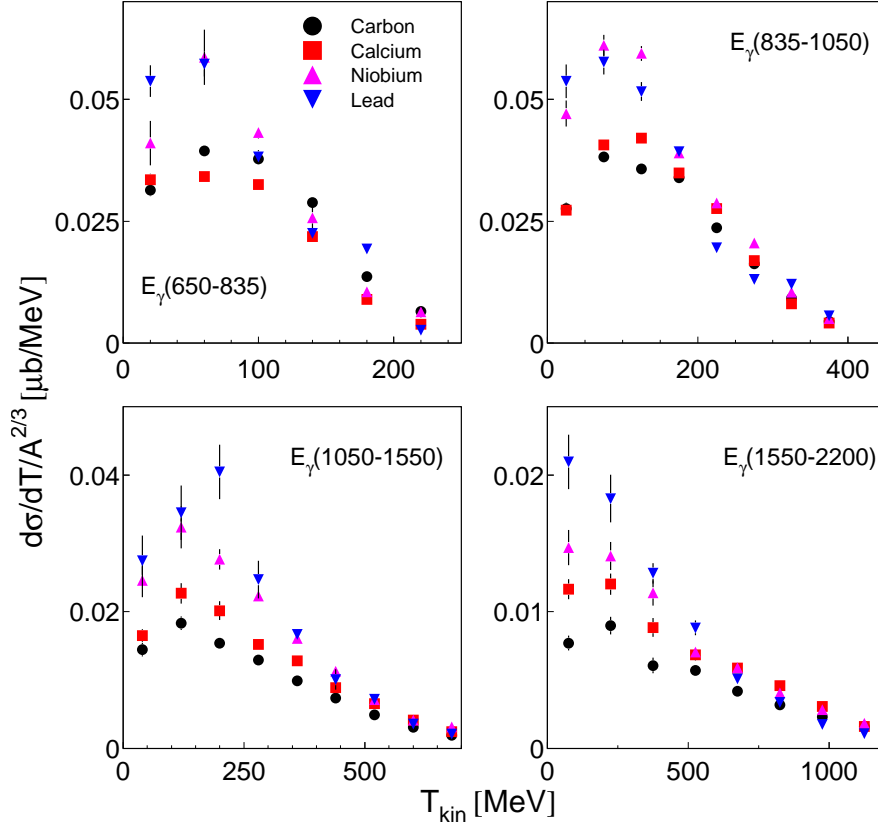

Figure 5.8: *Differential energy cross section in MeV unit for different beam energy ranges*

The differential cross sections in energy are normalized by $A^{2/3}$ As for the angular distributions, the cross sections are measured for different ranges of the photon energies. A systematic enhancement of the signal is observed for heavy target mass in comparison to the lighter one for the low meson kinetic energy and the cross sections seem to converge for the highest kinetic energy. This feature is explained when secondary production mechanisms play a significant role. For the highest kinetic energy T_η not enough energy may be used to create additional particles, therefore only reaction like $\gamma + N \to \eta + N$ without much rescattering can contribute.

5.1.3 η FSI in nuclear matter

The missing mass of the η event can be plotted for different beam energy ranges. In the next pictures (fig 5.9) and (fig 5.10) the missing mass distribution of the η meson is plotted for the two extreme cases of the photon energy range.
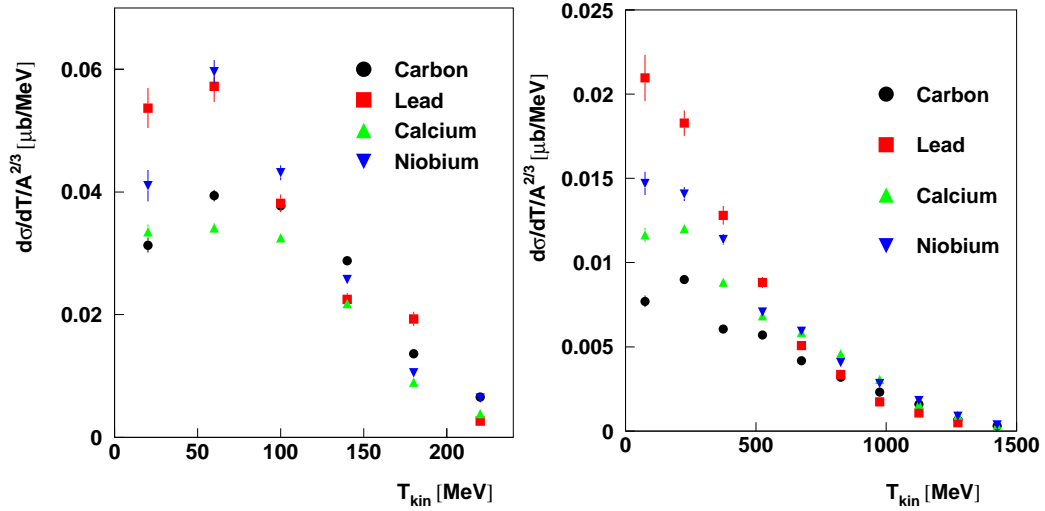
Figure 5.9: *Left plot : Diff. cross section in energy for beam range in MeV unit (650,835) Right Plot : Diff. cross section in energy for beam range in MeV unit (1550,2200)*
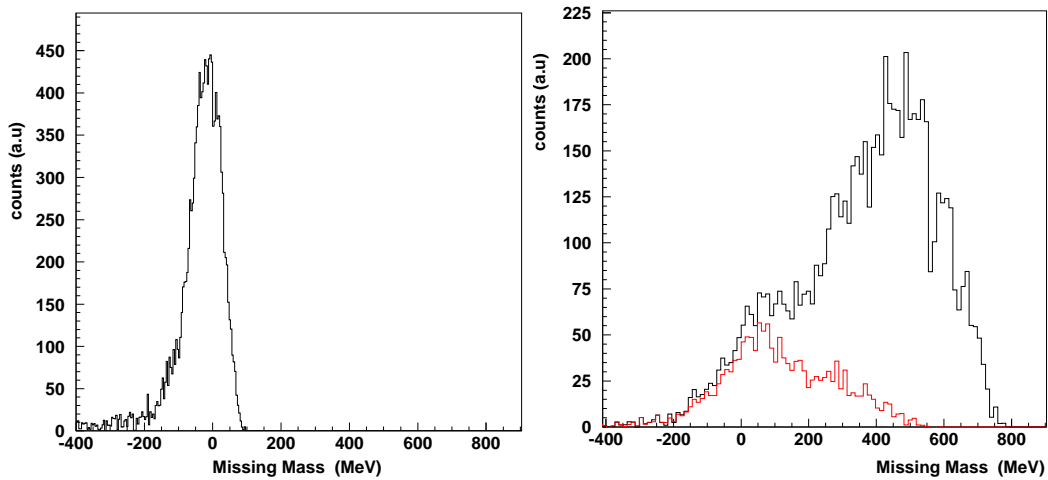

Figure 5.10: *Left plot : Missing mass events for beam range in MeV unit (650,835) Right Plot : Missing mass events for beam range in MeV unit (1550,2200), the lower curve centered around the nucleon mass (events at 0 in this curve) corresponds to events with kinetic energy higher than 700 MeV.*

At the reaction threshold the cross sections scale approximately like $A^{2/3}$ and the missing mass distribution indicates single η production. For the highest photon energies, the full missing mass distribution clearly shows a high background level. Most of this background is removed when taking only into account events with high kinetic energy. This is due to the fact that when a further particle is created not enough energy is available so that the η can have large energy. The second point is that the four different cross section seem to converge towards the largest kinetic energy when using the normalization $A^{2/3}$.

A new estimate of the scale factor α is done for the four beam ranges considering only events with the following condition :

$$T_{kin} > 0.5(E_\gamma - M_\eta).$$

Where the maximum η kinetic energy is $E_\gamma - M_\eta$, in this approximation the full energy of the system is transfered to the η. The scale factor is re-fitted using the four target cross sections and the simple ansatz $\sigma(A) \propto A^\alpha$
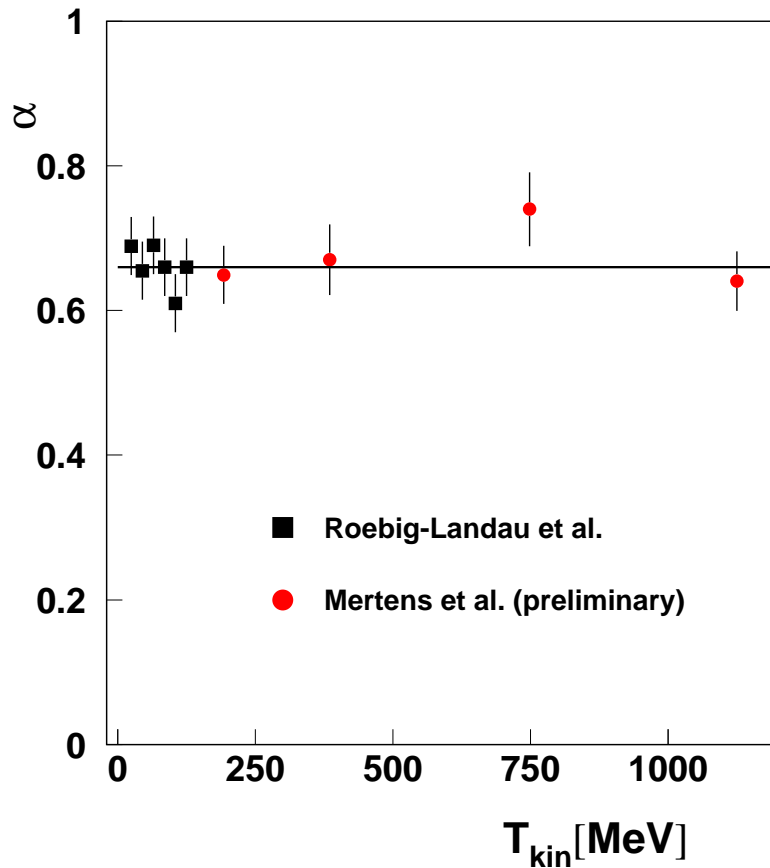.

Figure 5.11: *Determination of the scale factor from the energy differential cross section when keeping events with at least 50 % of the maximum kinetic energy. The squared points are data from Mainz. The circle are data from this work.*

As is shown in (fig 5.11) the scale factor looks more or less constant as function of the η kinetic energy close to a value 2/3. Near threshold this result confirms previous experimental data and extends the information about $\eta - nucleon$ absorption towards kinetic energies up to 1200 MeV.

Simple assumptions can be made concerning the determination of the η mean free path in matter using the frame work of the Glauber theory. As explained in the introduction this model assumes the dominance of the quasifree production. In the present case, the cuts applied on the kinetic energy remove most of the background from secondary η's or primary produced $\eta\pi$ and only single quasifree η are included.

Therefore the Glauber model may be used and the absorption cross section of the η meson can be related to the scale factor α extracted from the fitted data as shown in fig5.13
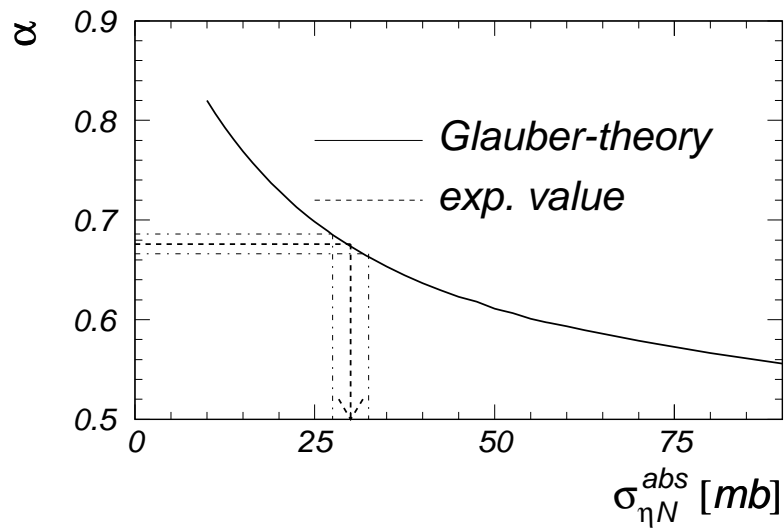

Figure 5.12: *correspondance between the fitted scale factor and the absorption cross section $\sigma_{\eta N}$ The curve is taken from [47]. The dash points corresponding to a scale factor α of 2/3 indicate an absorption cross section of 30 mb. The dot-dashed points indicate the range of the errors both for the α and the absorption cross section.*

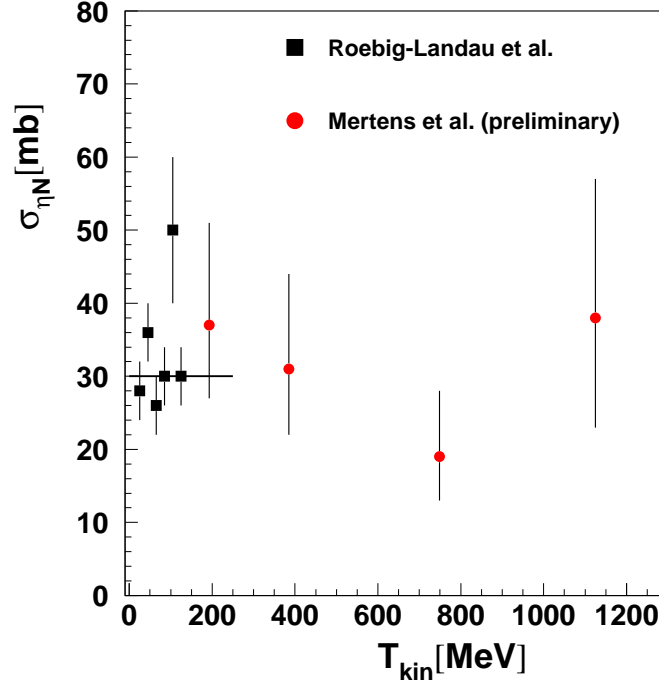The corresponding absorption cross sections $\sigma_{\eta N}^{abs}$ are then deduced from the fitted scale factor α.

Figure 5.13: *Evolution of the absorption cross section $\sigma_{\eta N}$ as function of the η kinetic energy. The error bars are not symmetric due to the evolution of the absorption cross section $\sigma_{\eta N}^{abs}$ as function of the α factor. The squared points are from [13]. Circle points are data from this work.*

The resulting $\sigma_{\eta N}^{abs}$ shows a more or less constant value around 30 mb.
The η mean free path is related to the absorption cross section via

$$\lambda = \frac{1}{\rho_0 \sigma_{\eta N}} \tag{5.1}$$

where ρ_0 is the normal nuclear density 0.168 (fm^{-3}). A constant value of the η mean free path around 2 fm is found.

5.1.4 Determination of the resonance in-medium properties

The extraction of the resonance properties requires to identify events from the decay of the $S_{11}(1535)$ into the ηN channel. In this chapter two different methods have been tested in order to probe the $S_{11}(1535)$. The first method considers missing mass criteria while the second one is based on a selection of the kinetic energy of the produced η's.

Strategy 1

As explained in an earlier chapter, the missing mass analysis is based on the condition that a single meson is created and the coincident nucleon is treated as a missing particle. Events with a missing mass smaller than 140 MeV are kept and used to extract the cross sections. The effect on this cut is shown in (fig 5.15) for the energy differential cross sections.
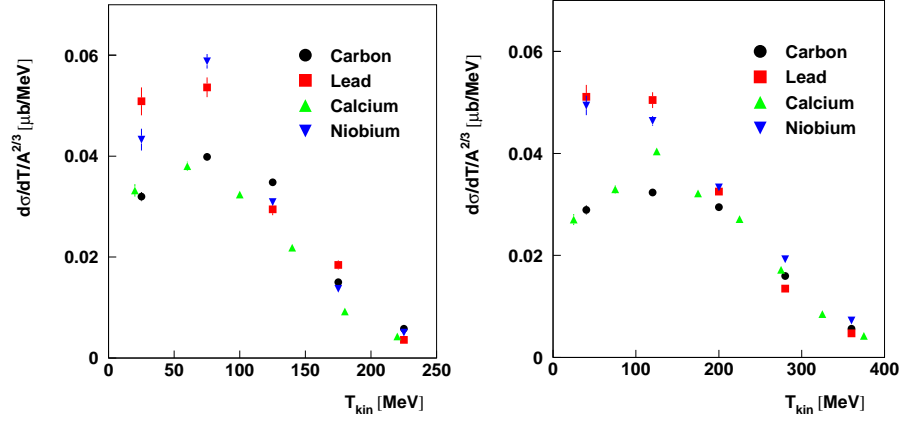
Figure 5.14: *Range of the Photon beam energy in MeV : Left (650,835) , Right (835,1050)*

This cut does not seem to affect the cross sections for small photon beam energies. Larger effects are observed at higher energy.

Figure 5.15: *Range of the Photon beam energy in MeV : Left (1050,1550) , Right (1550,2200)*

A lot of strenght is removed at high energy, espacially for the low kinetic ranges. The cross sections also more or less scale like $A^{2/3}$ for the η's of high energy.

The influence of the missing cut is also studied for the angular distributions in fig 5.17
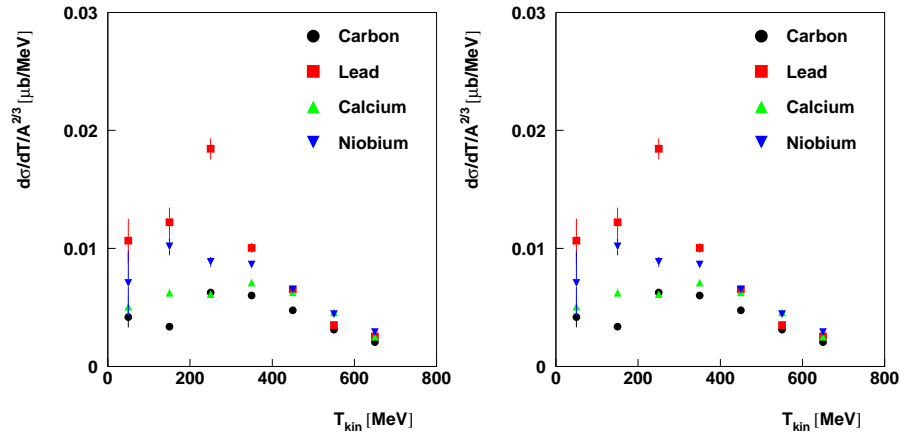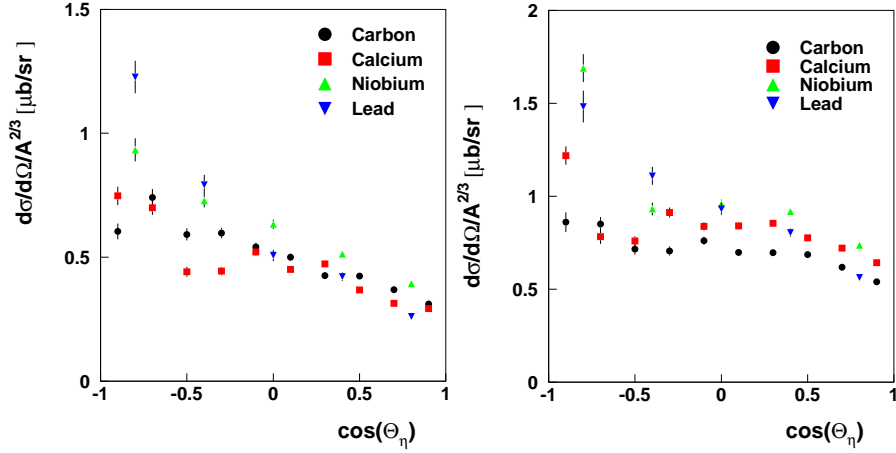

Figure 5.16: *Range of the Photon beam energy in MeV : Left (650,835) , Right (835,1050)*

As for the energy distribution this cut does not affect cross sections measured at low photon beam energies.
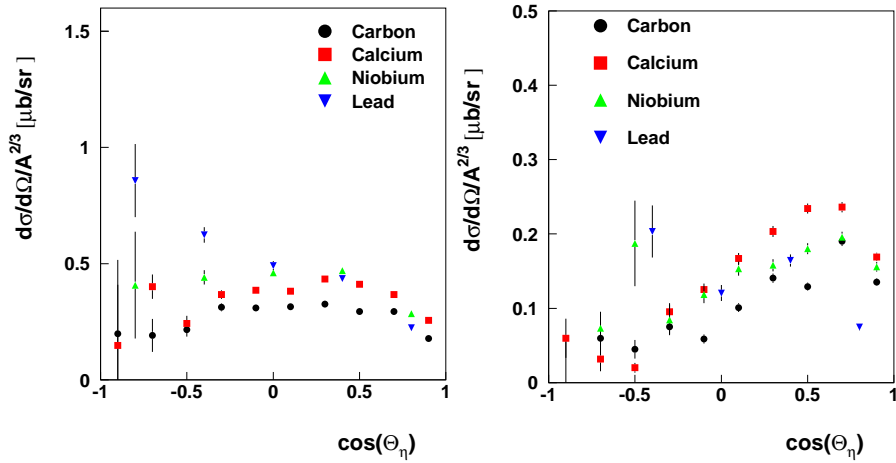
Figure 5.17: *Range of the Photon beam energy in MeV : Left (1050,1550) , Right (1550,2200)*

The missing mass cut on the highest energy range shows a more pronounced forward to backward asymmetry in the distribution lineshape in comparison to the full inclusive angular distributions. This effect becomes also visible for the Niobium target. The lineshape of the cross sections measured from nuclear targets get closer to the cross section distributions extracted from the proton by [26] where only single η's are taken into account in the cross section.

The total η cross sections for both carbon and lead data are shown in (fig 5.19).
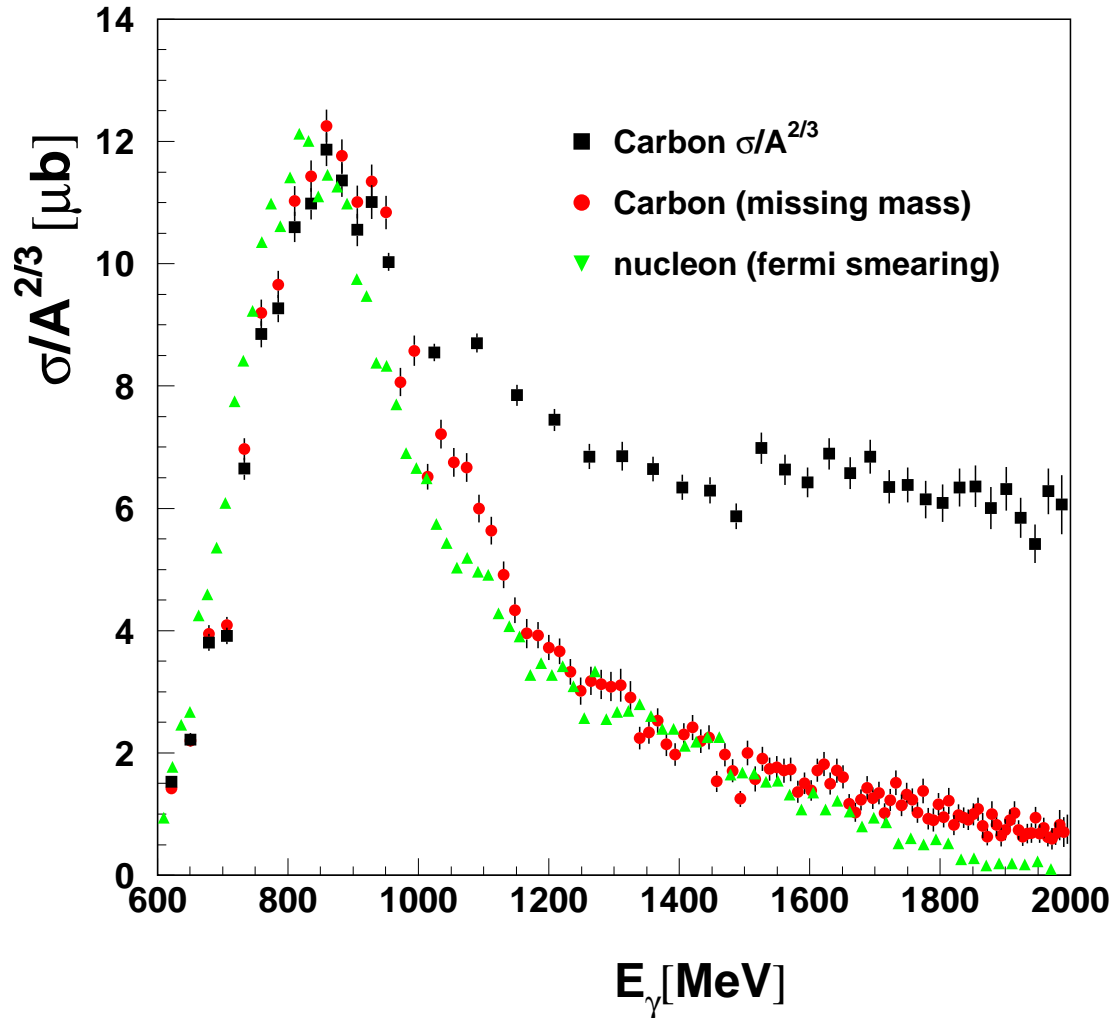
Figure 5.18: *Squared: Cross section from the carbon target. The normalization factor $A^{2/3}$ is applied to the data. Circle: The cross section is measured with a missing mass cut at 140 MeV. Triangle: The Fermi motion of the carbon nuclei is folded in the nucleon cross section taking into account the cross section lineshape of both the proton and the neutron.*

The effect of the missing mass cut is visible above incident photon energies of 900 MeV and becomes very important for high photon energies. The Fermi smeared nucleon lineshape has been deduced from both the proton and the neutron cross section lineshape taking into account the proportion of protons and neutrons for the target of interest. For the purpose of this analysis the neutron cross section has been approximated by the MAID model as explained in [53],[54],[55]. The plot in fig 5.21 shows both the proton and neutron lineshape where the maxima of the cross sections have been adjusted such that the enhancement of the cross section off the neutron for photon energies around

1 GeV becomes visible. The ratio of both distribution is also shown, the bump around photon beam energies of 1050 MeV indicates a clear enhancement of the neutron cross section. This could be due to a stronger coupling of a resonance into the $\eta - neutron$ channel than with the $\eta - proton$ channel.

Values of the photon beam are chosen according to the distribution probability of the cross section lineshape. For each photon beam a value of the Fermi momentum distribution corresponding to the nucleus of interest is randomely chosen. The corresponding new center of mass energy $\sqrt{s}$ is calculated. Finally a new value of the photon beam is calculated from this new (CM) energy which can be either larger or smaller than the initial one. The normalization of the Fermi smeared nucleon curve is done arbitrarely such that it agrees with the threshold region of the cross section measured from the nucleus.
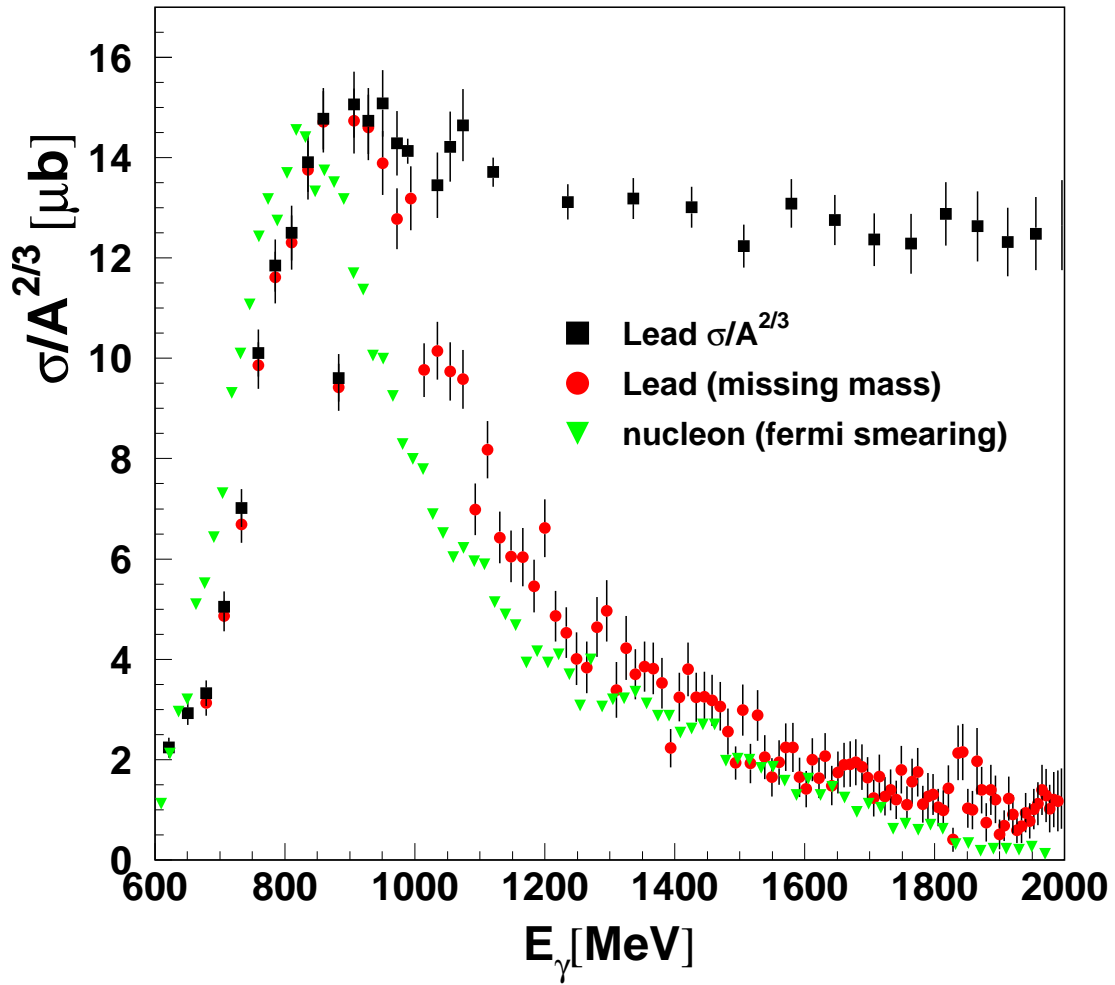
Figure 5.19: *circle points: cross section from Lead. The normalization factor $A^{2/3}$ is applied. square: The cross section is measured with a missing mass cut at 140 MeV triangle: The Fermi motion of the lead nuclei is folded in the nucleon cross section taking into account the cross section lineshape of both the proton and the neutron.*

The cut on missing mass removes most of the background and work pretty well at high energy but is not so efficient in the intermediate range between 800 and 1200 MeV. The observed difference between the Fermi smeared nucleon and the cross section may highlight a possible in-medium effect of the resonance but may also be obscured by an artificial background effect. The deviation to the Fermi smeared nucleon is more pronounced for the lead than for the carbon. The difference between lead and carbon may be partly explained by Fermi smearing and absorption effect which can be more important on the heaviest target. As a further explanation, the cross section from lead gets a much higher level around 900 MeV in comparison with the carbon. This difference can be explained by an excess of η created during secondary processes. Since the cut on the missing mass gets efficient at high photon energies, this background to

the single η can not be removed.

The next plot compares the cross sections for the different with the deuterium assuming the missing cut at 140 MeV. As described earlier the effect of the cut becomes visible for energy above 900 MeV, the cross sections seem to converge for the high energy photons.
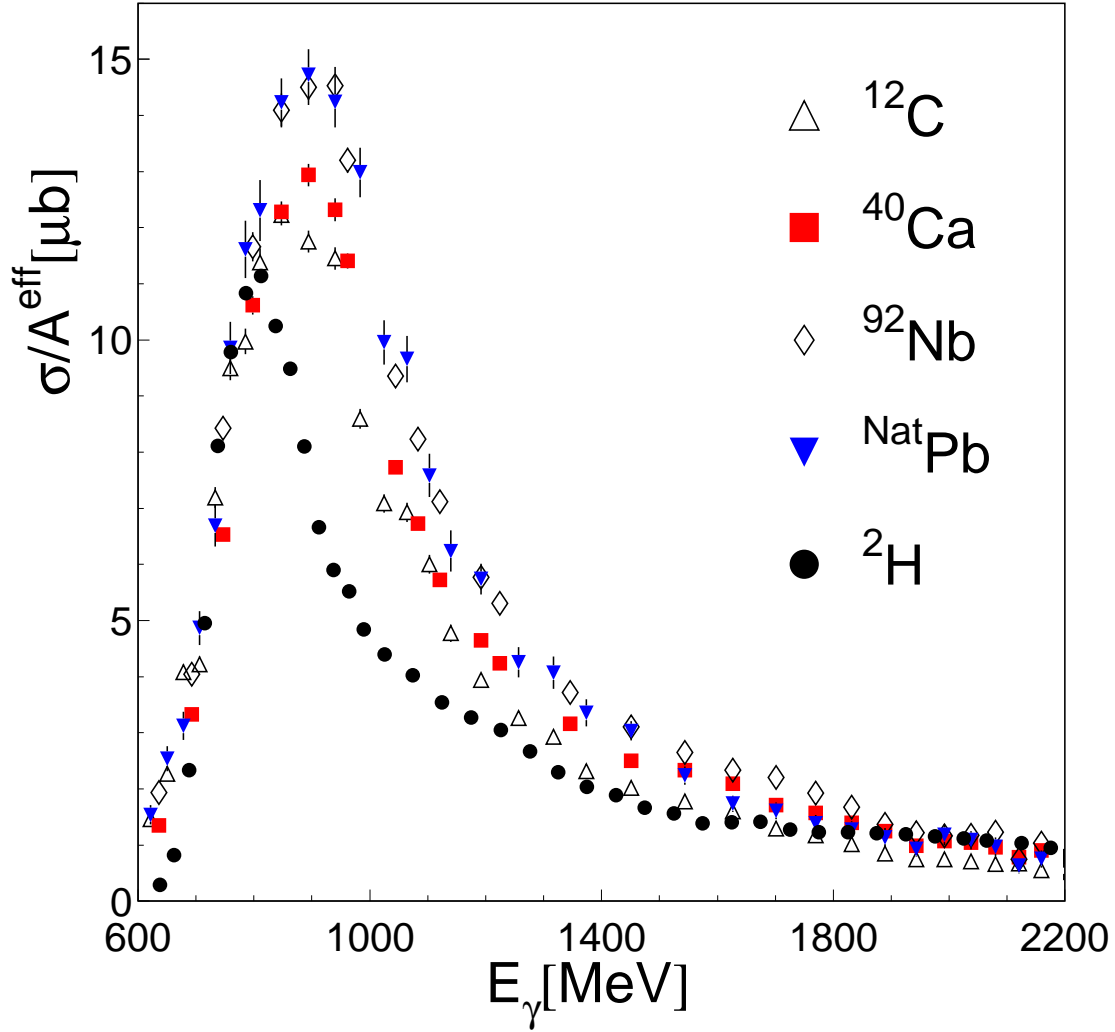
Figure 5.20: *Cross sections for the different nuclei including the deuterium target with the missing mass cut.*

In comparison with the next strategy based on a selection of the kinetic energy the missing mass cut allows to consider events for all the possible range of the η energy.
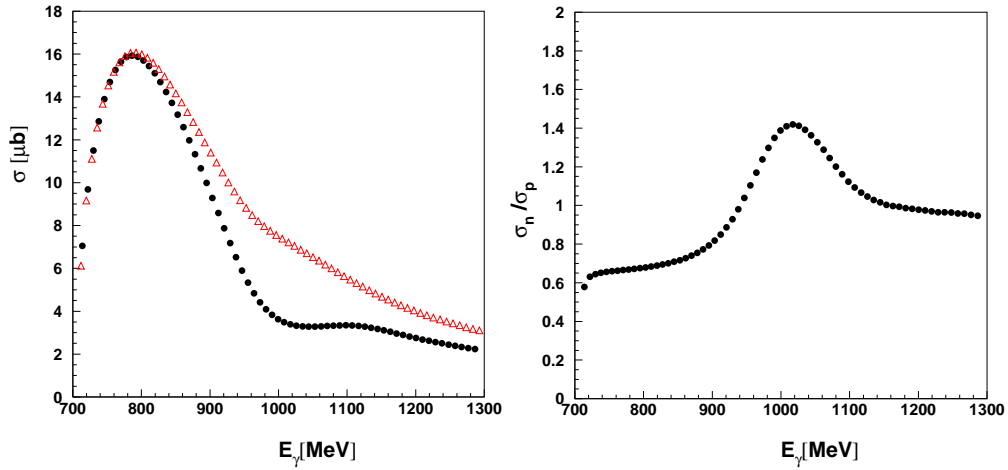
Figure 5.21: *Left: MAID predictions for the proton and neutron cross sections. Both curves are relatively normalized. Right: Neutron to proton ratio of the absolute cross sections.*

Strategy 2

The exclusive measurement of a coincident proton or neutron with an η is impossible for a nucleus, nevertheless a good compromise can be done when searching for a quasifree reaction by keeping events with relatively high kinetic energy. This cut on the η energy leads to a leak of statistic but has the advantage to remove most of the background to the single η production and give the lineshape of $S_{11}(1535)$ made of the most energetic $\eta's$ as can be seen next (fig 5.22)
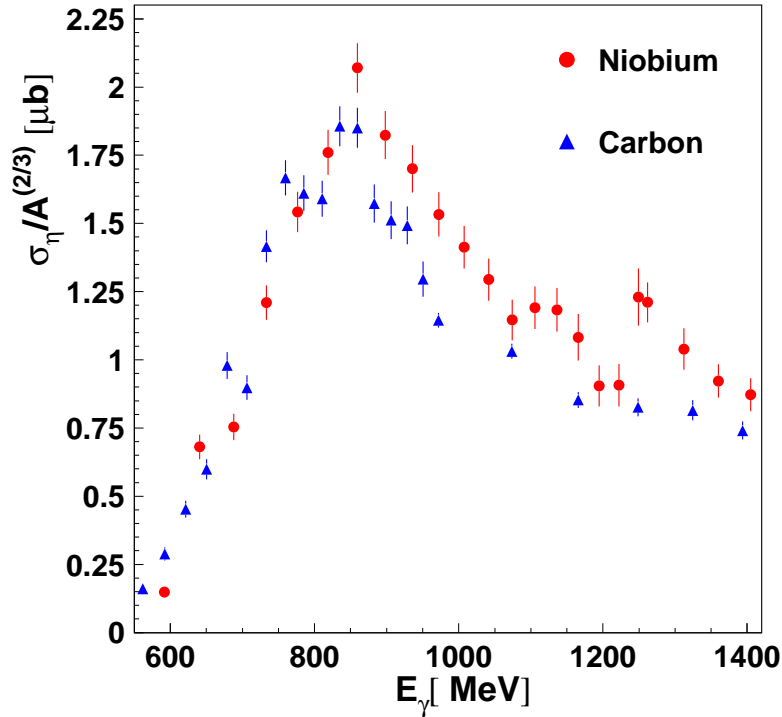
Figure 5.22: *Comparison carbon to niobium data when only keeping events with at least 70 % of the maximum possible kinetic energy for the corresponding incident photon beam energy*

Both carbon and niobium data are compared assuming a scale factor of $A^{2/3}$. A small deviation around 1.2 GeV photon energy is observed, and the width of the $S_{11}(1535)$ measured via η photoproduction from niobium seems to be $\pm$ 50 MeV larger than the one for the Carbon. It should be pointed out that in comparison with the previous method based on missing mass considerations, the maximum of the cross sections for the two nuclei is almost equivalent and is reached for a photon energy of 850 meV. The question is asked if the applied cut removes relatively more background on lighter nuclei or if a real in-medium effect is observed. Both nuclei cross section seem to converge towards the same lineshape at higher photon energies. These questions can be studied by a detailed comparison of data and the results of the BUU simulations which contains only trivial in-medium effects (see next chapter, Comparison to theoritical models).

5.2   The double π^0 cross section

In order to investigate the second resonance region, another resonance, the $D_{13}(1520)$ has been studied via the double π^0 reaction.
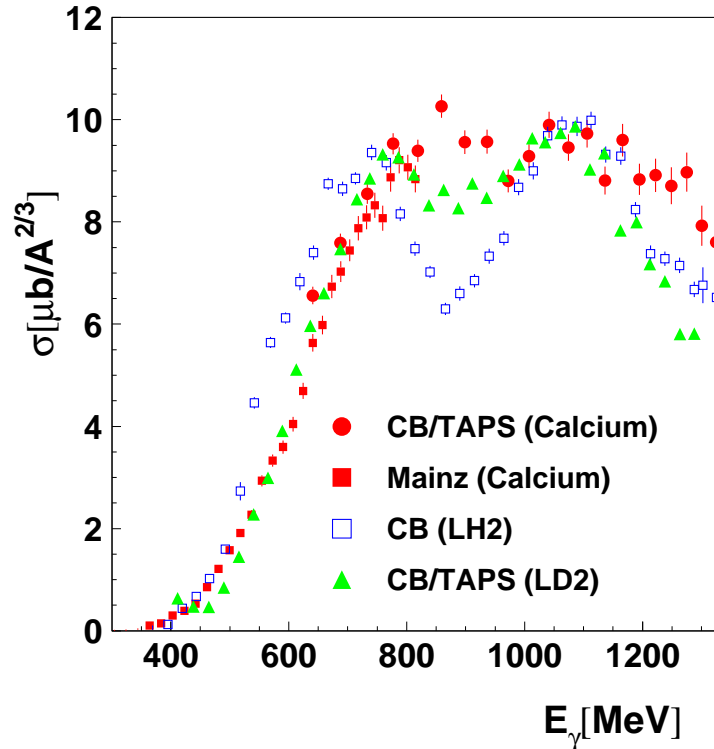
Figure 5.23:   *Comparison $\pi^0\pi^0$ cross section off calcium between Mainz and CB/TAPS data. open squared: Data off proton, triangle : deuterium data*

A good agreement is found between the Mainz data and the one from the CB/TAPS collaboration for the Calcium nucleus.

It is important to point out that the depletion between the two peak structures on the deuterium seems to be already significant. This difference to the proton data could be explained by a different cross section off the neutron. On going analysis are on the way to measure the exclusive cross section of the double π^0 channel from both the proton and the neutron. Furthermore, the measurement of the cross section from the Calcium shows an almost complete disappearance of the valley between the second and third resonance region. In addition to the different cross section between the proton and the neutron a pure in-medium effect like the broadening of the $D_{13}(1520)$ resonance width could contribute. This feature has been predicted by the calculation of the Giessen theory group. The Fermi smearing alone can not explain the depletion, more sophisticated effects should contribute. Going further, this disappearance might help to understand the result from Bianchi et al. [16] where the two bumps corresponding to the second and third resonance region are not visible when looking at nuclear targets.

5.3   Comparison to theoritical models.

The experimental results need to be compared with theory in order to get a better understanding of the production mechanisms of the η meson. The different contributions to the η have to be determined by adjusting the model parameters to the data.

5.3.1   Total inclusive cross sections

The cross sections for the different nuclear targets are compared to the BUU simulations from [56] for both the case with missing mass cut in fig5.25, and for the full inclusive in fig5.24.
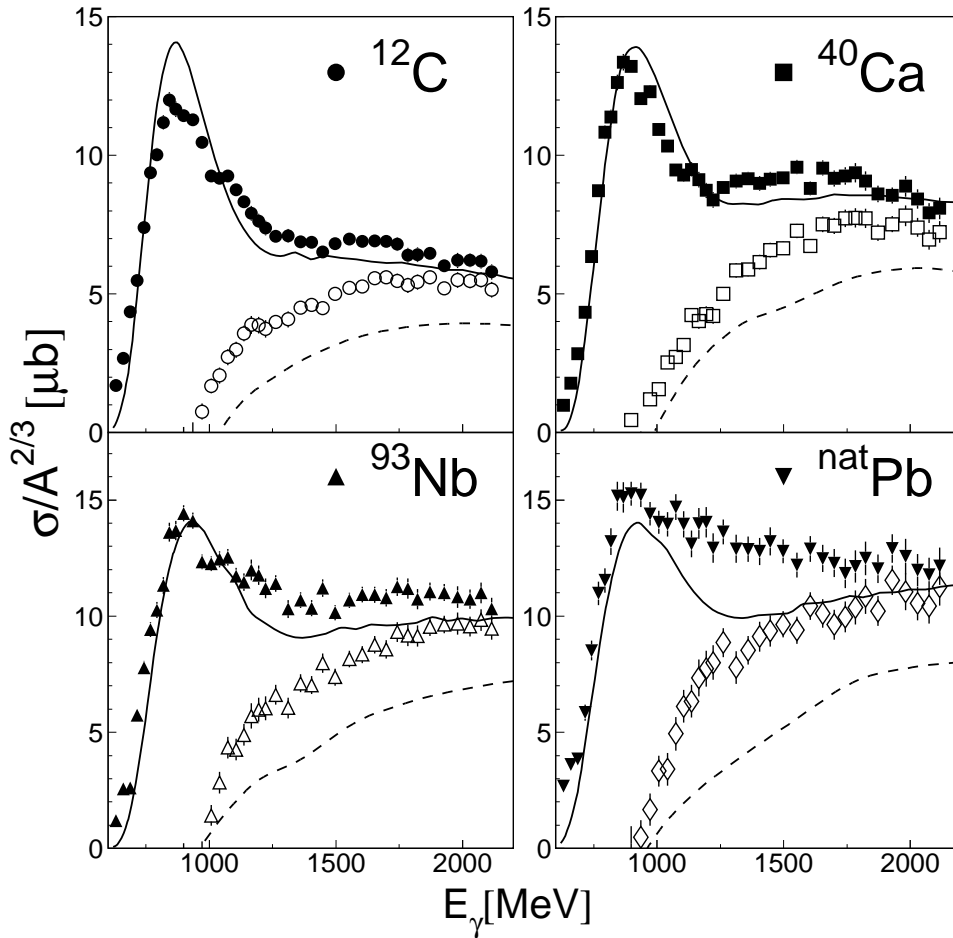
Figure 5.24: *Filled symbols: inclusive cross sections (solid curves: BUU results). Open symbols: difference of inclusive and exclusive single η production (dashed curves: BUU results).*

5.3.2   Cross sections with missing mass cut
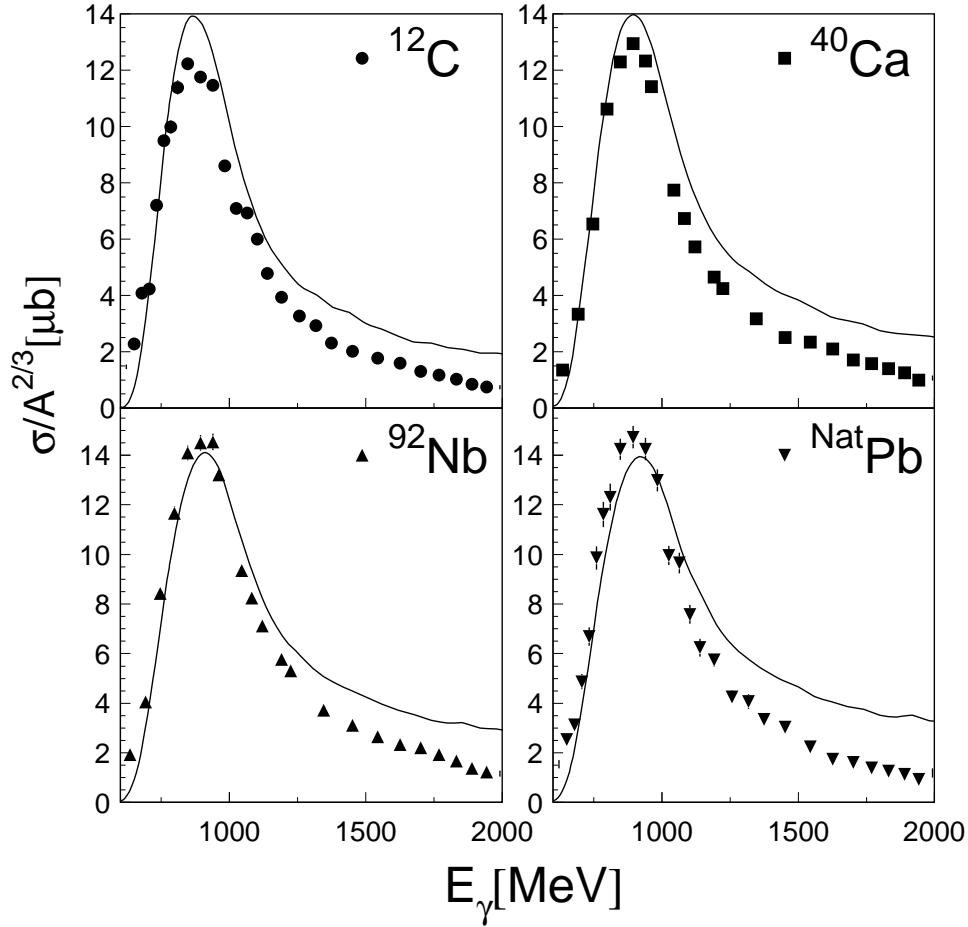
Figure 5.25: *Comparison of the total exclusive single η-production cross section(missing mass cut at 140 MeV) to BUU results.*

Some discrepancies between the data and the simulations are visible. For the Niobium and Lead targets, some missing strenght is observed on the simulations for photon beam energies around 1300 MeV. This difference could be explained by a relatively stronger contribution of low energetic η's on the heavier targets, where primary π are produced and induce the creation of these η' s via rescattering processes. The analysis of the different contributions to the η cross section and their relative strenght is on the way.

5.3.3 Angular Differential cross sections
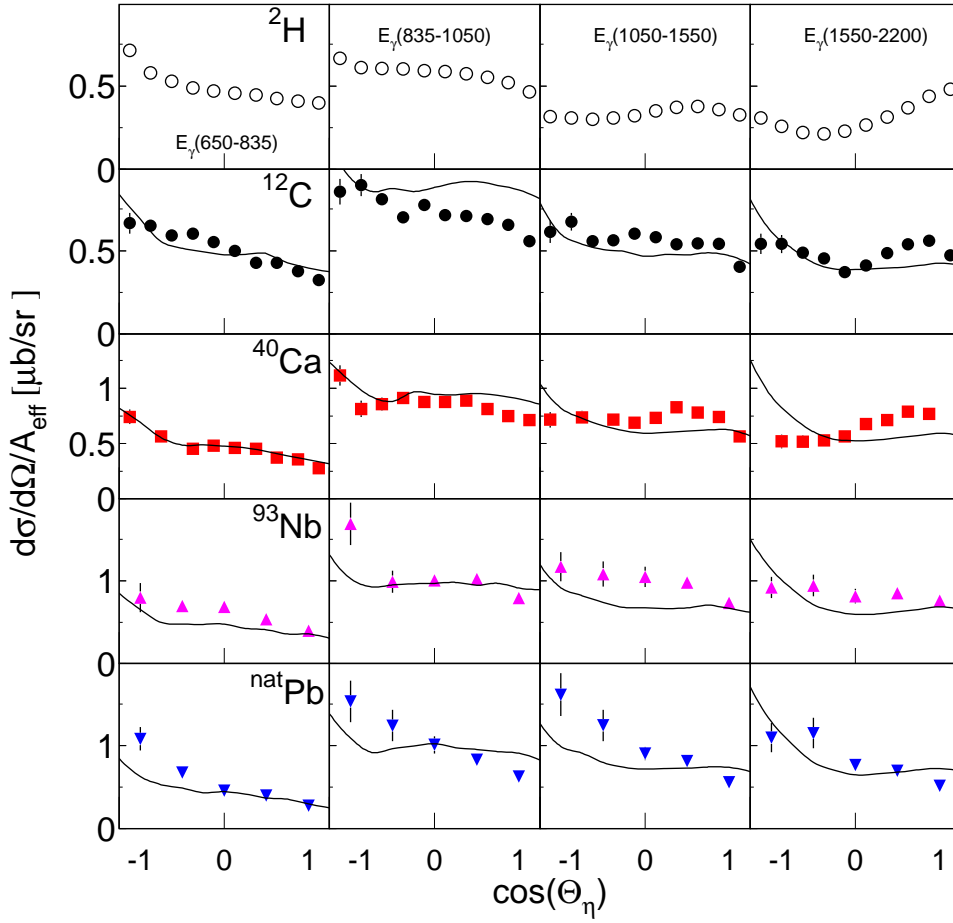
Figure 5.26: *Comparison between data for angular differential cross sections for the different targets with BUU models for four ranges of incident beam energies. The Deuterium data are plotted for comparison.*

Disagreements seem to be observed specially for the heaviest targets. A larger bunch of events are measured in the backward region. This could indicate that the model underestimate the production of $\eta\pi$ events primarely or the creation of secondary η's created due to primary pions.

5.3.4   Mass Differential cross sections

Next the mass differential for both Carbon and Leads are extracted for two beam energy ranges.
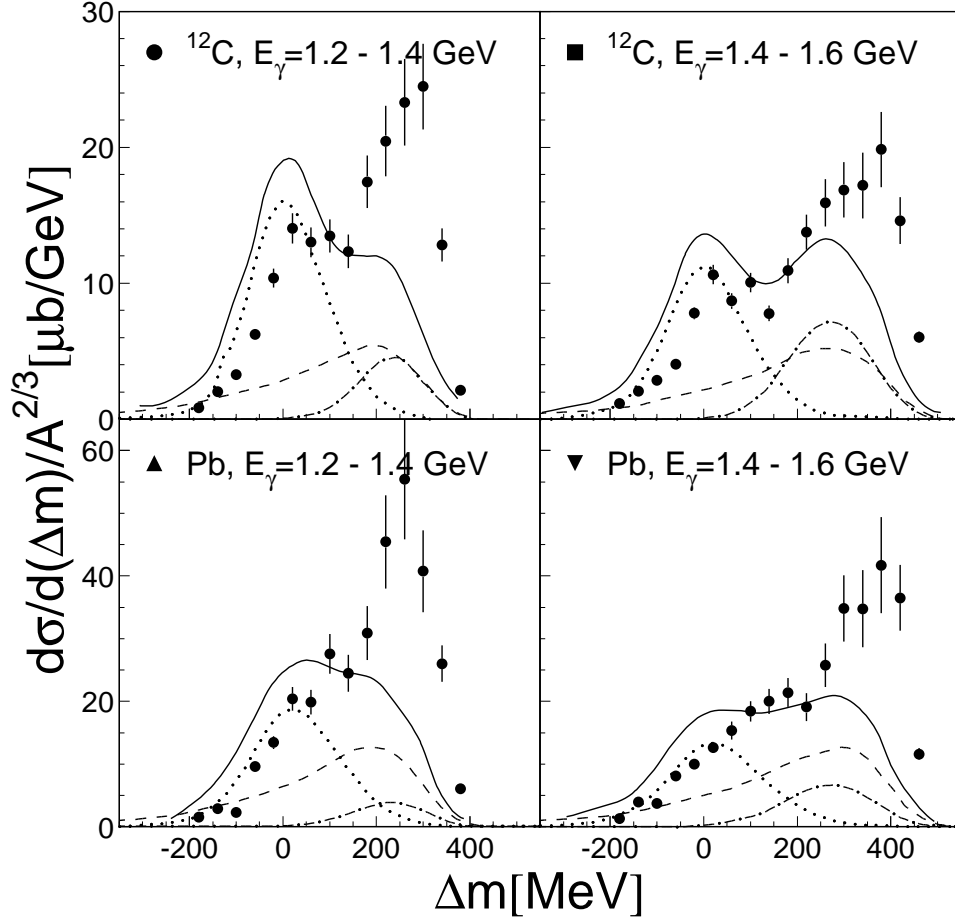
Figure 5.27: *Missing mass spectra for carbon and lead for two ranges of incident photon energies. Curves: BUU-results for full model (full curves), single, quasi-free η production (dotted), ηπ final states (dash-dotted) and secondary η-production(dashed).*

In comparison with the BUU model a significant number of events are located in the regin around 300MeV. These bumps could correspond to a bunch of correlated $\eta\pi$ events for which the strenght is underestimated in the simulations.

5.3.5   Event Selection on the kinetic energy

In this case the Niobium data are compared to the simulation from [56] using some conditions on the kinetic energy of the η. The kinematical selection on the η meson is applied in the same way than in the data. For that purpose a condition on the kinetic energy of the η is applied such that events must have at least 70 % of the maximum kinetic energy

$$T_{kin} > 0.7(E_\gamma - M_\eta).$$

This method removes most of the background due to rescattering processes. The kinematic selection induces that the cross section is extracted only with fast η's. The good agreement between data and model indicates that no strong depletion or unexplained features seem to affect the $S_{11}(1535)$ as seen in fig 5.28.
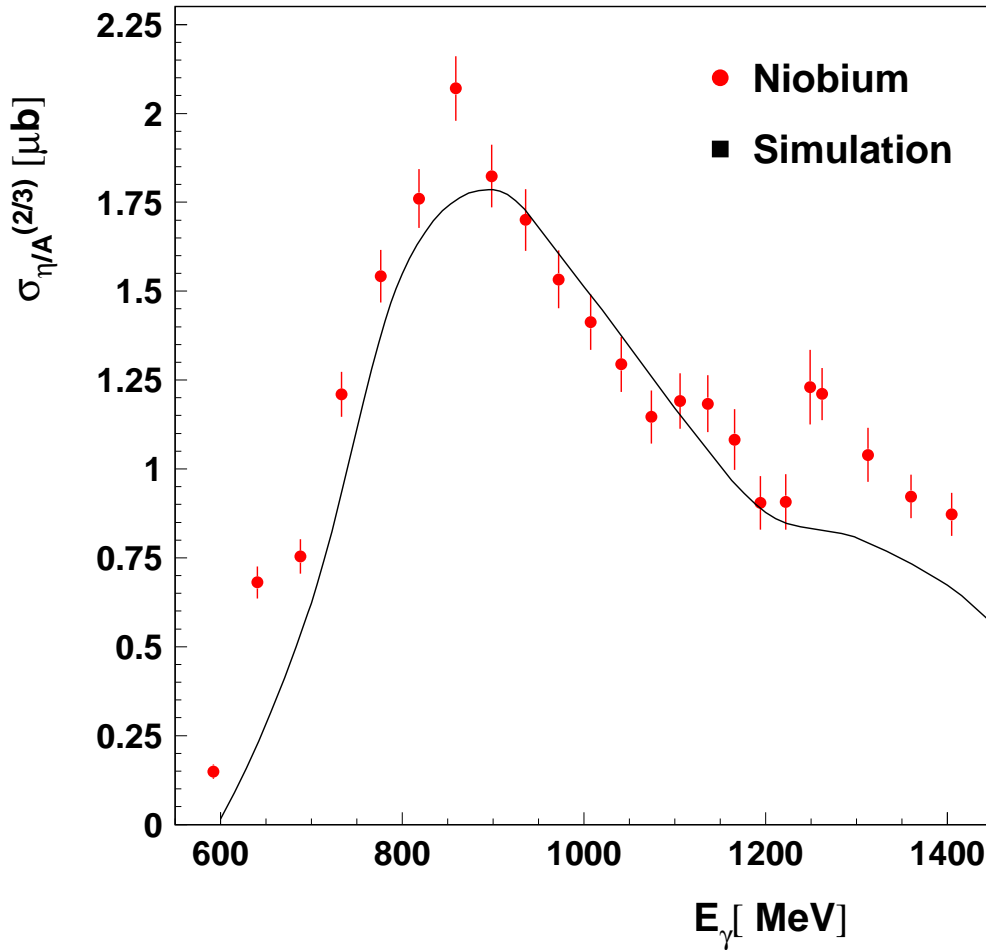
Figure 5.28: *Comparison between the measured cross section off niobium to a BUU simulation from Pascal Muehlich.*

5.3.6   Study of the angular distributions

The angular cross sections off protons measured by [26] are taken as an input to the BUU simulations.
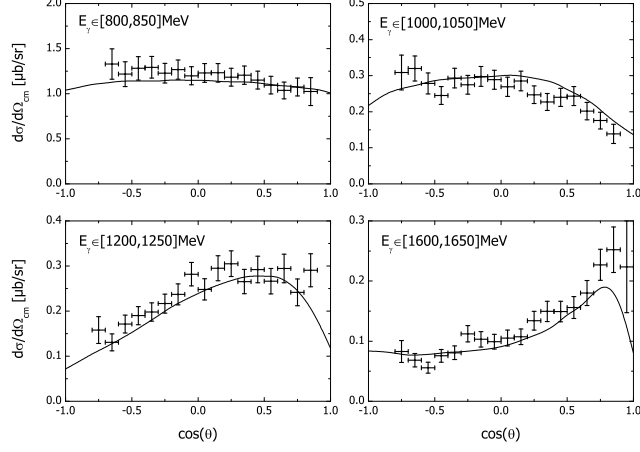
Figure 5.29: *Angular differential cross sections off the proton target for different energy beam ranges. The line is a fit of the data according to [53]*

.

The angular cross sections for Calcium are seen in the fig 5.30. The influence of both Fermi smearing and FSI are shown. Missing mass cut and kinetic energy selection of the η are also tested and the effect on the cross section is seen in the right part of the fig 5.30.
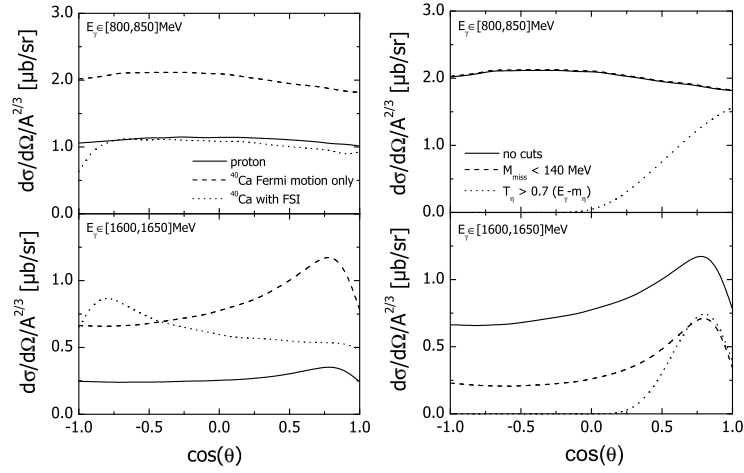
Figure 5.30: *Angular cross sections for the Calcium target for two incident photon beam energy ranges. Left plot: Fermi smearing and FSI are tested. Right plot: Influence of missing mass cut and kinetic energy condition*

.

5.3.7 Spatial distribution and average probed density

An interesting aspect is to study the spatial distribution of η's produced in the nucleus which can escape from the nucleus and then be detected. A common geometrical shape to represent a nucleus is a sphere. In that situation, the density at a point of the nucleus is a function of the distance between this point and the center of the sphere, as suggested for example by the Wood Saxon distribution. Therefore spatial distribution and density can be connected. In the fig 5.31 the ratio of the average probed density to the normal nuclear density ρ_0 is shown for two incident photon beam ranges and different conditions on the event selection.

The influence of both the missing mass cut and the selection on the η kinetic energy is shown.
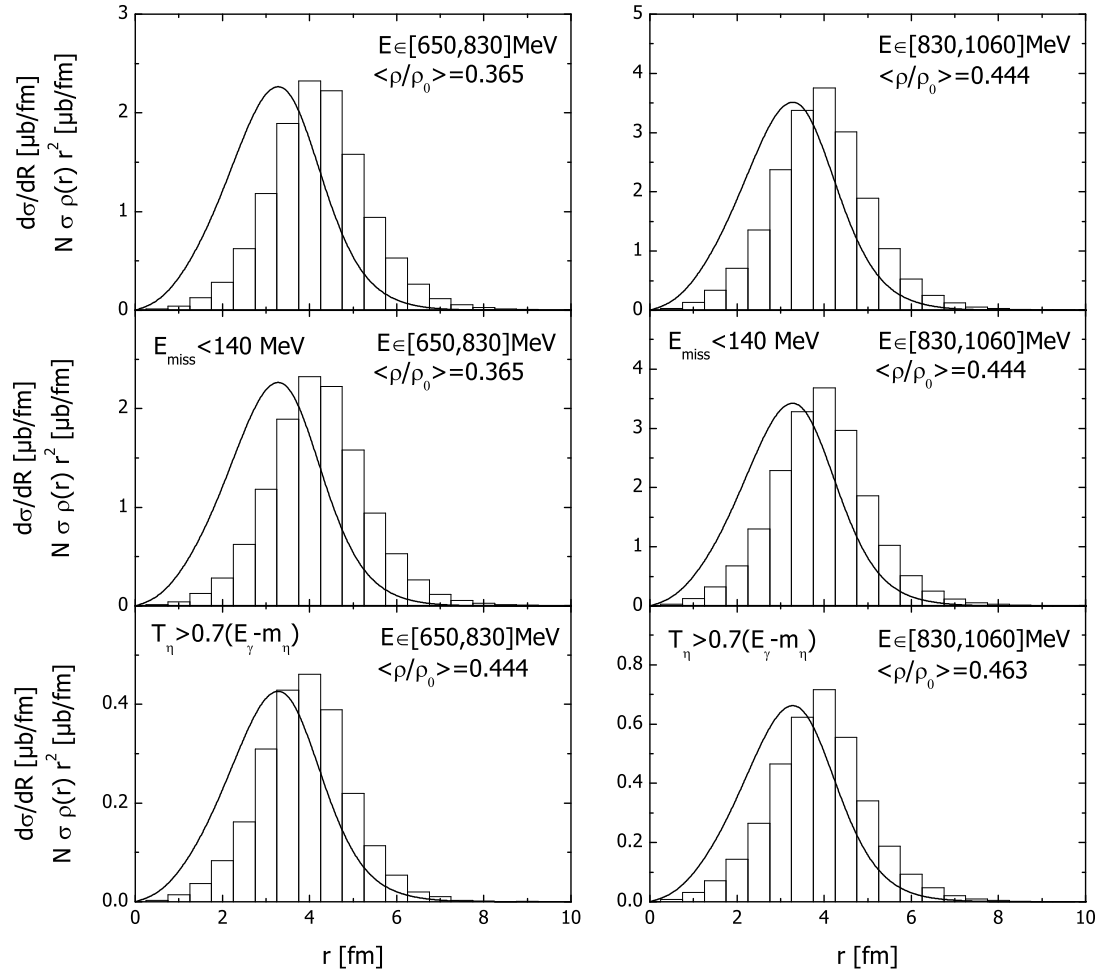
Figure 5.31: *Distribution of the creation point of the η meson in the Lead target. The plot on the left shows the probed density for incident photon beam energies between 650 and 830 MeV. The plots on right show the same features for the range (830, 1060 MeV)*

For the low energy range, between 650 and 830 MeV, the selection of the highest η kinetic energies shifts upwards the average density where the η can be created and detected in a proportion of almost 25 %. The lineshape of the $S_{11}(1535)$ resonance is almost covered with photon energies between 650 and 1060 MeV. Since the η production at threshold is completely dominated by the $S_{11}(1535)$, the spatial distribution of the detected η's is directly connected to the creation point of the resonance for the low energy range. For the higher energy range some background can contribute and may bias the determination of the average density where the $S_{11}(1535)$ is produced.

Since the cut on the kinetic energy removes most of background, the average probed density found by the simulation is more sensitive to the properties of the $S_{11}(1535)$ in a sense that a larger fraction of η event comes from the decay of the $S_{11}(1535)$ when one compares with the full data.

According to the preliminary results of the BUU simulation, the selection on the kinetic energy of the η turns out to be quite efficient to probe at a relatively higher density the resonance in comparison to the average density seen by the full data sample. It is therefore possible to argue that the comparison of the Niobium data to the simulation using this selective cut on the energy is a sensitive tool to detect any possible in-medium modification of the resonance.

Chapter 6

Conclusion and outlook

The in-medium properties of resonances from the second region have been investigated via meson photo-production. During an experiment with real photons, the full nuclei is illuminated with the same probability such that nuclear reactions may occur at the normal density ρ_0 where already significant effects on the in-medium hadron properties are expected.

The total and differential η cross sections have been measured for four different nuclei, Carbon, Calcium, Niobium, and Lead in order to analyse possible in-medium modifications of the $S_{11}(1535)$ resonance. The cross sections scale like $A^{2/3}$ at the reaction threshold of the η meson which indicate a strong absorption effect of the η in the nuclear medium in this energy range. Furthermore, the differences observed at high photon energies may be explained by a relatively higher number of low energetic η's created during secondary reactions. Some conditions have been applied to the selection of the η kinetic energy to extract the lineshape of the $S_{11}(1535)$ resonance free of background coming from primary $\eta\pi$ or secondary η's due to rescattering processes. Final state interactions between the η meson and the nuclear medium have been studied in term of η mean free path considering events with the highest available kinetic energy. With this condition most of the background to the single η production is removed. Thus, an estimate of the absorption cross section has been made in the framework of the Glauber theory and a more or less constant value around 30 mb for the $(\eta - nucleon)$ absorption cross section has been found throughout the entire kinetic energy range. This feature indicates strong final state interactions of the η meson with the nuclear medium at any η energy. Finally no strong modifications of the $S_{11}(1535)$ resonance properties have been found.

The total $\pi^0\pi^0$ cross section has been measured off calcium to measure possible in-medium modifications of the $D_{13}(1520)$ resonance. In comparison with the $S_{11}(1535)$ a strong modification of the resonance lineshape is predicted due to its large coupling to the $N\rho$ channel. Data on deuterium show already a large modification as compared with the data off the proton which may be explained by a different cross section off the neutron. The Analysis of deuterium is still under way. The excitation function for $2\pi^0$ production off Calcium nuclei is much different then the proton data. It is

almost constant throughout the second and third resonance region and the pronounced valley between the two resonances bumps for the proton is absent. This outcome of the data might be in agreement with the in-medium modification of the $D_{13}(1520)$ spectral function.

Furthermore, this result might help to understand the photoabsortion picture observed by [16],([17]), and ([18]).

Further experiments are planed both in Bonn and in Mainz with a better statistic to understand the properties of the second resonance region.

6.1 Tables

6.1.1 Total η cross section

Carbon

E_γ(MeV)	σ (μb)	E_γ(MeV)	σ (μb)
2208.72607	5.29658 ± 0.45974	1487.46094	5.86666 ± 0.20973
2192.45605	5.06969 ± 0.48438	1447.26001	6.29315 ± 0.21326
2176.43896	6.10744 ± 0.49644	1404.85706	6.34420 ± 0.20583
2160.53198	5.31614 ± 0.44649	1360.03198	6.64460 ± 0.19953
2144.60303	5.47401 ± 0.44387	1312.53601	6.85230 ± 0.23588
2128.54810	5.70856 ± 0.43750	1262.09009	6.84740 ± 0.20551
2112.26782	5.55233 ± 0.41332	1208.40295	7.44524 ± 0.17718
2095.68018	5.49329 ± 0.38908	1151.14099	7.84955 ± 0.17086
2078.71289	6.10161 ± 0.41265	1089.95190	8.70082 ± 0.15568
2061.30493	6.09329 ± 0.40551	1024.44751	8.54783 ± 0.14104
2043.40503	5.85400 ± 0.38563	954.21179	10.02770 ± 0.14577
2024.96509	6.19230 ± 0.38483	928.63263	11.01070 ± 0.27942
2005.95215	5.26192 ± 0.36987	906.01935	10.55150 ± 0.26750
1986.32788	6.06194 ± 0.48199	882.91235	11.36510 ± 0.27448
1966.06287	6.27821 ± 0.37354	859.29865	11.86600 ± 0.26869
1945.13599	5.41680 ± 0.31513	835.16400	10.98010 ± 0.25759
1923.51404	5.84674 ± 0.32753	810.49463	10.60130 ± 0.24505
1901.17896	6.31865 ± 0.35546	785.27704	9.26734 ± 0.22340
1878.09705	6.00307 ± 0.34597	759.49567	8.85004 ± 0.21349
1854.24194	6.35925 ± 0.34035	733.13696	6.64759 ± 0.17968
1829.58008	6.33967 ± 0.31162	706.18506	3.91217 ± 0.13342
1804.06995	6.08757 ± 0.30623	678.62469	3.80775 ± 0.13725
1777.66797	6.14343 ± 0.30900	650.44037	2.21943 ± 0.10295
1750.32202	6.38214 ± 0.28868	621.61597	1.52987 ± 0.08259
1721.96704	6.35113 ± 0.27378	592.13531	0.94573 ± 0.06498
1692.53088	6.84281 ± 0.27532	561.98199	0.60734 ± 0.05376
1661.92810	6.57279 ± 0.25877	531.13867	0.92195 ± 0.05810
1630.06091	6.89171 ± 0.25810	499.58798	0.56097 ± 0.04364
1596.81702	6.42233 ± 0.24359	467.31265	0.87714 ± 0.05203
1562.06812	6.63103 ± 0.24946	434.29501	0.82267 ± 0.04781
1525.67297	6.98402 ± 0.25726	400.51636	0.61334 ± 0.03994

Calcium

E_γ(MeV)	σ (μb)	E_γ(MeV)	σ (μb)
2208.72607	6.85793 ± 0.65344	1596.81702	8.71103 ± 0.30296
2192.45605	6.95830 ± 0.68755	1562.06812	9.45713 ± 0.31407
2176.43896	7.80458 ± 0.69421	1525.67297	9.35213 ± 0.30226
2160.53198	7.82164 ± 0.66746	1487.46094	8.04307 ± 0.24795
2144.60303	7.06926 ± 0.59113	1447.26001	9.01814 ± 0.26204
2128.54810	7.76504 ± 0.62694	1404.85706	8.77640 ± 0.24909
2112.26782	7.98036 ± 0.60374	1360.03198	9.04263 ± 0.23699
2095.68018	8.01750 ± 0.56542	1312.53601	8.95515 ± 0.26202
2078.71289	7.56512 ± 0.55513	1262.09009	8.72504 ± 0.23026
2061.30493	8.18374 ± 0.56498	1208.40295	8.45561 ± 0.19470
2043.40503	8.46815 ± 0.55408	1151.14099	9.19155 ± 0.18880
2024.96509	8.13377 ± 0.52542	1136.35193	9.37254 ± 0.25481
2005.95215	8.50861 ± 0.54947	1105.77002	9.16411 ± 0.24005
1986.32788	8.98266 ± 0.64431	1074.13403	9.34824 ± 0.22952
1966.06287	8.63768 ± 0.50531	1041.39404	10.20660 ± 0.22962
1945.13599	8.35032 ± 0.45515	1007.50098	10.79750 ± 0.22090
1923.51404	7.80273 ± 0.41697	972.39600	12.13100 ± 0.23001
1901.17896	8.24169 ± 0.46520	936.02765	11.88670 ± 0.22789
1878.09705	8.21620 ± 0.46046	898.33563	13.04320 ± 0.23329
1854.24194	8.87931 ± 0.45389	859.26007	12.88170 ± 0.22198
1829.58008	9.04114 ± 0.42080	818.73779	11.43590 ± 0.20612
1804.06995	9.02191 ± 0.41893	776.70447	9.41064 ± 0.17996
1777.66797	9.24717 ± 0.42052	733.09302	5.56901 ± 0.13453
1750.32202	8.85123 ± 0.37729	687.83417	2.91855 ± 0.09658
1721.96704	8.44198 ± 0.34231	640.85626	1.16811 ± 0.06049
1692.53088	9.18944 ± 0.35032	592.08557	0.62521 ± 0.04267
1661.92810	9.48705 ± 0.33977	541.44562	0.31084 ± 0.02584
1630.06091	8.97932 ± 0.31830	488.85678	0.46765 ± 0.03310

Niobium

E_γ(MeV)	σ (μb)	E_γ(MeV)	σ (μb)
2200.59106	9.76691 ± 0.57001 9	1028.01001	12.64390 ± 0.41112 9
2168.48511	10.42020 ± 0.56380 9	1007.53339	13.47450 ± 0.43235 9
2136.57568	10.21210 ± 0.52794 9	986.61896	13.60020 ± 0.41967 9
2103.97388	10.38100 ± 0.48696 9	965.25934	13.34000 ± 0.41981 9
2070.00928	11.21750 ± 0.48891 9	943.44037	13.83690 ± 0.42887 9
2034.18494	10.27240 ± 0.44404 9	921.14868	14.67060 ± 0.44701 9
1996.14001	10.97240 ± 0.51321 9	898.37262	14.03810 ± 0.40687 9
1955.59937	10.40830 ± 0.40255 9	875.09796	13.98620 ± 0.41323 9
1908.30005	10.81920 ± 0.40288 9	851.31232	14.49510 ± 0.40430 9
1861.38208	10.74860 ± 0.39178 9	827.00098	12.25830 ± 0.37646 9
1811.70532	10.91300 ± 0.36404 9	802.15039	11.12880 ± 0.34653 9
1758.50488	10.79780 ± 0.33770 9	776.74664	10.51950 ± 0.33036 9
1701.33813	10.82530 ± 0.30893 9	750.77435	8.71601 ± 0.29467 9
1639.59253	10.91970 ± 0.28916 9	724.21967	6.35542 ± 0.24426 9
1572.45886	11.19860 ± 0.28588 9	697.06665	3.90468 ± 0.18650 9
1498.88403	10.25500 ± 0.26105 9	669.29999	2.66168 ± 0.16268 9
1479.58704	9.70470 ± 0.33634 9	640.90399	2.43991 ± 0.15303 9
1438.96216	11.29290 ± 0.35616 9	611.86304	0.73629 ± 0.07172 9
1392.48901	10.66960 ± 0.33761 9	582.15967	0.44693 ± 0.06300 9
1341.36792	10.38810 ± 0.34440 9	551.77832	0.44607 ± 0.06270 9
1292.72803	10.67690 ± 0.35674 9	520.70135	0.90754 ± 0.07925 9
1241.02197	11.26040 ± 0.32123 9	488.91098	0.69053 ± 0.06477 9
1185.94690	11.22440 ± 0.28798 9	456.39035	0.37493 ± 0.04703 9
1127.15698	11.65730 ± 0.25490 9	423.12070	1.09791 ± 0.07567 9
1064.29102	12.84340 ± 0.24647 9	389.08469	0.66653 ± 0.05953 9
1048.06335	12.91530 ± 0.44735 9	151.35634	0.59141 ± 0.04385 9

Lead

E_γ(MeV)	σ (μb)	E_γ(MeV)	σ (μb)
2200.59106	11.16530 ± 1.04616 9	989.32971	14.12870 ± 0.25245 9
2168.48511	10.42940 ± 0.96447 9	972.42969	14.28590 ± 0.63817 9
2136.57593	12.64050 ± 1.00166 9	950.76501	15.07640 ± 0.66261 9
2103.97412	11.29900 ± 0.85689 9	928.63263	14.72920 ± 0.65540 9
2070.00903	12.50860 ± 0.87309 9	906.01929	15.05680 ± 0.65510 9
2034.18506	12.01750 ± 0.80628 9	882.91241	9.60795 ± 0.47337 9
1996.14001	12.65250 ± 0.89542 9	859.29858	14.77290 ± 0.61233 9
1955.59900	12.48560 ± 0.73016 9	835.16400	13.91280 ± 0.59074 9
1912.34595	12.31940 ± 0.68603 9	810.49463	12.49960 ± 0.54531 9
1866.17004	12.63170 ± 0.70052 9	785.27698	11.84780 ± 0.51661 9
1816.82495	12.87930 ± 0.63618 9	759.49573	10.10480 ± 0.46664 9
1763.99500	12.28380 ± 0.59430 9	733.13702	7.01752 ± 0.37718 9
1707.24902	12.36570 ± 0.52738 9	706.18512	5.04422 ± 0.30694 9
1645.99500	12.75580 ± 0.50379 9	678.62469	3.32545 ± 0.25481 9
1579.44299	13.08510 ± 0.48655 9	650.44043	2.93004 ± 0.23318 9
1506.56702	12.23730 ± 0.42881 9	621.61603	2.24162 ± 0.19773 9
1426.05896	13.00700 ± 0.40838 9	592.13531	1.88275 ± 0.17890 9
1336.28406	13.18350 ± 0.40406 9	561.98199	2.35056 ± 0.19915 9
1235.24597	13.11650 ± 0.34931 9	531.13867	1.82035 ± 0.15762 9
1120.54700	13.71040 ± 0.29157 9	499.58801	1.92967 ± 0.15673 9
1074.16296	14.64340 ± 0.71964 9	467.31271	0.93036 ± 0.10208 9
1054.65698	14.21870 ± 0.69566 9	434.29501	2.23551 ± 0.15016 9
1034.73999	13.45190 ± 0.65373 9	400.51639	2.05700 ± 0.13850 9

Acknowledgements

Curriculum Vitae

General informations:

Name: Thierry Mertens
Date of birth: september 20, 1977
Place of birth: Nice(France)
Nationality: French
Adress: 26, rue du Ventron 68100 Mulhouse (France)

Education:

2001-2006 PhD"Photo-Excitation of Nucleon Resonances from complex nuclei "
University of Basel (Switzerland) with Pr. Dr. B. Krusche

2000-2001 DEA (Diplome d'Etude Approfondie) "physique subatomique"
University of Nantes (France)

1999-2000 Maitrise "physique fondamentale"
University of Nice (France)

1998-1999 Licence "physique fondamentale"
University of Nice (France)

1995-1997 Deug "sciences de la matiere"
University of Nice (France)

1995 Baccalaureat Serie S
Lycee Guillaume Apolinaire, Nice(France)

Scientific experience:

2001+ Assistant for Anfängerprakticum
Assistant for Nuclear physic exercices
Participation to several experiments
ELSA, (Bonn, Germany)
MAMY, (Mainz, Germany)
Jlab, (Newport News, Virginia, USA)

Bibliography

[1] http://nobelprize.org/physics/laureates/2004

[2] PDG - Particle Data Group: Particle booklet. American institut of physics, (July 2004)

[3] V. Koch Introduction to chiral symmetry LBNL-Report 38000 (1995)

[4] M. Gell-Mann, R.J. Oakes, B.Renner, Phys Rev 175(1968) 2195

[5] M. Lutz, S. Klimt, W.Weise, NPA 542(1992) 521

[6] G.E Brown, M.Rho, PRL 66 (1991) 2720

[7] QCD sum rules, C.M Ko; linear sygma model, Hatsuda et al.

[8] N. Isgur and G. Karl, Phys. Lett 72B (1977) 109.

[9] S. Godfrey and N. Isgur, Phys Rev. D32(1985) 189.

[10] S. Capstick and N. Isgur, Phys. Rev D34, (1986) 2809.

[11] S. Captcisk and W. Roberts, Phys. Rev D47, (1993) 1994.

[12] S.Capstick, W. Roberts, Quark model of baryon masses and decay, nucl-th 0008028 (2000)

[13] Mathias Roebig Landau, Phys.Lett.B373:45-50, 1996

[14] S. Damjanovic et al. arXiv:nucl-ex/0510044 v1, 2005

[15] David Trnka et al., Phys.Rev.Lett.94:192303,2005

[16] N.Bianchi et al. Phys. Lett B 325

[17] T. Frommhold et al., Phys. Lett B295(1992) 28-31

[18] T. Frommhold et al., Z. Phys A350(1994) 249-261

[19] B. Krusche et al., Eur. Phys. J. A 22, 277-291 (2004)

[20] F.E Close An introduction to Quarks and partons, Academic Press, London (1979)

[21] L. Montanet et al. , Phys Rev D50(1994) Review of particle properties

[22] T.Yorita et al., Phys. Lett B476 (2000) 226

[23] H.Yamasaki et al., Nucl. phys A 670(2000) 202c

[24] T. Kinoshita et al., nucl-ex/0509022 (2005)

[25] B.Krusche et al. Phys. Lett B 74 (1995) 3736

[26] V. Crede et al. Phys.Rev.Lett.94:012004,2005

[27] F. Renard et al, Phys. Lett B 528(2002) 215

[28] F.Bloch et al, PhD Thesis (Basel 2005)

[29] M.Fuchs et al., PhD Thesis (Bonn 2004)

[30] M.Nacher et al., Nucl. Phys A695(2001) 295-327

[31] Braghieri et al., Phys. Lett B363 (1995) 46

[32] Y. Assafiri et al., Phys., Rev., Lett.90:222001, (2003)

[33] Alexander Fix, Uni-Mainz, Private Communication

[34] Igor Horn, Uni-Bonn, PhD Thesis

[35] R. Burgwinkel, Aufbau und Test und Eichung des hochaufloesenden Tagging-Systems TOPAS-II and Bonner SAPHIR-Detecktor, PhD thesis, Physikalisches Institut, University of Bonn, (1996).

[36] E. Aker et al. The Crystal Barrel spectrometer at LEAR, NIM A321,69 (1992)

[37] R. Novotny et al. The BaF$_2$ photon spectrometer TAPS, IEEE transactions on nuclear science 38, 378,(1991)

[38] C. Schmidt, Entwicklung, Aufbau un test eines neuen Auslesesytems fuer den Crystal-Barrel-Detector zur Messung photoinduzierter Reaktionen an ELSA, PhD thesis, Instituet fur Strahlen- und Kernphysik, university of Bonn, (2000).

[39] A.Hombach, A.Angel, S.Teis and U.Mosel, Z.Phys A352(1995) 223

[40] Martin J. Kotulla: Double Pi0 photoproduction off the proton at threshold, Phys. Lett B 57:63-68 (2003)

[41] Martin J.Kotulla: Experiment zur bestimmung des magnetischen Moments der Δ^+(1232) Resonanz, 2001. PhD Thesis Giessen.

[42] Hadronic Spectral Functions of Nuclear matter M. Post, S. Leupold, U. Mosel

[43] G. Agakichiev et al. e^+e^- pair production in Pb-Au collision at 158 GeV per nucleon nucl-ex/0506002

[44] L. Alvarez-Ruso et al. nucl-th/0412084, 2005.

[45] M.Pfeiffer PhD thesis, Giessen University. (2002)

[46] K.S Koelbig and B. Margolis, Nucl. Phys B6 (1968) 85

[47] E. Vercellin et al. Nuovo Cimento A106(1993) 605

[48] E. Lohrmann, Hochenergyphysik, Teubner Studienbucher, (1981).

[49] J.M. Jauch and F. Rohrlich, The Theory of photons and electrons, Springer Verlag, (1980)

[50] B. Rossi, High energy particles, Prentice Hall series, (1965).

[51] Bestimmung des Photonenflusses. Daniel Elsner, Andre Suele, Kathrin Fornet-Ponse, Bonn (2005)

[52] Geant Detector Description and simulation Tool, CERN Geneva, Switzerland.

[53] http://www.kph.uni-mainz.de/MAID/eta/

[54] Gnoechlein et al. Z. Phys. A 352 (1995) 327-343

[55] Chiang et al. Nucl. Phys. A 700 (2002) 429-453

[56] Pascal Muehlich, Giessen university, (Private Communication)